Clemson University
TigerPrints

8-2015

Manipulation of the Electrical Double Layer for Control and Sensing in a Solid State Nanopore

Samuel L. Bearden
Clemson University

Follow this and additional works at: https://tigerprints.clemson.edu/all_dissertations

Part of the Biomedical Engineering and Bioengineering Commons

Recommended Citation

MANIPULATION OF THE ELECTRICAL DOUBLE LAYER FOR CONTROL AND
SENSING IN A SOLID STATE NANOPORE

_____

A Dissertation
Presented to
the Graduate School of
Clemson University

_____

In Partial Fulfillment
of the Requirements for the Degree
Doctor of Philosophy
Bioengineering

_____

by
Samuel L Bearden
August 2015

_____

Accepted by:
Guigen Zhang, Committee Chair
Stephen Foulger
Christopher Saski
Bruce Gao
Alexey Vertegel

ABSTRACT

Nanopores have been explored with the goal of achieving non-functionalized, sub-molecular sensors, primarily with the purpose of producing fast, low-cost DNA sequencers. Because of the nanoscale volume within the nanopore structure, it is possible to isolate individual molecular and sub-molecular analytes. Nanopore DNA sequencing has remained elusive due to high noise levels and the challenge of obtaining single-nucleotide resolution. However, the complete electrical double layer within the nanopore is a key feature of fluid-nanopore interaction and has been neglected in previous studies. By exploring interactions with the electrical double layer in various nanopore systems, we characterize the material, electrical, and solution dependent properties of this structure and develop a new sensing technique.

The overall goals of this project are development of a theoretically complete and useful model of the electrical double layer in a nanopore, development of a nanopore device capable of detecting and manipulating the electrical double layer, characterization of active nanofluidic control, and detection of molecular and double layer properties. By considering extensive numerical models along with experimental evaluation of the nanopore devices, we characterize the fluidic and sensor properties of the electrical double layer in a nanopore. The ability to interact with the electrochemical and structural properties of the fluid within a nanopore offers new avenues for molecular detection and manipulation.

We find that the energetic balance between the nanopore surface potential and the distribution of charged species within the electrical double layer is the key relationship governing the operation of this type of device. A method of active control of the ionic conductance through the nanopore was developed, with complete gating and on-state modulation. A molecular sensing technique was developed by correlating changes to the electrochemical potential of the solution to the physical properties of molecular analytes. The theoretical and practical limits of the nanopore sensor were tested by implementing a new type of nanopore DNA sequencer. High accuracy DNA sequences were produced by combining the double layer potential and ionic current channels in parallel, along with extensive application of signal theory, digital signal processing, and machine learning techniques.

Finally I would like to thank my family for their support and encouragement as I pursued this project.

TABLE OF CONTENTS

Table of Contents (Continued)

Table of Contents (Continued)

Table of Contents (Continued)

Table of Contents (Continued)

LIST OF TABLES

LIST OF FIGURES

List of Figures (Continued)

List of Figures (Continued)

Figure   Page

List of Figures (Continued)

Figure   Page

List of Figures (Continued)

List of Figures (Continued)

CHAPTER 1 : INTRODUCTION

1.1 <u>Background</u>

Nanopores as fluidic devices and sensors have been investigated with many different materials and conformations. Truly the amount of variation in designs is incredible, given that the basic structure is essentially a tiny hole. Solid-state nanopores are important devices in future biosensing. They can be fabricated by using several different methods, such as selective etching, e-beam sculpting, and focused ion beam sculpting with a variety of materials. While the electrical and surface properties of the selected materials may affect the characteristics of nanopore behavior, different fabrication methods will also affect the shape of nanopores and sometimes even alter the electrical characteristics of the materials that make the nanopores. Because of such inherent complexity, analysis of the electrical and fluidic properties of a nanopore device requires the consideration of all relevant physics associated with the device. Of particular importance to the modeling of the fluidics through a nanopore is the consideration of the electrical double layer.

1.1.1 <u>Electrical Double Layer</u>

The electrical double layer (EDL) consists of the accumulation of species at the interface of a material with a liquid solution. Over the years, different models of the EDL have been considered and the layers referred to in the double layer have varied. Some conceptions of the EDL consider a layer of charge on the material surface and the accumulation of species in the solution as the double layer. Others models have

considered multiple layers of charge rather than two. In this work, we base our understanding of the EDL on the Gouy-Chapman-Stern (GCS) model of the electrical double layer. The GCS-EDL is primarily concerned with two layers in the liquid solution, the compact layer and the diffuse layer. The compact layer is made up of solvent molecules and ions that are immobile and adsorbed to the material/solution interface while the diffuse layer consists of mobile solution which carries a net charge within the solution. The distribution of charges in the diffuse layer is governed by the Debye length and serves to screen the surface potential or charge of the material. Within a nanopore, the diffuse layer will not decay to electroneutrality as it would in an unconstrained volume. Throughout this project, the effects of this overlapping diffuse layer are explored in several different solid state nanopores.

1.1.2 *Basis for this project and highlights of the advances made*

The project discussed in this dissertation is in part inspired by a patent applied for by Dr. Guigen Zhang in 2010 (which was granted in 2014).[1] The patent highlights his new discovery that the capacitance of the EDL is extremely sensitive to molecular interrogation and when coupled with a nanopore, it will provide a unique nanopore sensor sensitive to changes in the EDL structures caused by molecular and ionic species that translocate through the EDL. Essentially, this EDL based nanopore technology differs from the majority of nanopore devices, which typically rely on measurement of the ionic current through the nanopore. In implementing this patented technology for controlling and detecting changes to the electrical double layer in a nanopore, we further advanced

the EDL based nanopore technology in several areas, notably the nanopore dimensions, substrate design, and variables of interest. This dissertation will discuss the development of a practical EDL nanopore device and all these aspects in detail in subsequent chapters.

Aside from the advances on the experimental fronts, this dissertation also highlights the numerical model (based on the GCS-EDL model) developed for the first time in a nanopore to account for the physical and electrical behavior of nanopores in a way that is more complete and consistent than has been seen in previous studies. With this complete model, we are able to characterize the interaction between the electrical double layer and the nanopore surface potential for the control of the nanopore as a nanofluidic device. Moreover, another important improvement this dissertation will present is that with a complete model along with full experimental characterization, changes to the EDL due to molecular analytes (including DNA) are demonstrated through measurements of the charging potential of the EDL capacitance, rather than the direct measurements of capacitance.

1.2 <u>Structure of This Dissertation</u>

The structure of this dissertation roughly follows the development of the project from initial modelling, to development of double layer manipulation, to implementation of a robust sensor design. Chapter 2 presents an overview of the techniques that may be used to model nanopore fluidics and sensing, and this chapter has been published as a book chapter in the Spring of 2015.[2] In this chapter, methods such as molecular dynamics,

Monte Carlo, and numerical continuum modelling are examined with consideration of the strengths, weaknesses, and requirements of each.

In chapter 3, a numerical model of the electrical double layer in a single-walled carbon nanotube is developed and used to evaluate the surprisingly-high electrical conductance through a carbon nanotube. The implementation of the compact layer of the electrical layer was constrained by matching the model conductance to corresponding experimental measurements derived from literature. Our numerical model of the electrical double layer in a nanopore was developed in a continuum modeling software package (COMSOL 4.2a). The primary considerations that differentiated this model from previous studies are the consideration of the work function potentials of the solution and materials, and the consideration of the compact layer. These two considerations served to bring our understanding of the behavior of electrolyte solution within the nanopore into alignment with standard electrochemical theory. Key findings of this study were characterization of the contribution of the complete electrical double layer to the relationships observed in the nanopore conductivity and the consideration of the work function potential of the nanopore materials as an important contributor to the double layer behavior. The contents of chapter 3 were published in 2013.[3]

The fourth chapter details an investigation into experimentally controlling the nanopore ionic conductance by modulating the surface potential. We manipulated the electrical double layer in a metallic nanopore by applying an electrical potential to the surface of the nanopore. Experimentally, we observed gating and linear amplification of the ionic conductance through the nanopore depending on the polarity and magnitude of the

applied bias. By adapting our numerical model of the electrical double layer to the geometry, materials, and electrical conditions of our experiment, we were able to describe the changes to the double layer that were responsible for the observed conductance effects. The numerical model from chapter 3 was expanded and adapted to the experimental system in order to provide a theoretical basis explaining the observed behavior. This chapter was published in the spring of 2015. [4]

Molecular detection via the electrical double layer in a nanopore is explored in chapter 5. The metallic layer of the nanopore was brought to equilibrium with the electrochemical potential of the electrical double layer. Small molecules with well-defined physical and electrical properties were driven through the nanopore and the measured change in solution potential was recorded. Based on our observation of the balance between the charge in the electrical double layer and the applied surface potential in Chapter 4, it seemed likely that the process could be inverted. In order to allow the double layer to control the surface potential, it was necessary to allow the surface potential to stay in equilibrium with the energetic potential of the electrical double layer. The equilibrium potential nanopore electrode was produced by supplying a small electrical current to the metallic layer of the nanopore. Initial confirmation that the electrode was in equilibrium with the solution was obtained by observing that the steady-state potential measured at the electrode was logarithmically related to the concentration of the supporting electrolyte. A logarithmic relationship with concentration is typical for the activity and electrochemical potential of a solution. In seeking to describe the solution/electrode balance, it was helpful to return to the original work on the electrochemical potential of

aqueous electrolyte solution by Huckel and Debye. [5] Their analytical description of the relationship between the charge, size, and permittivity of constituent ions with the electrochemical potential of solutions was similar to our experimental observations, particularly the logarithmic relationship between concentration and potential. The numerical model was adapted to the electrical equilibrium sensing modality and provided insight into the underlying mechanics of the sensor.

Chapter 6 covers an implementation of the nanopore double layer sensor as a DNA sequencer. DNA is an interesting analyte and prime target for nanopore sequencing. We take advantage of the limited input space afforded by the known nucleotide bases to simplify the sensor operation while accounting for the multi-nucleotide resolution of the sensor. By using a hidden Markov model, the nucleotide input was mapped to the high-resolution sensor output, creating a system capable of achieving high basecall accuracy.

1.3 <u>Summary</u>

Throughout this project, the EDL has been examined as a medium for interaction with the contents of a nanopore. By applying a potential to the surface of the nanopore, we were able to manipulate the EDL structure and obtained very good control over the ionic conductance through the nanopore. When measuring the charging potential of the EDL capacitance, we were able to detect and identify molecular targets. Using this method, small molecules and DNA were successfully identified and sequenced. Throughout, numerical modeling of the electrical double layer has lent insight into the mechanics underlying the observed phenomena.

CHAPTER 2 : A SOLID-STATE NANOPORE AS BIOSENSOR

2.1 <u>Introduction</u>

Solid-state nanopores are important devices in future biosensing. They can be fabricated by using several different processing methods, such as selective etching, e-beam sculpting, and focused ion beam sculpting with a variety of materials. While the electrical and surface properties of the selected materials may affect the characteristics of nanopore behavior, different fabrication methods will also affect the shape of nanopores and sometimes even alter the electrical characteristics of the materials that make the nanopores. Because of such inherent complexity, analysis of the electrical and fluidic properties of a nanopore device requires the consideration of all relevant physics associated with the device. This may be better accomplished by using either a deterministic or probabilistic modeling techniques. Of particular importance to the modeling of the fluidics through a nanopore is the consideration of the electrical double layer. This chapter discusses the effects of various factors affecting the performance of a nanopore biosensor, and presents a case study in which a nanopore consisting of a single walled carbon nanotube is modelled.

Biosensors are analytical devices that combine a biologically sensitive element with a physical transducer to selectively and quantitatively detect the presence of specific compounds in a given biological environment [6]. Like any conventional sensors, a biosensor is expected to be sensitive, responsive, and reliable over a long period of time. However, since a biosensor is often exposed to an environment containing many

biological species that are similar in structures and binding behavior, it needs to be specific, that is, being responsive only to the specifically targeted analyte species. A biosensor may directly measure a measurand of interest (as in the case of typical electrolytic pH sensors) or make indirect measurements that are related to the measurand of interest (as in the case of enzyme mediated sensors). In any case, the key to designing and calibrating such biosensors is to know the underlying principle that describes how signal transduction occurs and how the output signal is related to the measurand. For example, in the case of the electrolytic pH meter, the input is the concentration of hydrogen ions and the output is an electric potential signal with the operations governed by the Nernst equation. In the case of an enzyme mediated biosensor, the actual target is the enzyme substrate (e.g., glucose), but the measured signal is often an electrical current that occurs during the oxidation of the substrate [7–9].

For most biosensors, various physical and chemical methods are used for converting the biological events into electrical or optical signals, such as the mechanical, optical, electromagnetic, electrical, thermal, magnetic and electrochemical methods, among others. The pH meter and enzymatic mediated biosensor mentioned earlier are of the electrochemical type. The performances of this type of biosensors rely not only on the kinetics of the underlying electrochemical reactions but also on the mass transport behavior near and around the electrodes. Since mass transport is a phenomenon affected by both temporal and spatial restrictions and limitations, predicting the performances of electrochemical-based biosensors has been difficult in certain cases, if not impossible, due to the sophisticated fluidic designs of these biosensors.

Case in point: solid-state nanopores have been widely recognized as a promising sensor design, but their properties are inherently difficult to characterize. For example, in a typical case a nanopore device is placed in a flow cell filled with an electrolytic solution. The device is often biased by an electric field across the pore while the resulting ionic through-pore current is measured (for more detailed discussion on this subject, please refer to the next chapter). Additional electric potentials may be applied near the nanopore surface to create a gating effect. By altering the geometric configurations or the materials comprising the nanopore, one may cause the nanopore to rectify the ionic current, creating a fluidic diode, or to increase the current, creating a fluidic amplifier [10–14]. Rectifying nanopores have been organized into fluidic logic gates, mimicking in a very simplified way the information processing logic found in neurophysiological structures [15]. Recently, there is a great deal of research into using a nanopore system as the basis of very fast and accurate DNA sequencers [16–25]. Next chapter discusses such an application. Several different transduction strategies have been implemented such as using ionic conductance through the nanopore and quantum tunnelling across the two electrodes embedded in a nanopore [19,26–29].

The electro-driven fluidic transport through a nanopore is very complex and has been observed to exhibit unexpected behavior [11,30–32]. Therefore, a practical understanding of the processes governing the operations of a nanopore calls for elucidation of the interplay of electrochemistry, quantum mechanics, materials science, and fluid dynamics, among others. In situations like these, computational modeling provides an effective way for elucidating the mechanics of biosensor performance. In this chapter, we discuss the

various aspects of computational modeling of electrofluidic transport through a nanopore. As a case study, we present in depth the study of electrofluidic flow through a nanopore made of a single walled carbon nanotube.

2.2 The Making of a Solid-State Nanopore

A nanopore is often regarded as a single nanoscale opening through an otherwise impermeable material. Biological nanopores appearing in nature often serve as active or passive transporters through cell membranes. For example, in muscle and nerve tissues, sodium is transported across the cell membrane against an electrochemical gradient due to active transport proteins [33]. Water is passively transported across cell membranes through aquaporins in response to osmotic and hydraulic pressure gradients [34]. Solid-state nanopores, on the other hand, are passive manmade structures. In this chapter we limit our discussion to solid-state nanopores and ignore biological nanopores (discussions on biological nanopores can be found elsewhere [16,20,22]).

A solid-state nanopore can be fabricated using a wide variety of materials and can be shaped in various geometric configurations. For example, nanopores may be in a cylindrical shape when made using carbon nanotubes [10,31,35–37], in a conical shape [38], or in a bow-tie shape [39,40] as illustrated in Figure 2.1. The pore depth (sometimes it is also referred to as the pore channel length) may vary from a few angstroms (when made of graphene) [21,25,41,42] to several microns (when made of carbon nanotubes) [10,35,43] with a pore opening sizing from single to few tens of nanometers [39].

(a)   (b)   (c)
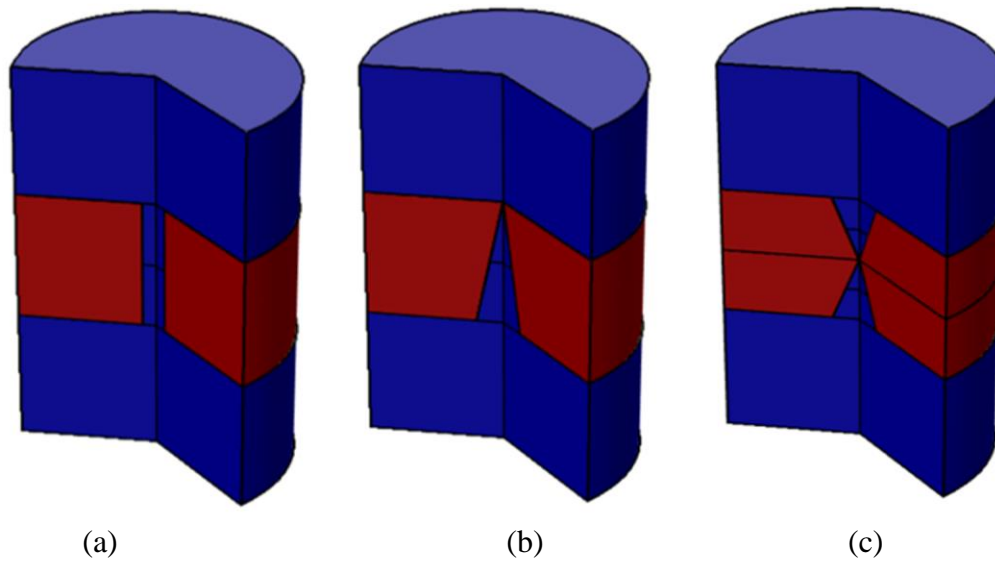
Figure 2.1. Typical solid-state pore geometries. (a): A cylindrical nanopore. Such nanopores may be formed by embedding a nanotube in a supporting material. (b): A conical nanopore. Conical nanopores may be created by depositing the pore material around an electrosharpened tip and then etching the tip. (c): A double conical nanopore. The double conical geometry occurs when a nanopore is formed by sputtering away material, as with a focused ion beam.

2.2.1 *Materials for fabricating solid-state nanopores*

Due to the electrostatic nature of a nanopore and its electronic control in operations, the materials used to fabricate a nanopore will affect its performance. Nanopores are often made using semiconductors and insulating materials such as Si_3N_4, SiO_2/Si, or various polymers.[10,11,32,40] They sometimes are constructed using composite materials in order to elicit specific effects.[44]

The electrical permittivity, work function potential, and other properties of the materials used to make nanopores will dictate their performance. Due to the tiny dimensions of a nanopore, a slight change in the electric work potential and permittivity of its component materials could result in a large change in the electric field within the nanopore lumen, hence the overall sensing performance. For this reason, tuning of nanopore performance may be accomplished through careful selection of the component materials. Component materials are primarily chosen for their electronic and mechanical properties. For a nanopore with a very small pore depth, mechanical stability of the supporting material becomes extremely important [42] for the material must withstand the shearing forces associated with through-pore transport. Failure rates in some nanopore devices are found at 30% due to mechanical failure of the supporting material alone.

Recently, graphene has emerged to become a popular material for nanopore fabrication [21,23,25,27,41,42,44] due to its atomically thin structure allowing the creation of nanopores with extremely tiny pore depth. Graphene consists of a planar, hexagonal honeycomb of carbon atoms that exists in discrete layers. The layers may be mechanically cleaved using a process developed by Novoselov and integrated into free standing membranes [45–48].

2.3 <u>Fabrication processes</u>

The fabrication processes of nanopores depend highly on the desired geometry and chosen materials. While porous membranes can be made relatively easily through anodization or other lithographic techniques, fabrication of a single pore with desirable size and structural as well as electrical properties requires greater controls. Here we list three commonly used methods for nanopore fabrication.

2.3.1 *E-beam/focused ion beam*

Electron beam sculpting is a commonly used top-down approach for silicon based materials and is often used for nanopore drilling. Typically a suspended membrane is prepared using silicon, silicon oxide, silicon nitride, or graphene and loaded into a tunnelling electron microscope. Focusing the e-beam to a diameter of ~1 nm with energy of ~100 keV can drill (or burn) a small hole in the membrane [23,44,49]. E-beam sculpting offers fairly good control in the case of suspended graphene sheets [17,23,24,29,39,41,42,44,49–53]. Nanowires, nanogaps, nanoslits, and nanopores have all been produced in stable configuration using e-beam sculpting of graphene. For graphene, an e-beam may be used to add carbon to the lattice as well as to remove it, useful for shrinking the aperture in the lattice at low energy levels [41]. It has been shown that carbon present in the atmosphere will integrate into the honeycomb lattice graphene in a manner that may be controlled by temperature. This allows precise control over graphene structure and nanopores may be produced with very small diameters by sculpting an initial pore and gradually shrinking with a diffuse beam.

Focused ion beam lithography is a technique that allows sub-micron patterning by controlling the energy level of the incident ions, the type of ions, and the exposure time. The technique consists of generating a stream of ions and focusing the stream at a location on a sample surface. The ions interact with the sample through sputtering, implanting, and heating the substrate [54]. Focused ion beam is a more versatile technique than electron beam sculpting in terms of the types and properties of the ion source. For example, a semiconductor sample may be selectively doped by implanting Boron or

Arsenic, changing the electrical properties or the pore material. Formation of nanopores is possible by sputtering atoms off of the sample surface [55]. Sputtering occurs when ions are given low energy (typically in the 50-1000 eV range) while higher energy ion beams tend to cause implantation. Treating a surface with a focused ion beam will typically alter the crystalline structure of the sample, which will affect the electrical properties and chemical reactivity of the sample at the site of interaction. Nanopores have been fabricated in Al_2O_3, graphene, and Si_3N_4 membranes using FIB [44,56].

2.3.2 *Swift heavy ion tracks in polymer*

Conical nanopores in polymeric materials has been formed by a top down track-etch process [11–14,38,57–60]. This process can create pores with a depth of ~10 μm and with a diameter as small as ~3 nm (up to 1-2 μm). In this process, polymer films of a desired thickness are irradiated by single swift heavy ions. A latent track is left in the polymer in the trail of the swift heavy ion, causing the alteration of the polymer structure along the track from semicrystalline to amorphous. This will help facilitate preferential etching along the latent track during an etching process. By etching the track from one side and monitoring the progress via ionic current, the opening of the pore can be controlled precisely.

2.3.3 *Embedded SWCNTs in insulating material*

Cylindrical nanopores with an extremely long depth can be produced through a bottom up process of growing carbon nanotubes on an insulating substrate and covering the full grown carbon nanotubes with another layer of the insulating material using electron beam

evaporation [10,37,43]. This method has been employed to create highly efficient electrofluidic field effect transistors. Single walled carbon nanotubes (SWCNTs) with desirable dimension have been embedded in an insulating material (such as polymer or oxide materials) to form a sandwich structure, which is then selectively etched to reveal the ends of the nanotubes. The lumens at the two ends are subsequently opened by exposing the ends to oxygen plasma. This method has been used to create nanopores with diameters of 1 to 2 nm and lengths of up to 20 to 30 μm.

2.3.4 *Electrolytic solutions*

Another active component of an electrofluidic nanopore system is the electrolyte fluid. The electrolyte fluid flows though the nanopore, responding dynamically to the electronic structure of the nanopore and the applied electric field. A typical electrolyte fluid is aqueous potassium chloride (KCl) of various concentrations, though other electrolytes (such as NaCl or KF) are also commonly used [14,39,59–61]. In a nanopore with a radius on the order of the Debye length, the relationship between the conductance of the device and the solution concentration is more complex than is typically observed in other systems. The electrical double layer at the pore wall will typically overlap in the diffuse region due to the radial symmetry of the nanopore structure, giving rise to ion selectivity causing the intraluminal fluid to differ drastically from the bulk solution [62–68]. Additionally, the surface properties of the pore wall influenced by the presence of adsorbed charged species or distributed charge will affect the intraluminal fluid transport [14,29,36,68,69].

Electrolyte solutions often consist of various ionic compounds dissolved in water. In the case where the compounds are strong electrolytes, the ionic components of the

compounds (e.g. K^+ and Cl^- from KCl) will dissociate completely and the conductivity of the solution will be a function of the limiting molar conductivities of the individual ionic components. Here the limiting molar conductivity refers to the conductivity of an electrolyte as the solution approaches infinite dilution and is given as λ_0. It can be determined by linear superposition,

$$\lambda_0 = n_1\lambda_1 + n_2\lambda_2 + \cdots$$

Equation 2-1

where λ_1, λ_2, etc., are the limiting molar conductivity for each component, and n_1, n_2, etc., are the number of moles of the corresponding individual electrolytes.

For a strong electrolytic solution, its conductivity (σ) can be estimated as $\sigma = \lambda_0 c$, where c is the concentration of the electrolyte. The conductance of this solution through a narrow channel can be estimated by using the conductance equation:

$$G = \sigma \frac{A}{l}$$

Equation 2-2

where G is conductance and A and l are geometric terms representing the minimum cross-section area and length of the channel. This equation, though often used to provide a baseline reference, is usually a poor predictor for the nanopore's conductance behavior. As examined by Kowalczyk, et al. , this equation predicted conductance well for small, double conical nanopores (<10 nm minimum diameter) but deviated from observed conductance by more than a factor of 2 for larger double conical pores [39]. In double conical nanopores larger than 10 nm, the resistance of the pore becomes comparable to

the resistance of the fluid surrounding the pore (the access resistance), meaning that the access resistance is no longer negligible. A correction factor was proposed which made prediction much more accurate for double conical nanopores with diameters between 10 nm and 100 nm by accounting for access resistance:

$$\left(G = \sigma \left[\frac{4l}{\pi d^2} + \frac{1}{d} \right]^{-1} \right)$$

Equation 2-3

However, for other types of nanopores, this relationship may not apply. For instance, the conductance of a nanopore with a high aspect ratio made of single walled carbon nanotubes (SWCNTs) was found to be 2 to 3 orders of magnitude larger than that predicted by this equation, despite the fact that the nanopore diameter was less than 10 nm [10,31,37].

2.4 Influence of the Electrode-Fluid Interface

In addition to solution conductivity, it is important to consider the interaction between the electrolytic fluid and the nanopore at their interface. Electrical double layer (EDL) is a molecular structure that spontaneously forms at a solid/fluid interface due to the drive of thermodynamic equilibrium. The EDL structure is well studied in the context of electrochemistry, in light of the seminal theoretical and experimental works of Grahame and others in the middle of the 20th century [70,71], which is also discussed in details in the previous chapter. For the sake of the discussion that fellows, we describe it here in brief. EDL consists of a compact layer and a diffuse layer [62,70–72] made of ions and solvent molecules that are accumulated in solution near a solid/liquid interface. Unlike the

compact layer, the ions in the diffuse later are not bound to the surface and may move freely in response to applied forces and potentials. Typically the thickness of the diffuse later is given by the Debye length, where the Debye length is calculated as

$$\lambda_D = \sqrt{\frac{\varepsilon_0 \varepsilon_r RT}{2 F_c^2 c_0}}$$
Equation 2-4

where ε_0 and ε_r are the vacuum and relative permittivity, R is the gas constant, T is temperature, F_c is the Faraday constant, and c_0 is the electrolyte concentration. When the radius of a nanopore is less than or equal to the Debye length, the diffuse layer around the nanopore will overlap, making transport through the nanopore ion selective. In conical nanopore this ion selectivity can lead to current rectification through the creation of depletion regions [12,59].

In both the compact and diffuse layers, the ions and solvent arrange themselves in response to an electrical field generated from the differential potential of the work functions of the nanopore materials and from any charge build-up at the pore wall. The work function of a material is defined as the energy needed to move an electron from the Fermi level to the vacuum energy level. The Fermi level can be thought of as the average energy level of carriers in a material. When a material has a bandgap in its electronic structure due to quantum restrictions, the Fermi level often falls within the bandgap. The Fermi level may be altered by doping the material with hole or electron donors, or by bringing the material in contact with another material possessing a different work function. This is the basis for the design of most diodes, bipolar junction transistors, and field effect transistors. The result is a potential drop at the surface of the nanopore

structure relative to the solution that causes preferential accumulation of ions near the material interface. This accumulation and occlusion are important because the properties of the solution and the volume available for transport within the pore govern the function of the entire device.

2.5 <u>Choosing a Modeling Platform</u>

In modeling nanoscale systems, it is important to select an appropriate modeling platform for the system of interest. In general, there are four main types of mathematical modeling platforms, and they are 1) analytical, 2) numerical continuum, 3) molecular dynamics, and 4) Monte Carlo simulation. Analytical models typically offer the most complete solutions. But since solving an analytical model often requires knowing well-defined physics and boundary conditions, it is sometimes impossible to develop an analytical model or find a solution for it. Numerical continuum models may be used with much relaxed aprior conditions. Numerical methods (finite element modeling as an example) are used to solve weak forms of differential equations over a given domain. This is done by meshing the domain with many small elements over which the approximate solutions to the differential equations are computed. Typically, the size of the elements is gradually decreased, or the number of elements is increased, until the numerical error within the model is decreased to an acceptable level.

In molecular dynamics models, the continuum approach is abandoned in favor of modeling the motion and forces of individual particles. A system is designed as a group of molecules, with each atom and bond defined. The molecules themselves are defined in terms of atomic radius, bond lengths, mass, and charge. The interactions between the

molecules are defined by thermodynamic potential energy fields or by force fields between particles (where the forces are typically due to electrostatics or physical interaction). One may also account for quantum mechanical phenomena in a molecular dynamics simulation. Solutions are often arrived at iteratively. Given an initial starting point for all species in the simulation, the spatially varying interactions between molecules are calculated. The time component of the simulation is then incremented in some small step and the molecules are moved in response to local forces according to Newtonian mechanics. Movement may be estimated by Newtonian mechanics or other more complicated methods. The process is repeated for as long as necessary or achievable.

Monte Carlo simulation is to molecular dynamics what finite element analysis is to analytical solutions. Monte Carlo simulation relies on probabilistic properties of complex systems to generate meaningful outcomes. This type of simulation is useful for systems dominated by Brownian motion or some other randomly varying mechanic. The method was developed at Los Alamos Scientific Laboratory as a way to model neutron scattering in nuclear experiments [73]. There is no standard system that describes Monte Carlo modeling, as methods may vary wildly between physical systems. For example, in optics, a photon may have some finite probability of being absorbed by a surface and some finite probability of being reflected, with a distribution of probabilities as to the direction of reflection. A famous Monte Carlo problem consists of calculating pi (π) by dropping needles on a striped surface (the Buffon's needle problem). Defining a system in terms of these interactions and repeating the experiment many times will produce a result that

models reality. When performed computationally, a source of random numbers with known distribution is used to produce an outcome to each probabilistic event. Practically, the kind of probabilistic information needed to set up a Monte Carlo simulation is very different from the physical information used in other modeling methods. The advantage is that non-deterministic systems may be evaluated with reasonable computational resource. The disadvantage is that Monte Carlo simulations are "black box", and tend not to provide as much mechanistic information as physics driven simulations. In one case, a Monte Carlo simulation was performed to investigate the conformation of DNA in a nanopore [74]. The pore geometry was defined and a model of a DNA chain was created. The DNA chain consisted of 10 base pairs in a freely jointed chain capable of random rotation and stretching. Starting with a random chain orientation, the model DNA was electrostatically driven into the pore. The results provided information about conformation and stretching of DNA in a nanopore (illustrated in Figure 2.2) that would be difficult or impossible to acquire from other simulation methods and provided insight into the meaning of several experimental nanopore current measurements.
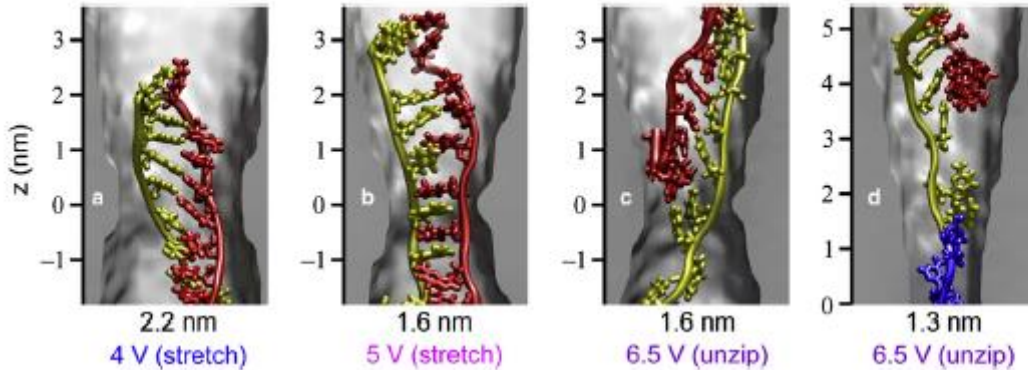
Figure 2.2. A Monte Carlo method was used to determine the conformation of DNA in a

double conical nanopore.[74]

To choose from these different methods of modeling, a decision is necessary in terms

of whether to consider the system as composed of discrete particles (molecular dynamics

or Monte Carlo) or as a structure of the continuum (analytical or finite element). To

decide on this, a key factor to consider is whether the physical dimensions of the system

permit the use of a continuum approach. This typically can be decided by examining the

dimensionless Knudsen number. A Knudsen number less than 1 often justifies the use of

a continuum model while other methods should be used for larger numbers, though to be

convincing, the Knudsen number should be much smaller than 1. The Knudsen number is

originally derived for use in rarefied gases in the upper atmosphere and is defined as the

ratio of the mean free path of particles to some characteristic system length:

$$\left(Kn = \frac{\lambda}{L} \right)$$

Equation 2-5

The use of the Knudsen number in condensed fluid systems is not rigorously supported, yet it is often used as a rule of thumb in nanoscale fluidics [75]. The number is commonly used in studies of micro- and nano-fluidics with good outcomes [10,37,75,76]. The mean free path length in aqueous solutions is often regarded to be the molecular diameter of water (0.3 nm) and the characteristic length will vary depending on the geometry of the system. A Knudsen value in the range from 0.1 down to 0.001 is in a transitional region between probabilistic and continuum approaches that is inherently difficult to model, and both approaches have been used [10,37,75]. A more accurate Knudsen number may be calculated by finding the mean free path of a solvent particle modelled as a sphere (with radius of 0.15 nm, half the molecular diameter of water). The mean free path length is then defined by the formula:

$$\lambda = \frac{MW}{4\pi r^2 N_{avagadro} \rho_v}$$
Equation 2-6

where λ is the mean free path length, MW is the molecular weight of a solvent molecule, r is the molecular radius (0.15 nm in this case), and ρ_v is the mass density of the fluid. The mean free path length for water produced by this method is 0.105 nm which decreases the Knudsen number by about a factor of three. A small, transitional Knudsen number allows for the continuum model to be utilized, but it does not rule out the added value a probabilistic model may provide. However, the computational cost of a probabilistic model of the same scale as the continuum model may tend to be prohibitively high [75].

2.6 Considering the Electrical Double Layer (EDL)

In continuum models, where the finite size of solute and solvent molecules is typically ignored, care must be taken to properly model the EDL. The difficulty in modeling the EDL is the fact that the compact layer forms due to surface adsorption of species with a finite size. The finite size of the adsorbed particles creates a plane of closest approach (the outer Helmholtz plane) which defines the boundary between the compact and diffuse layers. The outer Helmholtz plane will become the practical boundary not only for fluidic flow but also for electron transfer, if any. Continuum modeling of the complete electrical double layer has been extensively studied in the realm of electrochemical nano-electrodes with investigation of various parameters such as electrode size, electrode spacing, compact layer thickness, reaction rate, and presence of supporting electrolyte.

Numerical continuum models of axisymmetric nano-scale electrodes have been produced investigating the effects of the EDL [62,72]. The operating principle of larger scale electrodes is that the current response is limited only by diffusion of the reactant species near the electrodes; however this model breaks down at nano-scale. Attempts to correct this failed to account for the non-electroneutrality that occurs within the diffuse layer of the electrical double layer. A nano-scale model, however, is able to account for most of the phenomena near the electrode that become prominent at nano-scale.

One of these computation models consisted of axisymmetric setting with a spherical electrode having a radius of r_0, and a compact layer thickness of μ (Figure 2.3a). The compact layer was divided into inner and outer Helmholtz planes where the inner plane consists of adsorbed ions or solvent molecules and the outer plane represents the plane of

closest approach for non-adsorbed solution. In electrochemical experiments, the outer Helmholtz plane also serves as the position of electron transfer. The electrical permittivity within the compact layer was defined as smoothly varying between the permittivity of the electrode material and the electrolyte. The smoothly varying permittivity has been defined using segmented cosine and hyperbolic cosine equations or a single sigmoidal equation with good effect. The use of a smoothly varying permittivity within the compact layer produces more accurate models than assuming either a single uniform permittivity or a stepped permittivity where the compact layer is divided into two regions of different permittivity values. Moreover, it allows for the permittivity within the compact layer to be defined for electrodes constructed of any material and for any compact layer thickness.

For a continuum system, the steady-state electrostatic distribution of potential is governed by Poisson equation and the transport and distribution of charged species governed by Nernst-Planck equation. The compact layer is considered to be composed of adsorbed solvent molecules, and therefore containing no net charge. Thus Poisson equation for the compact layer region can be simplified to Laplace equation. The presence of electroactive species undergoing redox reactions at the position of electron transfer may be dealt with by Bulter-Volmer kinetics equations. In the model, Poisson equation is applied over the entire geometry, while Nernst-Planck equation is only considered in the domain of the electrolytic solution, bound by a distant boundary held at constant concentration and the outer Helmholtz plane. At the outer Helmholtz plane, the

concentration of electroactive species is defined by the flux of redox species governed by the Bulter-Volmer equation.

The modeling results were compared against the result of a large scale diffusion limited situation. For a single electrode, the limiting current deviates more as the electrode radius decreases, due to differences in the potential drop across the compact layer which has a size dependent effect. As a result, the diffuse layer is shorter in a relative sense for larger electrodes than for smaller electrodes (100 nm vs 1 nm). The diffuse layer consists of the region outside the compact layer where electroneutrality is not kept due to unequal concentrations of charged species of differing valence. This non-electroneutrality is due to two causes: 1) the depletion of electroactive species at the position of electron transfer due to electrochemical reaction, and 2) the electromigration of charged species in the electric field near the electrode surface. The concentration gradient of any specie is dependent on the concentration of co-solutes due to the screening of electric potential within the solution. The depletion gradient of the reactant species was found to increase in the presence of supporting electrolyte, altering the cyclic voltammetric current response of the electrode.

In the case of interdigitated electrodes, where collector and generator electrodes (Figure 2.3b) are placed in close proximity, the electrochemical properties are influenced by the overlapping of the diffuse layers of the two electrodes. The result is fast redox cycling between the two electrodes. Similar to the case of a single electrode, the influence of the electrical double layer decreases as the size of the electrodes increases. Decreasing the space between the electrodes leads to an increased electrical field between the electrodes,

contributing to enhanced electromigration between the collector and generator. Due to the screening effects of the electrolyte solution, the electrical fields of the two electrodes do not overlap when the gap spacing between them is large (>16 nm), but they strongly overlap when the gap spacing is small (4 nm). It is noted in the case of a single nanoscale electrode that when a supporting electrolyte is not included, the thickness of the diffusion layer will increase. When interdigitated electrodes are considered without a supporting electrolyte, the increased diffusion layer will overlap between the electrodes, creating a peak shaped cyclic voltammogram. Increasing the thickness of the compact layer will lead to a greater potential drop within the compact layer, resulting in a smaller diffusion layer. These models of the electrical double layer discussed here illustrate how a continuum approach can be used in a transitional domain where the benefits of a probabilistic mechanics approach may provide similar validity but with greater complexity.
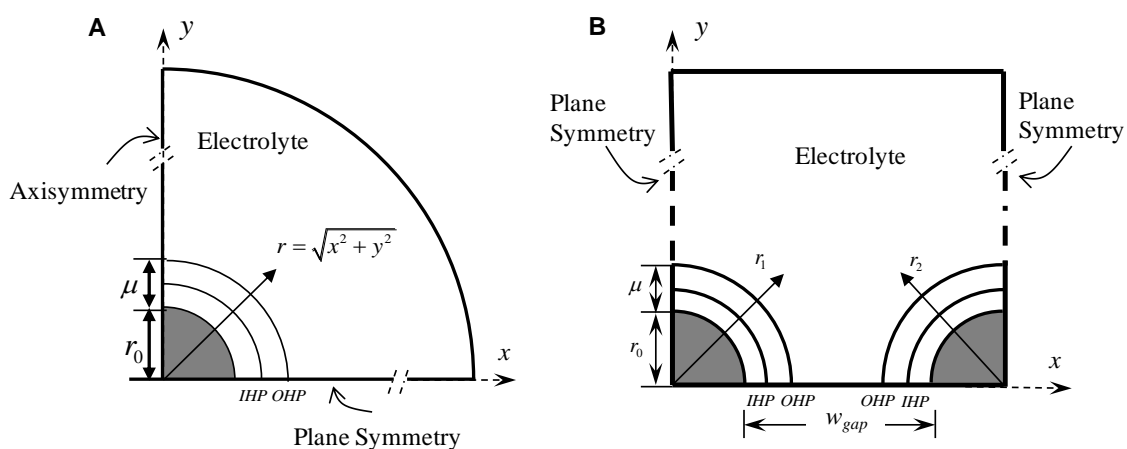
Figure 2.3. The electrical double layer occurs at the interface of an electrode (gray) and solution (white). The compact layer consists of immobilized ions and solvent molecules electrostatically held at the electrode surface. The finite size of these molecules creates a

plane of closest approach to the electrode (the outer Helmholtz layer, OHM) with a

thickness δ. B. When electrodes are placed in close proximity, the electrical double layer

overlaps itself. In a nanopore, EDL overlap is due to the small inner dimensions and is

responsible for some of the unusual properties of nanopores.[62]

2.7 <u>Mass Transport</u>

Mass transport through a nanopore is typically electrokinetically driven. Due to the

small cross sectional area and relative fragility of the supporting membranes comprising

such a device, any significant pressure across the nanopore may lead to structural failure.

Furthermore, due to the extremely small size of the lumen of the nanopore, fluid flow

will likely be laminar and the Reynolds number will be low. Given laminar flow in a low

pressure gradient environment, the fluidic flow will likely be driven predominately by

electrokinetics. The two mechanisms chiefly responsible for mass transport are

electrophoresis and electroosmosis, where electrophoresis is the movement of ions due to

an electric field and electroosmosis is movement of the supporting fluid. Diffusion exist

as a balancing influence that is reactionary to the concentration gradients imposed on the

system by the active mechanisms, but does not significantly contribute to mass flux.

2.7.1 Electrophoresis

Electrophoresis is the transport of charged particles in fluid under an electric field. A

subtlety of this definition is that the fluid may or may not be stationary. A moving fluid

will increase the drag force on ions moving against the flow by increasing the velocity of

the particles relative to the fluid, and vice versa, thus decreasing the drag force on ions

moving with the fluid. Conceptually one can separate the two mechanisms by considering ionic flux through the fluid (electrophoresis) and ionic flux with the fluid (electroosmosis). When an electrical field is applied across an electrolyte solution, each individual ion is subjected to a force proportional to the local electric field and the charge on the particle. Additionally, each ionic particle experiences a drag force in the direction opposite the electrical force in proportion to the velocity of the particle relative to the supporting fluid. The balance of these forces causes the particle to attain a final velocity dependent on the particle mass, charge, volume, and electrical field. The electrophoretic current flux can be determined as $\sum_j z_j \mu_j F_c \nabla V$ according to the Nernst-Planck equation, where z_j and μ_j are the valence charge and mobility of a j-th species, respectively, F_c is the Faraday constant, and ∇V is the differential of the electric potential. Electronic mobility of a particular ionic species is often determined by the Stokes-Einstein relationship:

$$\mu_m = \frac{D_j}{k_B T}$$

Equation 2-7

where D_j is the diffusion coefficient of j, k_B is the Boltzmann constant, and T is the temperature.

2.7.2 *Electroosmosis*

Just as the solvent exerts a drag force on mobile ions, mobile ions exert an equal and opposite drag force on the solvent. The force on the solvent can be expressed as a force per unit volume using the term:

$$\vec{F} = F_c \sum_j \left(z_j c_j \right) E$$

Equation 2-8

where $\vec{F}$ is the force per unit volume, c_j is the concentration of the j-th species, and E is the electric field. In a free body diagram, this force would be balanced by friction at the channel wall and viscous interaction at the mouths of the pore. However, these boundary conditions are often difficult or impossible to obtain for a model of nanopore fluidics. For this reason most studies of electrofluidic nanopores are solved numerically. Solving for electroosmosis gives a fluid velocity profile which is typically uniform (plug-like flow). The product of electroosmotic velocity and the concentration gradient in the diffuse layer of the electrical double layer gives a mass flux, which may be converted to an ionic current if geometry and species charge terms are known.

2.8 Modeling a Nanopore Biosensor

   2.8.1 Governing differential equations

   Creating functional models for nanopores is an important part of designing nanopore based biosensors. Having a good understanding of the underlying governing principles will help select better sensor design parameters. For complicated biosensors like nanopores, modeling can provide insight into the interplay of multiphysics phenomena as well as noise levels.

   Numerical modeling of a nanopore is essentially the process of applying numerical techniques to solve differential equations that govern the nanopore system. These

governing differential equations typically include the Poisson equation, Nernst-Planck equation and Navier-Stokes equation. The Poisson equation takes the form:

$$\nabla^2 V = -\frac{\rho_c}{\varepsilon_0 \varepsilon_r}$$

Equation 2-9

where V is the spatial distribution of electric potential, ρ_c is the spatial distribution of charged species, and ε_0 and ε_r represent the vacuum and relative permittivity values, respectively. The charge term ρ_c allows for interaction between all charged species and electric fields, where charged species can be solvated ions or surface charges. The Nernst-Planck equation is given as:

$$\nabla \cdot \left(-D_j \nabla c_j - z_j \mu_{m,j} F_c c_j \nabla V \right) + u \cdot \nabla c_j = R_j$$

Equation 2-10

where D_j is the diffusion coefficient, c_j is the ion concentration, z_j is the ion valence, $\mu_{m,j}$ is the ion mobility, F_c is Faraday's constant, V is electric potential, u is fluid velocity, and R_j is the source term. When solved, the Nernst-Planck equation provides a concentration distribution (as well as other information) for the species of interest. In the case of an aqueous solution of a strong electrolyte, the species of interest are typically the dissociated ions. Coupling between the Poisson and Nernst-Planck equation occurs by feeding the ionic concentration profile into the charge distribution term of the Poisson equation and using the electric fields of the Poisson equation in the electrokinetic terms of the Nernst-Planck equation. Such coupling must be solved iteratively and self-consistently in order to produce a stable solution.

Additional physics (such as electroosmosis or chemical reactions) must also be considered with appropriate differential equations. In the case of electroosmosis, fluid velocity may be defined using a Stokes equation, which is appropriate for low Reynolds number flow. The Stokes equations:

$$\rho_m\left(u\cdot\nabla\right)u=\nabla\cdot\left[-PI+\gamma\left(\nabla u+\left(\nabla u\right)^{\tau}\right)-\frac{2}{3}\gamma\left(\nabla\cdot u\right)I\right]+\vec{F}_V$$

$$\nabla\cdot\left(\rho_m u\right)=0$$
Equation 2-11

account for all fluidic flow parameters, where ρ_m represents the fluid density (not to be confused with ρ_c, the distribution of charges in the Poisson equation), u is the fluid velocity, P is pressure, I is an identity matrix useful for numerical solutions, γ is viscosity, τ is the viscous stress tensor, and $\vec{F}_V$ is a volume force that may be calculated as : $\vec{F}=F_c\sum_j\left(z_j c_j\right)E$.

Fluid flow through nanopores is not usually pressure driven (hindered by the inherent mechanical instability of most nanopore membranes), and electrokinetic terms usually dominate because of the interactions between moving charged particles (from the Poisson/Nernst-Planck equations) and a polar solvent (typically water). When a nanopore is composed of an embedded single walled carbon nanotube, one should also consider the large fluidic slip length at the nanopore wall, which induces nearly frictionless flow through the carbon nanotube [10,31,36,37].

2.8.2 Setting boundary conditions

Setting boundary conditions for a nanopore system can be a complex process, particularly the conditions at the nanopore wall. Issues to consider include: 1) the wall has either free or trapped charges distributed on it, 2) differential potentials due to material work function mismatches, 3) electrical double layer structure, and 4) fluidic conditions, among others. Charge may become trapped in the wall when energetic particles are used to ablate the pore volume, as in e-beam and FIB sculpting. The presence of such trapped charge can alter the electric field within the nanopore, leading to anomalous flow effects. In some cases pH sensitive molecules may be purposely bonded to the pore surface, allowing the operator to control the distribution and charge present on the pore wall [14,38]. In cases where the nanopore is constructed out of conductor/insulator composites (such as single wall carbon nanotube nanochannels), it has been theorized that charges trapped between the conductor and insulator can induce mobile charge on the conductor [10]. The resulting mobile charge distribution would have to be solved for in a manner consistent with the rest of the model. In all of these situations, the actual amount of charge will generally need to be found iteratively by comparing the model output to external references.

EDL is a construct that arises naturally at material interfaces. In models that account for difference in material work functions or consider charges on the pore wall, the diffuse layer forms in the solution following the Poisson/Nernst-Planck equations. However, a continuum model inherently neglects the finite size of the solvated ions, so if the compact layer is to be considered it must be included explicitly. The question remains as to what

the physical thickness of the compact layer should be. The compact layer thickness is typically regarded in the literature to exhibit some variability around a typical value of 0.44-0.46 nm. However, within the interior of a nanopore, this value may be better solved for by comparing the model output to external references through iteratively altering the value.

Any chemical reactions or fluidic slip planes must be considered at the wall of the nanopore. Species in the fluid may undergo surface catalyzed reactions which will change the distribution of species in the electrical double layer. The presence of redox species in the solution should be noted, especially if any portion of the nanopore is electrically biased. Chemical or electrochemical interactions will change the structure of the electrical double layer, which will likely have an effect on the conductance and transport properties of the nanopore [62,72]. Additionally, the fluidic slip length at the nanopore wall should be considered. Some materials (notably single walled carbon nanotubes) have been noted to have very long slip lengths resulting in essentially frictionless flow [31,37]. Correctly determining these conditions will help to ensure accurate modeling of nanopore transport characteristics.

2.9 A case study: effect of EDL on electro-fluidic transport in a SWCNTs nanopore

As mentioned earlier, the ionic conductance through single walled carbon nanotubes (SWCNT) has been observed to be 2-3 orders of magnitude larger than expected based on the geometry of the channel and the conductivity of the solution. In this section, a nanopore system consisting of SWCNTs embedded in a variety of materials is

investigated. The nanopore itself is formed in the lumen of the SWCNT with the embedding material forming an impermeable barrier around the nanopore. Several aqueous electrolyte solutions are examined, and the effects of the concentration of electrolyte on the EDL and transport properties of the pore are noted.

In SWCNTs with radii of 1-2 nm, the dimensions of the EDL are not negligible. The finite thickness of the compact layer of the EDL would effectively reduce the diameter of the carbon nanotube from a fluidics perspective, and changes in nanochannel diameter are known to alter the ionic conductance of a nanopore. The Knudsen number for this system was calculated to be 0.05 based on a mean free path length (λ) given by

$\lambda = \dfrac{MW}{4\pi r^2 N_{avagadro}\rho_v}$ (Equation 2-6) (where MW is the molecular weight of a solvent

molecule, r is the molecular radius - 0.15 nm for a water molecule, and ρ_m is the mass density of the fluid), and a characteristic length of 2 nm (the diameter chosen for a representative single walled carbon nanotube). Based on the small, but transitional Knudsen number, a continuum approach is considered as appropriate to use for modeling this system.

The geometry of the system is defined in an axisymmetric way, to take advantage of the symmetry of the system about a longitudinal axis running through the length at the center of the carbon nanotube. The model consists of cylindrical fluid reservoirs continuous with the interior volume of the nanotube. The nanotube itself is considered as an infinitesimal layer at the boundary of the bulk insulating material and the nanochannel. A compact layer is explicitly modelled as a cylindrical shell at the junction of the

infinitesimal carbon nanotube and the electrolyte fluid. Choosing a thickness for the compact layer presents a complication for the design of the model and is handled in a unique way. In the beginning, the thickness of the compact layer is given a parameterized variable thickness. Once the model is constructed, the thickness of the compact layer is allowed to vary and the model output is used along with a decision rule to identify allowable thicknesses.

Since the model in question is in the continuum regime, the model physics are defined by the Poisson, Nernst-Planck, and Stokes equations as discussed earlier. The Poisson equation is bounded by applied electric potentials at the far ends of the model reservoirs, which set up an electric field to drive ions through the nanopore formed by the carbon nanotube. Additionally, the model accounts for a potential at the surface of the carbon nanotube due to differences in the work function of the insulating materials and the carbon nanotube. The only charged species considered in the model is the solvated ionic species. The transport of electrolytes is governed by the Nernst-Planck equation with a boundary of a constant concentration condition at the far ends of the fluid reservoirs.

A special property of single walled carbon nanotubes is that they have a very long fluidic slip length for fluid transported through the interior nanochannel. The result is practically frictionless flow, which, when electrically driven, is called electroosmosis. Small scale fluid flow may be modelled with the Stokes equation, but because of the slip condition at the wall of the carbon nanotube, the boundary conditions are not well defined (this is actually the reason that an analytical model has not yet been created for

this system). The fluid is driven by a volume force due to electrostatic interaction with solvated ions, and this force is balanced by viscous interactions within the fluid.

With the physics of the model defined, a numerical mesh is constructed. A mesh with rectangular elements is implemented in order to reduce the computational load of the model. In order to obtain numerically converged results, the element size is iteratively reduced while monitoring the model output current at three different locations along the length of the carbon nanotube. Because mass will be conserved, it should be expected that the current at different positions along the length of the nanotube will be the same. An iterative approach is taken in which a mesh is first generated, the model solved, and the current measurements at these three locations compared. The number of elements is increased and the process repeated until the three measurements are close within three significant digits.

Once the mesh is set, the thickness of the compact layer and other parameters of interest are evaluated. Here we are interested in quantifying the thickness of the compact layer when the insulating material and the concentration of the electrolyte solution changes. To do that, we analyze the model under 12 conditions, where each conditional model is given one of three insulating materials and one of four possible solution concentrations. Care is taken in each conditional model: only the parameters of interest are changed and all other conditions and settings are kept identical between models. Each conditional model is solved with a parameterized sweep of eleven values for the compact layer thickness variable.

These conditional models are solved and ionic conductance is determined for each case. Since there are eleven solved conditional models (twelve original conditional models minus one which could not be solved in a reasonable time) and eleven compact layer thicknesses evaluated in each conditional model, 121 output conductance values are collected. Of the selected compact layer thickness values, some are invalid. So a filtering method is developed to eliminate the compact layer thickness values that seem unreasonable. From a survey of the literature it is known that the ionic conductance of single walled carbon nanotube devices is related to the concentration of the solution by a power law $\left(G = Ac^{b}\right)$, where G is conductance, A is a fitting factor, c is the solution concentration, and b is a characteristic exponent. In functional carbon nanotube devices, the exponent (b) is found to be less than 1. So the eleven conditional models were divided up into three separate groups by insulating material to be evaluated separately. Within each subgroup, the concentration and compact layer thickness parameters are iterated into every possible four member ordered list, where each ordered list contains all four solution concentrations. Each ordered list is then fit to a power relationship using a least squares method and a power law exponent and goodness of fit statistic is produced in each case. The ordered lists are then filtered to find lists with exponents meeting the experimental criterion (b less than one) from a good fit to the power relationship. The sorting and filtering of data is automated with custom scripting software, which greatly simplified and organized the process. The scripting approach is necessary due to the large amount of data produced by the eleven models. Since there are three insulating materials

investigated at four concentrations with eleven parametric values for the compact layer thickness, a total of $11^3+11^4+11^4=30613$ outputs are evaluated.
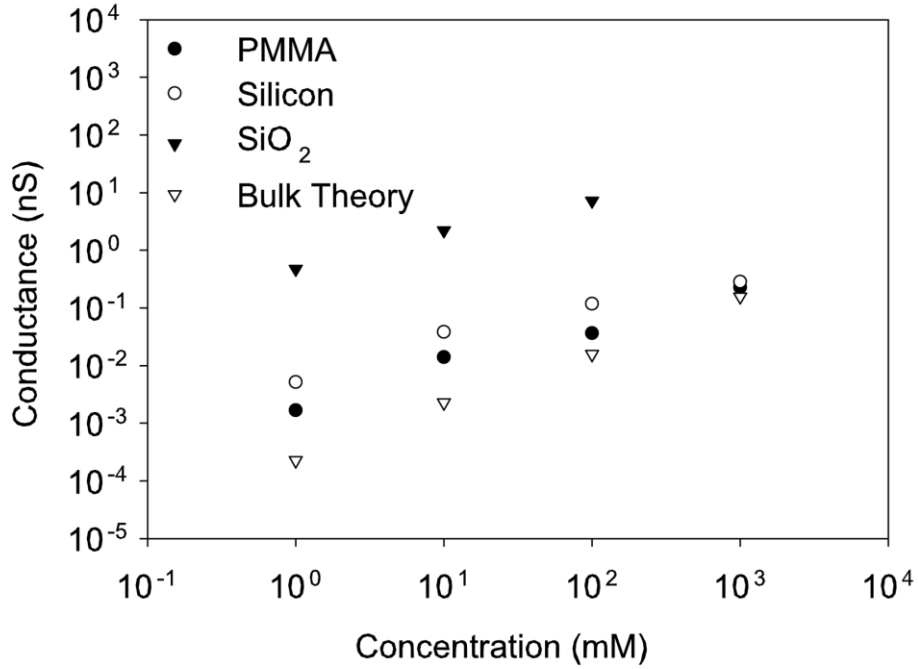
Figure 2.4. The conductance of the SWCNT nanopore is dependent on the work function of the embedding material. Higher work functions and electrolyte concentrations increase the overall conductance of the nanopore.

As shown in Figure 2.4, the conductance values from those models that deemed having a proper compact layer thickness are found to be in the range of 1-3 orders of magnitude greater than that predicted by the bulk conductance theory (Bulk Theory). Empirical checks of electrophoresis and electroosmosis are possible because the numerical computation package used allows for such mechanistic separation. Electrophoresis may

be approximated by the geometric conductance equation $G = \sigma \frac{A}{l}$ (Equation 2-2), where

G is the conductance, σ is the solution conductivity (a function of concentration as discussed earlier), A is the nanochannel cross sectional area, and L is the nanochannel length. When the electrophoretic conductance is calculated in this way using concentration information from the output of the Nernst-Planck equation, good agreement is seen between the empirical relationship and the numerical model, as seen in Figure 2.5.
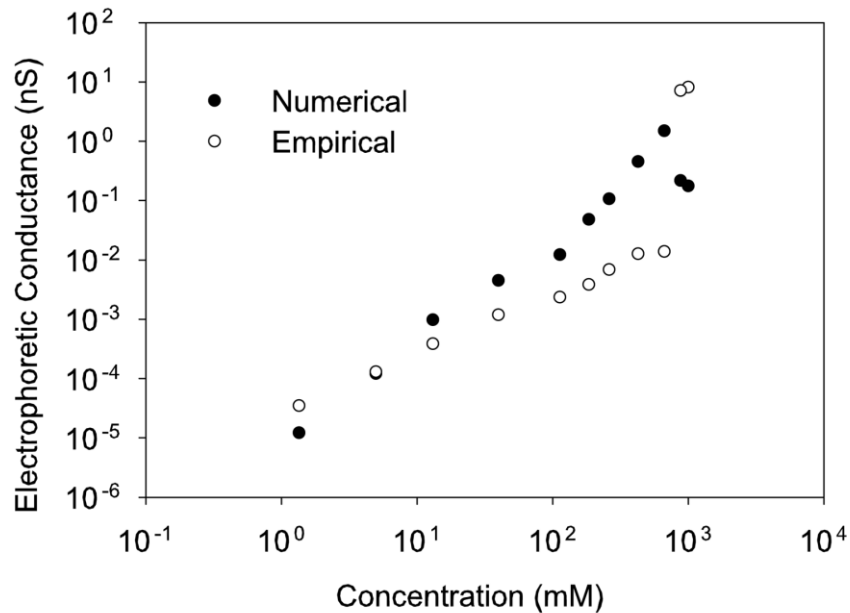
Figure 2.5. The numerical calculation of electrophoretic conductance and the empirically calculated electrophoretic conductance share similar values and relationships with the electrolyte concentration.

A similar test of electroosmosis can be made using the empirical electroosmotic equation $G = \frac{v_{eo}q}{LV}$ and the net charge within the nanotube from the Poisson-Nernst-Planck equations. The electroosmotic velocity in this empirical equation is calculated from $v_{eo} = \mu_{eo}E$, where μ_{eo} is the electroosmotic velocity and E is the applied electric field. μ_{eo} may be calculated from:

$$\mu_{eo} = \frac{\varepsilon_0 \varepsilon_r \xi}{\eta}$$
Equation 2-12

where ξ is the zeta potential, η is the fluid viscosity, and ε_0 and ε_r are the vacuum and relative permittivity, respectively. The empirical relationship reasonably approximates the numerically derived electroosmotic conductance, as seen in Figure 2.6. It should be emphasized that the empirical results presented here were calculated using the concentration and net charge within the nanopore as derived from the numerical model. Thus the good agreement between numerical and empirical methods suggests that the enhanced current conductance can be attributed to the increases in the electrolytic concentration and net change inside the nanopore.
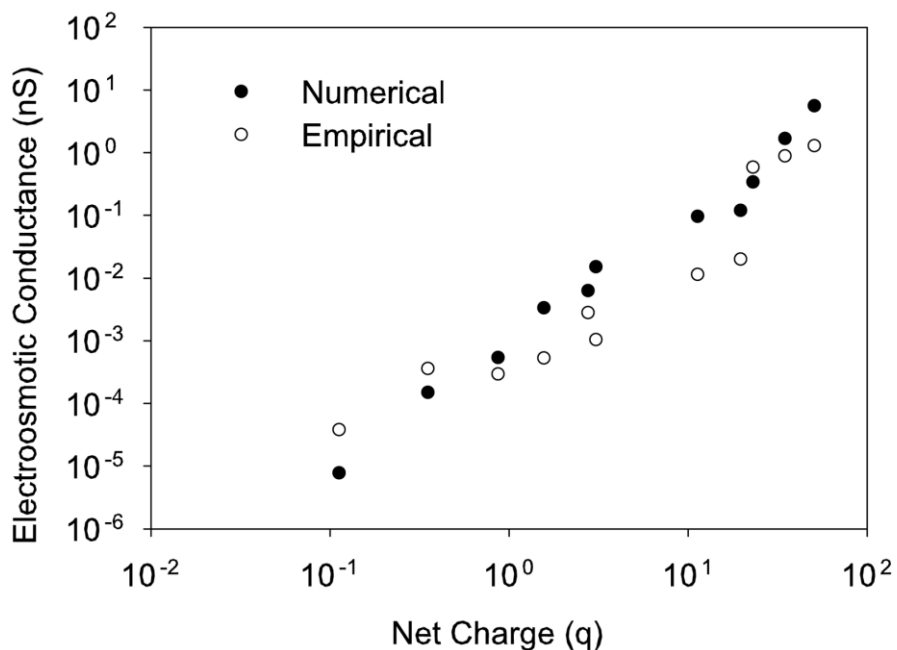
Figure 2.6. The numerical calculation of electroosmotic conductance and the empirically calculated electroosmotic conductance share similar values and relationships with the net charge of the fluid contained within the nanopore.

2.10 Summary and Future Perspectives

The design and analysis of the performance of a nanopore sensor is a complex and exciting subject. The properties of a nanopore may be tuned by carefully choosing proper materials and fabrication methods. Careful selection of materials allows the adjustment of the electrical and fluidic properties of the nanopore, and different fabrication methods may decide the shape of a nanopore device, which in turn may influence the nanopore behavior. While the materials and fabrication methods listed in this chapter are by no

means comprehensive, they nevertheless bring our attentions to the interdependence of the actual nanopore devices upon these selections.

The various modeling techniques discussed in this chapter provide an overview of common methods of deriving the physical basis of observed behavior in nanopores. The effect of the electrical double layer and its dependence on the material properties are of particular importance when modeling pores with truly nanoscale dimensions. The case study presented in this chapter highlights the usefulness of multiphysics computational modeling. With careful execution and iterative investigation, it is capable of shining crucial insights into the operations of a complex nanopore device. While nanopores may become an important class of biosensors, the complex behavior and performance of each new design need to be fully investigated.

CHAPTER 3 : THE EFFECTS OF THE ELECTRICAL DOUBLE LAYER ON GIANT
IONIC CURRENTS THROUGH SINGLE WALLED CARBON NANOTUBES

3.1 Introduction

We developed a computational model to investigate the cause for the high ionic current
through a single walled carbon nanotube (SWCNT) nanofluidic device by considering the
electrical double layer at a solid-liquid interface. With this model, we were able to
examine the influence of the Gouy-Chapman-Stern electrical double layer and solution
concentration on the ionic conductance in the device. Results showed that the
conductance-concentration relationship predicted by our model agreed well with
experimental observation. Moreover, our model showed that the compact layer thickness
increased with the increase of bulk solution concentration, reducing the internal volume
of the nanotube channel available for fluid transport. Fluid within the channel had an
enhanced concentration and a net charge which increased the electroosmotic and
electrophoretic transport properties of the device, increasing the total ionic conductance
of the system.

Electrokinetic flow through nanopores and nanochannels is a subject of active interest
and research. The nanoscale dimensions of these devices enable analysis and
manipulation of small sample volumes on the level of a few molecules. The small scale
of these devices (on the order of a few nanometers) brings in focus issues such as surface
properties, charge accumulations and screening effects, which are typically negligible at
large scales.

Novel effects have been observed in various nanopores and nanochannels including ionic current gating, current rectification, and enhancement of ionic current.[10,59] Nano fluidic devices made of silicon nitride, polyethylene terephthalate, carbon nanotubes and other materials[10,11,77] have been developed and used for interrogating translocating macromolecules.[39,43] Of particular interest to this study is the enhanced ionic conduction observed in nanochannels composed of single wall carbon nanotubes (SWCNTs).[10,37] The large ionic conductance through carbon nanotubes is believed to be enhanced by a nearly frictionless interior surface and electroosmotic flow.[10,31] In elucidating the underlying transport mechanisms, computational modeling with fully coupled Poisson, Nernst-Planck, and Stokes equations has been performed.[10] It was found that when certain amounts of charge were applied to the inner nanotube wall, the observed high ionic current could be accounted for as a result of induced electroosmosis.[10,35]

In all numerical studies of electrokinetics in nanochannels to date,[10,31,37] the structure and effect of the electrical double layer has been neglected. The electrical double layer arises due to a potential difference at an interface between a material and solution causing the ions in the solution to spontaneously rearrange in order to minimize the free energy of the surface/solution system. According to the Gouy-Chapman-Stern theory, an electrical double layer is composed of a compact layer (made of immobilized solvent molecules and specifically adsorbed ions) and a diffuse layer (made of various solvated electroactive and inactive ions). As we previously reported,[72] the effect of the compact layer is negligible at a dimension much larger than the thickness of the electrical double layer (typically given as the Debye length). Neglecting the compact layer in channels

with radii at the scale of the Debye length fails to account for all relevant surface/electrolyte interaction phenomena.

The reason for neglecting the double layer in previous studies, especially the compact layer, may be attributed to the unknown physical dimensions of the compact layer. For example, in explaining Grahame's observation[70] of the double layer effects, Macdonald[71] used a ratio (permittivity to thickness) in place of the compact layer such that no absolute values for the compact layer thickness needed to be defined. Although Macdonald did consider a thickness of 0.44 nm based on a single layer of adsorbed ions and solvent, it was noted in his analysis that the actual thickness was dependent on environmental conditions and could not be simply defined as an adsorbed monolayer. In Grahame's own work,[70] the compact layer was described as ranging from an incomplete monolayer to a multilayer. From these foundational analyses, it becomes clear that the actual thickness of the compact layer is most likely a variable quantity. Additionally, it has been noted that small changes in effective channel radius can have large effects on through-current conductance in carbon nanotubes.[37] Therefore, consideration of an immobile adsorbed layer within a nanotube is imperative.

In this study, we expand on our previously developed computational model[72] that considered the complete Gouy-Chapman-Stern electrical double layer structure to investigate the ionic conductance problem through SWCNTs and to elucidate the cause for the experimentally observed higher than expected ionic currents. With an enhanced model, we can account for many aspects of solution/surface interactions, including the thickness of the compact layer.

3.2 <u>Modeling Considerations</u>

    3.2.1 <u>Geometry</u>

  The nano-channel fluidic system considered in this study consisted of a SWCNT embedded in an insulating material, connecting two reservoirs filled with an aqueous electrolyte. To take advantage of axisymmetry of the SWCNT, the model geometry was constructed in two dimensions with axisymmetry about the central longitudinal axis. Illustrated in Figure 3.1, the longitudinal axis is represented by a dashed line through the centerline of the SWCNT. The length of the channel is equal to the length of the sides of the reservoirs (Figure 3.1). The SWCNT was considered to be an infinitesimally thin layer between the insulating material and the compact layer. A compact layer of thickness (δ) occupies a cylindrical shell at the surface of the channel, whose cross section is represented in Figure 3.1 as a rectangle extending from the edge of the nanotube. The inner edge of the cylindrical shell of the compact layer (right inset, Figure 3.1) was rounded to prevent anomalous flow effects due to sharp corners at the mouth of the SWCNT. A single SWCNT radius was considered in order that the model could be verified against external, experimental studies.
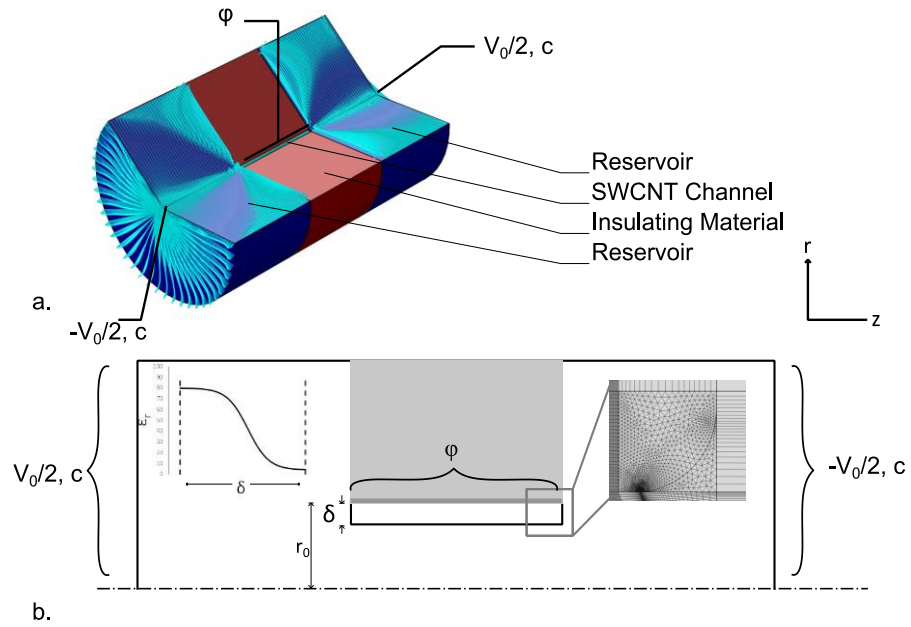
Figure 3.1. An isoperimetric view of the nanofluidic channel showing normalized flow velocity and boundary conditions (a) and a 2-dimensional diagram of the model geometry (b). V_0 represents the applied potential, c represents the constant concentration at the open boundaries of the reservoirs, and φ is the potential at the surface of the SWCNT due to work function mismatches. The model is considered axisymmetric about the central dashed-line with radius (r_0) and compact layer thickness (δ). The SWCNT (dark grey) was considered as an infinitesimally thin layer between the insulating material (black) and the compact layer. Line drawing is not to scale. Left inset: The profile of electrical permittivity varying smoothly in the compact layer. Right inset: The rounded corners of the compact layer were given a fine triangular mesh.

3.2.2 *Governing Equations*

The problem we are dealing with is governed by the coupled Poisson, Nernst-Planck, and Stokes equations. The electric potential throughout the model is governed by the Poisson equation:

$$\nabla^2 V = -\frac{\rho_c}{\varepsilon_0 \varepsilon_r}$$

Equation 3-1

Here, V is the electrical potential distributed throughout the model, ρ_c is the distribution of charges, and ε_0 and ε_r are the vacuum and relative permittivities, respectively. The potential distribution is determined by the applied cross-reservoir potential (V_0) and the differential potential along the outer wall of SWCNT due to the differences in work functions (φ) of the SWCNT and the surrounding insulating material.[78] The distribution of charge carriers consists solely of dissolved ions in solution. Within the compact layer of the electrical double layer, there is no net charge, thus equation (1) reduces to the Laplace equation:

$$\nabla^2 V = 0$$

Equation 3-2

In the compact layer, because the non-uniform distribution of immobilized and adsorbed ionic species, we considered the relative permittivity as varying smoothly from the solution permittivity on the liquid side to the permittivity of the insulating material on the solid side, as illustrated in the left inset of Figure 3.1. In this study, instead of modeling the variation of the permittivity with piecewise hyperbolic functions as has been done previously,[62,72] we simplified the variation profile with a single continuous function:

$$\varepsilon = \frac{\varepsilon_s - \varepsilon_b}{1 + \exp(g * r_0 - h)} + \varepsilon_b$$

Equation 3-3

where ε_s and ε_b are the relative permittivity of the solution and insulating material, respectively, and g and h are parameter functions allowing the sigmoidal permittivity function to be adjusted for different values of channel radius and compact layer thickness. In this study g and h were empirically determined.

The ions in solution undergoing diffusion, electrokinetic motion, and convection are governed by the Nernst-Planck equation:

$$\nabla \cdot \left(- D_j \nabla c_j - z_j \mu_{m,j} F c_j \nabla V\right) + u \cdot \nabla c_j = R_j$$

Equation 3-4

where D_j is the diffusion coefficient, c_j is the ion concentration, z_j is the ion valence, $\mu_{m,j}$ is the ion mobility, F_c is Faraday's constant, V is electric potential, u is fluid velocity, and R_j is the source term. The terms on the left hand side of equation (3) represents diffusion, electrophoresis, and electroosmosis, respectively. Mobility was defined using the diffusion coefficients of the ions and the Stokes-Einstein relationship:

$$\mu_{m,j} = \frac{D_j}{k_B T}$$

Equation 3-5

Because no chemical reactions occur in the device, the source term (R_j) is zero. The bulk solution consists of an aqueous potassium chloride solution of various concentrations. These ions are assumed to be at a constant concentration at the far ends of the reservoirs.

The convective flow of solution in the device is governed by the Stokes equation:

$$\rho_m (u \cdot \nabla) u = \nabla \cdot \left[-PI + \gamma \left(\nabla u + (\nabla u)^\tau \right) - \frac{2}{3} \gamma (\nabla \cdot u) I \right] + \vec{F}_V$$

$$\nabla \cdot (\rho_m u) = 0$$

Equation 3-6

Here, ρ_m represents the fluid density (not to be confused with ρ_c, the distribution of charges in the Poisson equation), u is the fluid velocity, P is pressure, I is an identity matrix useful for numerical solutions, γ is viscosity, τ is the viscous stress tensor, and $\vec{F}_V$ is a volume force that is calculated as: $\left(\vec{F}_V = F_c \sum\limits^{i} (z_j c_j) \cdot \nabla V \right)$. This volume force drives electroosmosis in this model. The interface between the compact layer and the fluid within the nanochannel (the outer Helmholtz plane) is considered as a perfect slip plane, validated by a large slip length in SWCNTs.[31,35,37] Within the simulation, the outer Helmholtz plane serves as a domain boundary. The perfect slip plane exists only at the outer Helmholtz plane, and this does not imply a drag free system. The force on the fluid is proportional to the net charge $\left(q = F_c \sum\limits^{i} (z_j c_j) \right)$. A net charge within the fluid only occurs inside the nanotube where the diffuse region of the electrical double layer disproportionately enhances the concentration of the positive ion. Outside of the nanotube (in the reservoir regions), the net charge is zero and the fluid experiences no electroosmotic force. In the much larger reservoir fluid, the fluid velocity will spread out and dissipate due to changes in geometry and internal viscous interactions. In addition, results will show that the flow rate through the SWCNT is very small (on the order of 1e-8 nL/s), so there will be no appreciable change in reservoir volume within any reasonable

time-scale. Coupling the three sets of equations (Poisson, Nernst-Planck, and Stokes) accounts for all expected transport factors and material interactions in SWCNTs.

3.2.3 *Numerical Considerations*

Ionic conductance and its dependence on bulk solution concentration were obtained for models with SWCNT having radius $r_0 = 1$ nm. For the thickness of the compact layer, since no definite values were given in the literature, we handled it in a unique way by taking advantage of the computational capability: we analysed numerous models in each concentration case with the thickness value varying in the neighborhood of 0.44 nm (a value used by Macdonald [71]). Several insulating materials with different work functions were examined, including poly(methyl methacrylate) (PMMA)[79], silicon dioxide[80], and undoped silicon[78]. All modeling parameters relevant to the system are listed in Table 1. We used a continuum-level finite element package (COMSOL 4.2a) to solve the coupled differential equations numerically. Numerically solving the fully coupled governing equations was computationally intensive and required a fine mesh. Rectangular elements were used for the majority of the domain, with a fine triangular elements defined near the openings of the nanochannel (right inset, Figure 3.1). All elements were of quadratic order. The mesh was iteratively refined until the ionic currents obtained at the middle and near the ends of the nanotube were equivalent to a precision of 3 significant digits.

The use of a continuum approach to modeling is typically justified by the use of the dimensionless Knudsen number. A Knudsen number with a value of less than one typically justifies the use of a continuum model while other methods should be used for larger numbers. The number is commonly used in studies of micro- and nano-fluidics

with good effect.[10,37,75,76] The Knudsen number is calculated by dividing the mean free path of a particle by some characteristic length. A solvent molecule modelled as a sphere with radius 0.15 nm (half the molecular diameter of water) may be used to calculate the mean free path length by the formula:

$$\lambda = \frac{MW}{4\pi r^2 N_{avagadro}\rho_m}$$

Equation 3-7

where λ is the mean free path length, MW is the molecular weight of a solvent molecule, r is the molecular radius (0.15 nm in this case), and ρ_m is the mass density of the fluid. The mean free path is 0.105 nm which produces a Knudsen number of 0.05, when the SWCNT diameter is used as a characteristic system dimension. Other studies of SWCNTs have reported a Knudsen number of 0.15 based on a mean free path length equal to the molecular diameter of water (0.3 nm) and a SWCNT diameter of 2 nm. In either case (Knudsen number of 0.05 or 0.15) the Knudsen value is in a transitional region between statistical and continuum approaches that is inherently difficult to model, and both approaches have been used.[10,37]

Due to the complexity of the numerical model, computation was divided into 12 separate models comprising the 12 conditions considered in this study (3 insulating materials with fluid at 4 different concentrations). All models had identical initial conditions and meshes, differing only in the material parameters of the insulating materials and solution concentration. Within each model, the compact layer thickness was parameterized and evaluated at 11 values ranging around the expected value (0.44 nm). Computation was performed on the Palmetto Cluster at Clemson University.

Solution time per model was typically around 40 hours on an 8 core node with 256 GB of memory. A solution for the model with SiO2 and a concentration of 1000 mM could not be completed in a reasonable time frame, and was therefore neglected in the system analysis. Output data for all conditions (total ionic conductance, concentration, insulating material, and compact layer thickness) was parsed with custom JavaScript code to systematically identify concentration/conductance relationships consistent with experimental observation (conductance/concentration relationships defined by a power law with exponent b<1). Over 30,000 (114+114+113) combinations of model parameters were systematically analysed using this method.

Table 1. Constants, variables, and values.

Symbol	Description		Unit
c	Concentration of the bulk solution in the reservoirs		millimolar
c_j	General concentration term for solvated electrolytes		millimolar
c_{nt}	Effective ion concentration within the nanochannel		millimolar
D_j	Diffusion coefficient for solvated electrolytes	D_{Cl}	$2.03e\text{-}5(cm^2/s)$
		D_K	$1.96e\text{-}5(cm^2/s)$
δ	Thickness of the compact layer		nm
ε_r	Relative permittivity		
ε_0	Permittivity of free space		$8.8542e\text{-}12$ (F/m)
ε_b	Permittivity of the device substrate	SiO_2	3.9
		Si	11.68

Symbol	Description		Value / Units
		PMMA	3.0
ε_s	Nominal permittivity of the electrolyte solution		80
F_c	Faraday's constant		96485.34 (C/mole)
$\vec{F}_V$	Volume force		N/m^3
G	Conductance		nS
G_{eo}	Electroosmotic conductance		nS
G_{ep}	Electrophoretic conductance		nS
g	Fitting term for smoothly varying permittivity in the compact layer		
γ	Fluid viscosity		Pa s
h	Fitting term for smoothly varying permittivity in the compact layer		
I	Identity matrix		
J_i	Volume flow rate		nL/s
k_B	Boltzmann's constant		1.38065e-23 (J/K)
L	SWCNT length		nm
λ	Mean free path length		nm
μ_{eo}	Electroosmotic mobility		m^2/(V s)
$\mu_{m,j}$	Mobility of solvated electrolytes	$\mu_{m,Cl}$	8.23e-13(s mole/kg)
		$\mu_{m,K}$	7.95e-13(s mole/kg)
P	Pressure		Pa
φ	Surface potential at the SWCNT due to work function differences	SiO$_2$	-1.49 V
		Si	-60 mV
		PMMA	-20 mV
q	Net charge on the diffuse layer within the nanochannel		Charge numbers
r_0	Radius of the SWCNT		nm
R_j	Rate of production of solvated electrolytes		mole/(s m^3)
ρ_c	Distribution of charge carriers within the model		C/m^3

ρ_m	Fluid mass density		kg/m^3
σ	Electrolyte solution conductivity		S/m
T	Temperature		296.65 (K)
τ	Viscous stress tensor		
u	Fluid velocity		m/s
V	General potential term within model		Volts
V_0	Potential applied across the length of the channel		0.0125 (V)
z_j	Valence of solvated electrolytes	z_{Cl}	-1
		z_K	+1
ζ	Zeta potential		V

3.3 Results and Discussion

Figure 3.2 shows the variation of total conductance obtained as a function of bulk concentration for different insulating materials (with their differential work functions given in parentheses). As a reference, the curve representing the conductivity according to bulk theory ($G = \sigma \dfrac{\pi r_0^2}{L}$ in which G is conductance, σ conductivity, r_0 SWCNT radius, and L SWCNT length) is also given to serve as a baseline from which the enhanced conductance of SWCNTs may be measured. It appears that the amount of conductance enhancement corresponds to the level of the differential work function between the surrounding insulating material and the SWCNT. The most enhancement occurs in models with SiO$_2$ ($\varphi = -1.49$ V) and the least occurs with model with PMMA ($\varphi = -0.02$ V). Nevertheless, the conductance of these models ranges from one to three orders of magnitude higher than the bulk reference level. The conductance of the SiO$_2$

model at 1000 mM could not be computationally solved in a manner consistent with the other parameters within a reasonable time frame, therefore the parameter was omitted in order to ensure the output parameters were comparable. The conductance for all these models follow power law relationships with bulk solution concentration and fall in the ranges reported in literature. The experimentally observed relationship reported in the literature between concentration and conductance may be characterized by a power fit $\left(G = Ac^b\right)$, where G is conductance, c is concentration, and the exponent (b) from the fit is less than one.[35] By performing regressions to the modeling results we found that $G = 0.002c^{0.6836}$, $G = 0.0071c^{0.5705}$ and $G = 0.5012c^{0.5925}$ for the PMMA, silicon and SiO_2 cases respectively (with concentration in millimolar). Clearly, all the exponents are less than one. This is also the criterion we used to exclude the values for the compact layer thickness (from a range of values we modelled) that produce an exponent larger than one (see detailed discussion later).
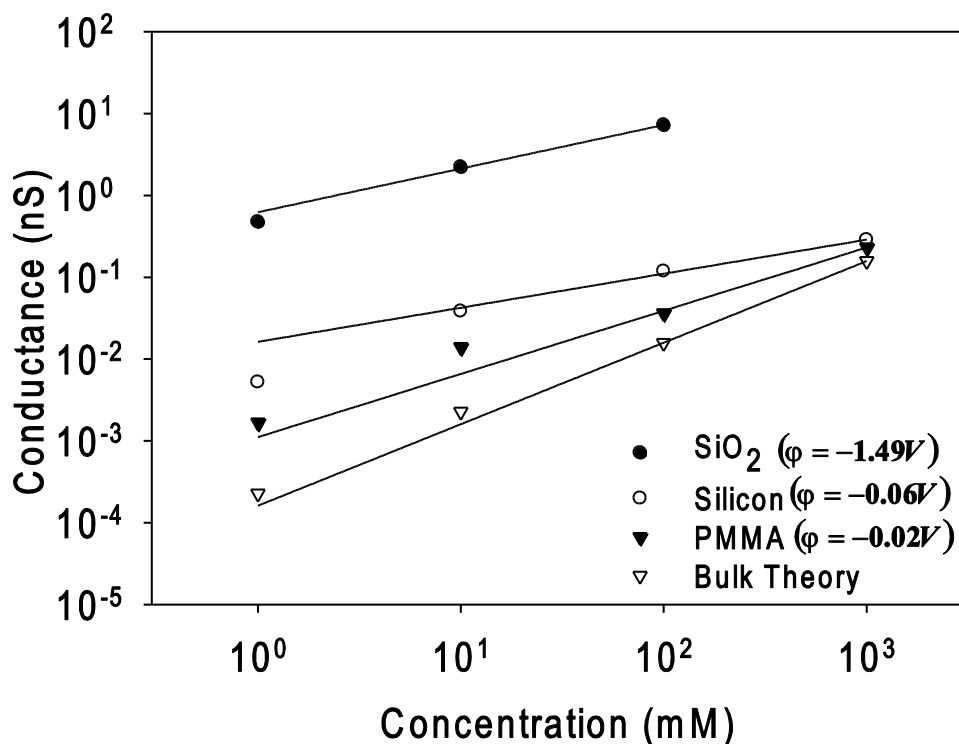
Figure 3.2. Total conductance of the model follows a power relationship with bulk solution concentration. The total conductance predicted by this model falls within the expected ranges and is enhanced by 1-3 orders of magnitude over the conductance predictions based on the bulk conductivity theory.

The mechanisms driving the enhancement in conductance are complex and highly dependent on the net charge and effective ion density within the SWCNT. Figure 3.3 shows the relationship between the net charge (expressed in the number of elementary electron charges) of the fluid within the nanotube and bulk solution concentration. In general, the net charge in the nanotube increases with bulk solution concentration. However, devices that possess larger differential work functions produce greater net charge in the SWCNT at all bulk solution concentrations. For instance, the net charge for models with SiO_2 as the insulating material is greater than that in models with silicon.

Likewise, the net charge in models based on silicon is greater than that in devices composed of PMMA. The relationships between net charge within the nanochannel and bulk solution concentration follows power law relationships. For the results shown in Figure 3, we found $q = 0.002c^{0.6836}$ for PMMA, $q = 0.0071c^{0.5705}$ for silicon, and $q = 0.5012c^{0.5925}$ for SiO$_2$, where q is the number of charges on the diffuse layer within the nanochannel and c is bulk solution concentration in millimolar. Because of the small radius of the nanochannel, the negative differential work function along the SWCNT will make the channel ion selective, leading to preferential exclusion of negative ions. Thus the conductance current is carried primarily by positively charged ions.
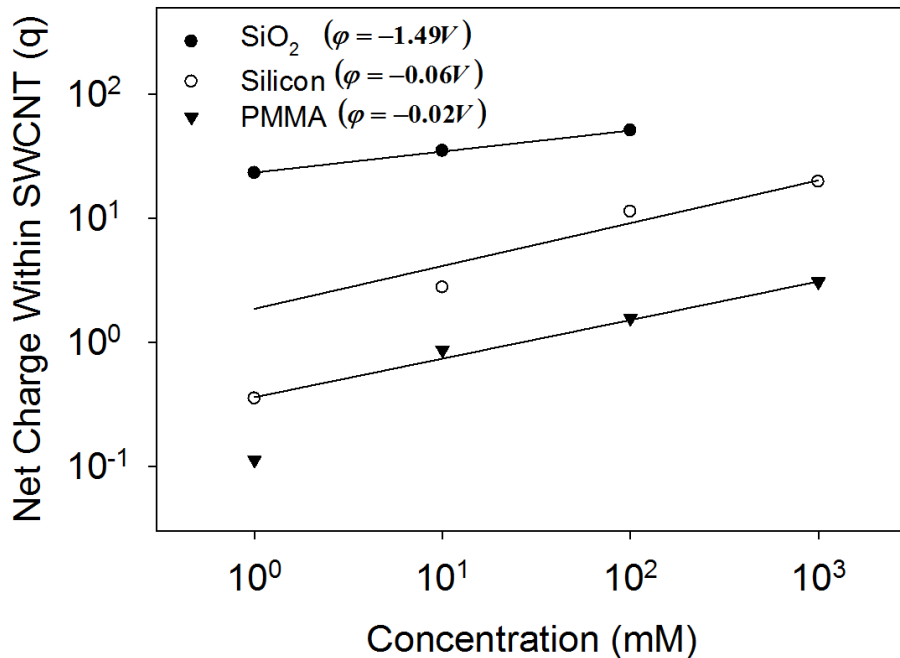
Figure 3.3. The net charge of the fluid within the nanochannel is related to the differential work function at the SWCNT wall and the bulk solution concentration. An increase in either parameter tends to increase the net charge in a power law relationship. Models

constructed from materials that yield a higher differential work function (SiO$_2$/SWCNT)

produce higher charges, and a lower charge is likewise associated with the materials that

produce a lower differential work function (PMMA/SWCNT).

Figure 3.4 shows that the electroosmotic conductance is related to the net charge within

the SWCNT in a linear relationship for each insulating material considered. This is as

expected since devices with larger differential work functions will generate larger net

charges in the nanochannel (see Figure 3.3). Quantitative relationships are found via best

fit as $G_{eo} = 0.1915q - 4.4187$ for SiO$_2$, $G_{eo} = 0.0067q - 0.0019$ for silicon, and

$G_{eo} = 0.0053q - 0.0027$ for PMMA, respectively. At macroscale, electroosmotic

conductance may be calculated in terms of zeta potential (potential at the outer Helmholtz

plane, ζ), permittivity, viscosity, and net charge (q) as $G = \dfrac{\mu_{eo} q}{L V_0}$, where $\mu_{eo} = \dfrac{\varepsilon_0 \varepsilon_r \zeta}{\gamma}$.

This equation predicts a linear relationship between electroosmotic conductance and net

charge, as was the case observed in our numerical results.
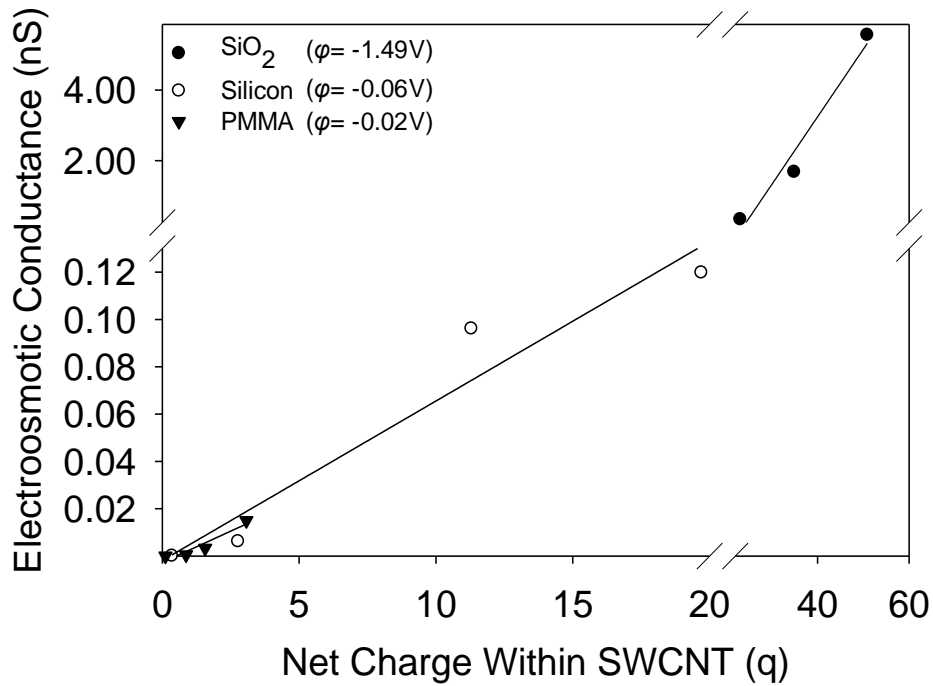
Figure 3.4. The electroosmotic conductance of the device varies with the net charge

within the SWCNT. The electroosmotic conductance is governed by net charge (via the

electrokinetic volume force) and viscous fluid interactions (via Equation 3-6, the Stokes

equation).

Figure 3.5 illustrates the spatially varying profiles of various parameters related to the

electrokinetic flow through the SWCNT system both within the nanochannel and near the

channel opening. Variations in pressure are given in Pascals and vary around values of

0.2e6 Pa, which is roughly twice atmospheric pressure. The ion selectivity of the

nanochannel may be observed in surface plots in Figure 3.5, where the concentration of

K^+ ions is enhanced within the SWCNT while the concentration of Cl^- ions is lower

within the channel compared to the reservoir. The electrical potential near the opening of

the pore decreases due to interaction between the driving potential (V_0), charges within

the fluid (ρ_c), and the potential at the wall of the SWCNT (φ). The velocity profile of the fluid within the nanochannel is characterized by plug-like flow that does not vary in the radial or axial dimensions. The 2-dimensional surface plot of fluid velocity in Figure 3.5 illustrates a transition region within the first 3 nm of the SWCNT channel, as well as the uniform velocity profile within the length of the nanochannel. The flow rate of solution through the SWCNT is related to the fluid velocity by the cross sectional area of the nanochannel (area given by $\pi \cdot (r_0 - \delta)^2$). The flow rate exhibits a power relationship with solution concentration and proportionality with the differential work function, given by $J_{SiO_2} = 4e - 8c^{0.4137}$, $J_{Si} = 1e - 9c^{0.4097}$, and $J_{PMMA} = 4e - 10c^{0.3311}$, where J_i is volume flow rate in nL/s and c is bulk solution concentration in millimolar. The flow rate is very small and will not move an appreciable amount of fluid between the reservoirs. For example, it would take more than 100 years to transport 1 μL of fluid at the highest observed flow rate. In this simulation, there is no fundamental limit to the volume of fluid that may be transported through the nanochannel due to the assumption of continuous fluid at the reservoir boundaries.
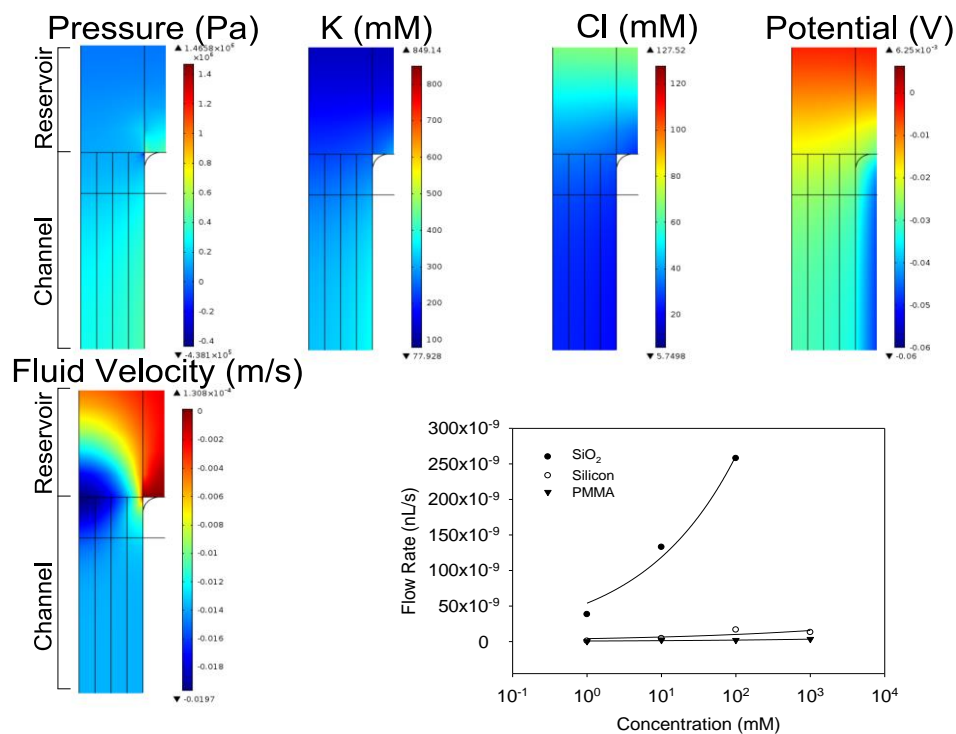
Figure 3.5. The spatial distribution of various fluidic parameters. A zoomed in region from a representative model (Silicon at 100mM) shows the spatial variation within the nanopore and in the reservoir near the SWCNT opening (the left boundary of the surface plots correspond to the axis of symmetry in the model). Note that the flow and concentration surface plots are restricted to the reservoir and channel while the potential surface plot extends over the reservoir, channel, and insulating material. The volume flow rate of the fluid through the SWCNT shares a power relationship with the solution concentration and is proportional to both concentration and differential work function.

Figure 3.6 compares the effective ion concentration (considering both positive and negative species as essentially equivalent charge carriers in terms of mobility and limiting molar conductivity) within the SWCNT with bulk solution concentration. The effective ion concentration follows a trend similar to that of net charge versus concentration: it

63

increases via a power relationship with the differential work function of the device and bulk concentration. The relationships may be quantified as $c_{nt} = 263.73c^{0.2027}$ for SiO$_2$, $c_{nt} = 5.8474c^{0.7401}$ for silicon, and $c_{nt} = 1.3884c^{0.9554}$ for PMMA, where c_{nt} is the effective ion concentration within the nanochannel and c is the bulk solution concentration (c and c_{nt} are in units of millimolar). The average ion concentration within the nanochannel is typically higher than the bulk concentration, with higher ion concentrations correlating to materials that possess a higher differential work function (Figure 3.6). The accumulation of charged species within the nanochannel due to the work function increases the total number of charge carriers within the channel. Furthermore, due to the constriction of the internal SWCNT volume by the compact layer (the finite nature of the compact layer will be discussed later), the concentration of ions within the nanochannel must increase. Thus the fluid that flows through the SWCNT differs from the bulk solution in that it carries a net charge and has an increased effective ion concentration. This in turn leads to enhanced electroosmotic and electrophoretic conductance.
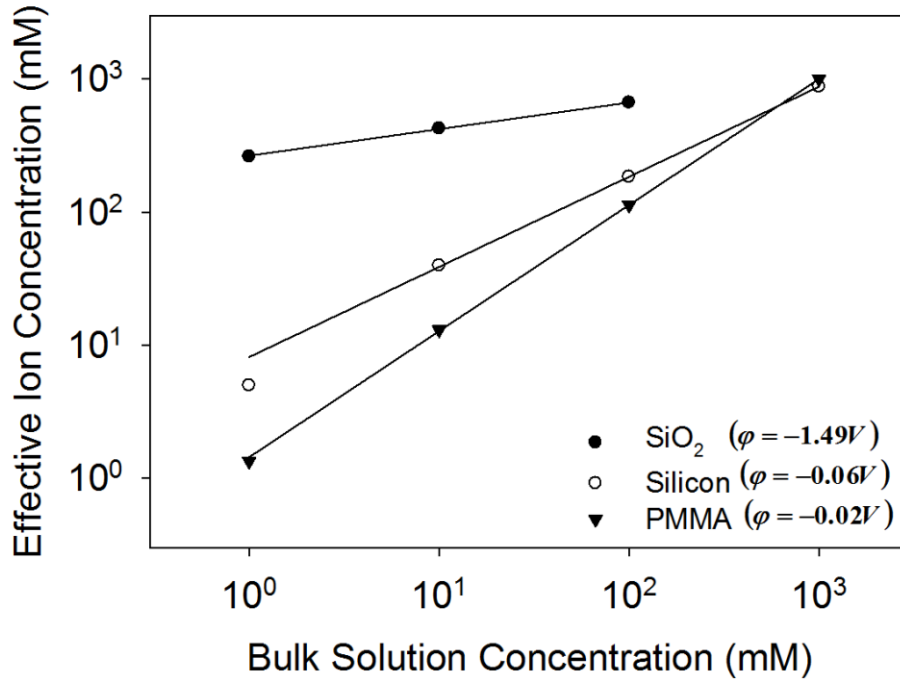
Figure 3.6. The effective ion concentration of the fluid within the SWCNT typically differs from the bulk solution concentration. The accumulation of charged species within the channel is due to charge selectivity of the SWCNT. The effective ion concentration increases with both bulk solution concentration and differential work function.

Figure 3.7 shows that the obtained electrophoretic conductance is proportional to the effective ion density of the solution within the SWCNT in a power relationship ($G_{ep} = 10^{-5} c_{nt}^{1.6049}$, where G_{ep} is the electrophoretic conductance in nanosiemens and c_{nt} is the mean ion concentration in millimolar). Electrophoresis is charge independent when solutes have comparable mobility and limiting molar conductivity (as potassium and chloride do) and thus may occur in electroneutral or charged solutions. Because of the relatively large size of the reservoirs, the overall conductance of the device is governed

by the solution within the nanotube. The electrophoretic conductance of the SiO_2 model is further enhanced by electrical distortions from the large electric field due to the high differential work function and ion accumulation. The enhanced ion concentration within the nanochannel therefore leads to electrophoretic conductance that is larger than predictions based on the concentration of the bulk solution alone. The combined mechanisms of electroosmosis and electrophoresis serve to produce device conductance that is orders of magnitude larger than what would be expected based on the bulk solution conductivity.
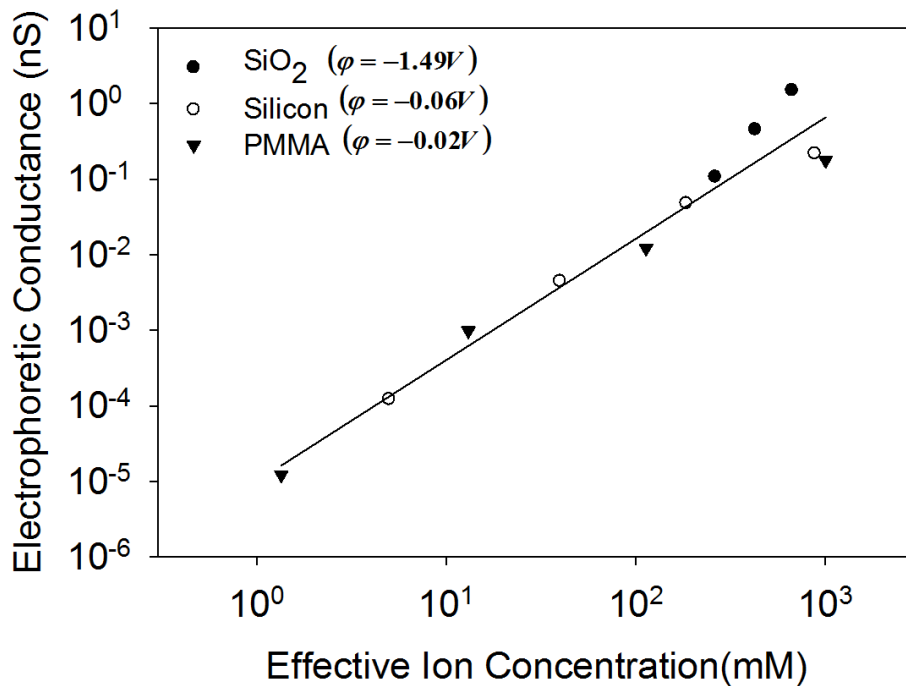
Figure 3.7. The electrophoretic conductance within the device is proportional to the average solution concentration within the SWCNT. The fluid inside SWCNT typically has a higher effective ion concentration than the bulk fluid (Figure 3.6) and therefore a higher conductivity.

Figure 3.8 shows the electrophoretic and electroosmotic components of conductance as functions of bulk solution concentration. The relationships all follow power laws and are proportional to bulk solution concentration and differential work function. The relationships of electroosmosis and electrophoresis with bulk solution concentration may be quantified by power laws, SiO$_2$: ($G_{eo} = 0.364c^{0.6067}, G_{ep} = 0.1118c^{0.5726}$), silicon: ($G_{eo} = 0.0003c^{0.9899}, G_{ep} = 0.0002c^{1.0785}$), and PMMA: ($G_{eo} = 2 \cdot 10^{-5} c^{1.0641}, G_{ep} = 2 \cdot 10^{-5} c^{1.3574}$), where G_{eo} is the electroosmotic conductance, G_{ep} is the electrophoretic conductance, and c is the bulk solution concentration in millimolar. The relative magnitude of the two transport mechanisms depends on the differential work function. Electroosmotic conductance in SiO$_2$ ($\varphi = $ -1.49 V) is larger than its electrophoretic counterpart due to the high net charge present when SiO$_2$ is considered as the insulating material. For the case of silicon ($\varphi = $ -0.06 V), the electrophoretic and electroosmotic components are of nearly equal magnitude. As the differential work function further decreases (in the case for PMMA, $\varphi = $ -0.02 V), a reverse situation is seen where the conductance is primarily driven by electrophoresis.
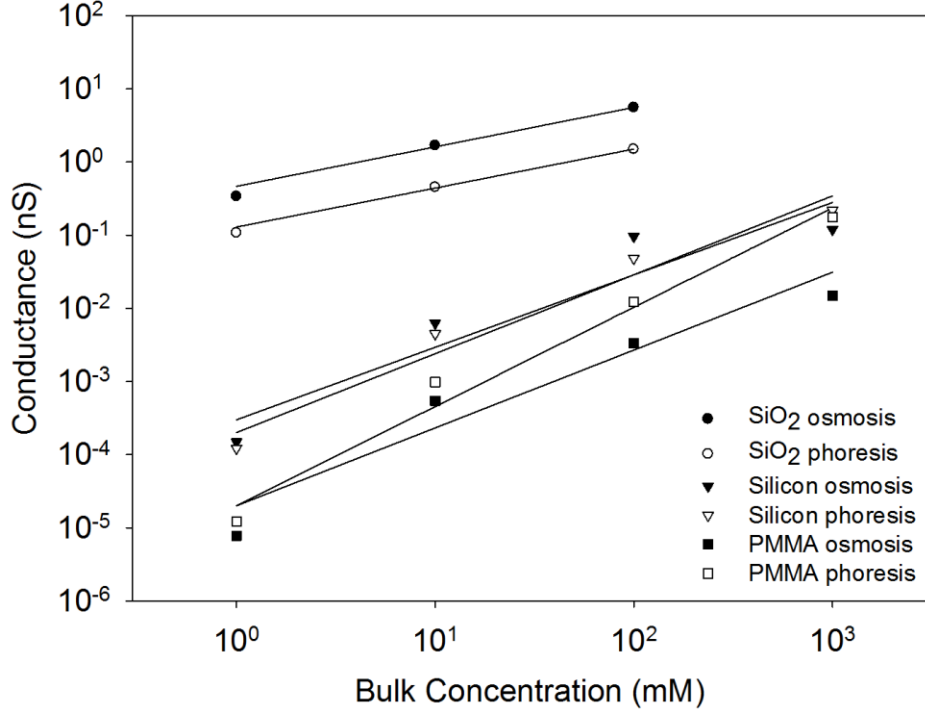
Figure 3.8. The electroosmotic and electrophoretic components of the conductance predicted by the model are enhanced differently in terms of differential work function. Electrophoresis dominates when the differential work function is small (as in the case of PMMA, $\varphi = -0.02V$) and electroosmosis dominates when the differential work function is large (as is the case of SiO$_2$, $\varphi = -1.49V$). For the case of silicon ($\varphi = -0.06V$), electroosmosis and electrophoresis contribute nearly equally.

As we pointed out earlier, the compact layer, which is filled with immobilized ions and molecules, extends a finite distance from a material/solution interface, restricting the internal volume of the SWCNT. Changes to the internal volume of a SWCNT can have large effects on the ionic conductance.[37] Based on the models we developed in this study, we also performed quantitative analysis of the thickness of the compact layer. In all models analysed we allowed the thickness of the compact layer to vary in each

concentration case and deemed the thickness value to be reasonable if the resulting power relationship between conductance and concentration $\left(G = Ac^b\right)$ has an exponent b <1. To do this, we considered thickness values in the neighborhood of 0.44 nm ranging from 0.1 nm at the lower end to 0.7 nm at the upper end. Thicknesses of less than 0.3 nm (the molecular diameter of a solvent molecule) were included to simulate the effect of a compact layer with the thickness of an incomplete monolayer. The approximation of an incomplete monolayer as a cylindrical shell was allowed in this model on the basis that the system exists in the transitional Knudsen regime, as discussed in the Numerical Considerations section. Additionally, the outer Helmholtz plane may exist within dimensions less than the diameter of adsorbed molecules as a plane of closest approach.[71,72] Figure 3.9 shows the ranges of the reasonable compact layer thickness at various concentrations for various differential work function conditions found in this model. Interestingly, the reasonable value for the compact layer thickness is found to vary from half the thickness of an adsorbed monolayer of solvent (0.15 nm) when the bulk concentration is low to the thickness of a stacked multilayer (0.66 nm) when the bulk concentration is high. Moreover, this thickness range is consistent with the electrochemical theories of Grahame and Macdonald, as discussed in the Introduction.[70,71] In a general trend, the compact layer thickness increases as bulk concentration increases regardless of the level of differential work functions, suggesting that the thickness of the compact layer is affected more by the availability of ions in solution and less by the differential work function. By pooling all reasonable values for

the compact layer thickness from all cases together we found it follows a sigmoidal

relationship with the concentration of the bulk solution in millimolar:

$$\delta = \frac{0.6167}{1 + e^{-\left(\frac{c-9.73}{13.27}\right)}}$$

Equation 3-8

A likely explanation for the sigmoidal behavior of the compact layer thickness is that

because of the decreased screening length of solvated ions at high concentrations, more

ions must adsorb to the surface in order to screen the differential work function at the

wall of the SWCNT, resulting in a thicker compact layer. That the compact layer

thickness is related to the bulk concentration is critical to the functioning of this type of

device. A change in the thickness of the compact layer will alter not only the internal

volume of the SWCNT but also the dielectric conditions inside, resulting in different net

charge and effective ion density within the channel.
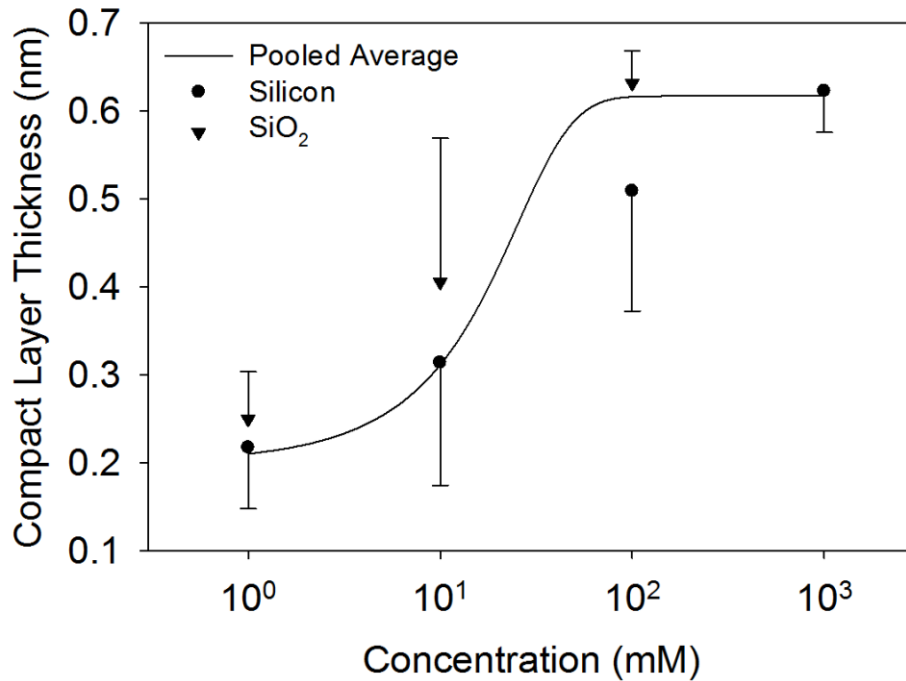
Figure 3.9. The thickness of the compact layer varies with bulk solution concentration. The average thickness is found to form a sigmoidal relationship with bulk solution concentration. For illustration clarity, data for the silicon case are not shown but they fall within the same range and are considered in the pooled average.

In summary, we found that the electrokinetic flow through a SWCNT was governed by many factors. The concentration of the bulk electrolyte solution regulated the availability of charge carriers in the system and the thickness of the compact layer. As a result, the conductance of the model increased with the bulk solution concentration as has been observed in experimental studies of similar devices. The work function of the material in which the device was constructed is responsible for the potential built-up at the surface of the SWCNT which alters the net charge and effective ion density within the channel. The increase in net charge and ion density cause enhancement of both electroosmosis and

electrophoresis, contrary to previous studies that indicated that the enhanced conductance was overwhelming due to increased electroosmosis.[10,35] Additionally, the differential work function potential makes the channel charge selective, contributing to the enhancement of electroosmosis that has been observed experimentally. The differential work function and the bulk concentration of the solution drive the immobilization of species inside the electrical double layer, which in turn regulates the nanochannel conductance.

3.4 Conclusion

A theoretically rigorous computational model of electrokinetic flow through a single walled carbon nanotube was presented. By including an explicitly defined Stern layer with a smoothly varying dielectric permittivity and accounting for the work functions of the SWCNT and surrounding insulating materials, the model presented a complete Gouy-Chapman-Stern electrical double layer and provided a thorough study of the effect of the electrical double layer on the electrokinetics in nanofluidic channels. With this model, we were able to investigate the mechanisms governing the electrofluidic conductance through SWCNT without applying any artificial boundary conditions. From this study we found that both electroosmosis and electrophoresis were enhanced when the nanofluidic device had an insulating material possessing a work function larger than that of SWCNTs as well as when the bulk concentration is high. This study also offered, for the first time, quantitative prediction of the thickness of the compact layer.

CHAPTER 4 : ACTIVE CURRENT GATING IN ELECTRICALLY BIASED
CONICAL NANOPORES

4.1 <u>Introduction</u>

We observed that the ionic current through a gold/silicon nitride (Si_3N_4) nanopore
could be modulated and gated by electrically biasing the gold layer. Rather than
employing chemical modification to alter device behavior, we achieved a control of
conductance directly by electrically biasing the gold portion of the nanopore. By stepping
through a range of bias potentials under a constant trans-pore electric field, we observed a
gating phenomenon in the trans-pore current response in a variety of solutions including
Potassium Chloride (KCl), Sodium Chloride (NaCl), and Potassium Iodide (KI). A
computational model with a conical nanopore was developed to examine the effect of the
Gouy-Chapman-Stern electrical double layer along with nanopore geometry, work
function potentials, and applied electrical bias on the ionic current. The numerical results
indicated that the observed modulation and gating behavior was due to dynamic
reorganization of the electrical double layer in response to changes in the electrical bias.
Specifically, in the conducting state, the nanopore conductance (both numerical and
experimental) is linearly proportional to the applied bias due to accumulation of charge in
the diffuse layer. The gating effect occurs due to the asymmetric charge distribution in
the fluid induced by the distribution of potentials at the nanopore surface. Time
dependent changes in current due to restructuring of the electrical double layer occur
when the electrostatic bias is instantaneously changed. The nanopore device demonstrates

direct external control over nanopore behavior via modulation of the electrical double layer by electrostatic biasing.

Electrokinetic mass transport through nanopores often has unusual characteristics, such as enhanced current, current rectification, or current gating.[10,59] Enhanced ionic currents have been observed in single walled carbon nanotubes and current rectification has been demonstrated in conical and double conical nanopores.[10,14,32,59] Characterization of the mechanisms governing the behavior of these nanoscale systems is necessary in order to aid design of practical devices, such as biosensors with sub-molecular resolution.[16,20,81,82] However, nanopore behavior is often difficult to explain in a way that is consistent with empirical behavior and accepted theory. Current gating is one feature which lacks a comprehensive explanation.

The rectification behavior of certain nanopores has been shown to often be the product of asymmetry, arising from the geometry (in the case of conical nanopores) or applied surface charge.[11,59] Rectification or gating of ionic currents may be controlled by construction of a conical nanopore with a uniform surface charge, or by applying a non-uniform surface charge to a cylindrical nanopore.[60,69,83] Typically, in order to control the rectification properties of a nanopore, the interior of the nanopore is coated with pH-sensitive ligands via thiol chemisorption.[14,59,61] The rectification behavior of nanopores prepared in this way follow a predictable, pH-dependent trend. When the pH is at the isoelectric point of the bound species, no rectification is observed, but when the bound species are charged, the current is rectified. However, such studies neglect the relationship between work function, electrical double layer, and rectification behavior.

In conical nanopores with unmodified surfaces, the ionic current may still be rectified.[14,49,84] The mechanism behind this kind of rectification is typically attributed to unknown surface charge implanted during nanopore formation and geometric asymmetry. However, it has been shown that the mechanisms attributed to surface charge may, in some cases, be explained by considering the effect of the potential at the surface of the nanopore due to material work functions.[32] It is known that pH can alter the differential work function potential at solution/material interfaces.[85] Such an effect may be responsible for the pH-sensitive character of unmodified conical nanopores, though this effect is clearly overridden in cases where the surface has been deliberately modified with pH sensitive species. Consideration of the effects of the Gouy-Chapman-Stern electrical double layer and work function potentials have typically been neglected in these systems.[70,71] The electrical double layer and surface potential have been shown to have non-negligible effects in the mechanism of enhanced ionic conduction in single walled carbon nanotubes and should also be considered in conical nanopores.[32]

The work function potential and the Gouy-Chapman-Stern electrical double layer have been shown to be mechanistically consistent with the unique behavior of nanochannels.[32] The electrical double layer consists of a compact layer of specifically adsorbed ions or solvent molecules at the liquid/material interface and a charged diffuse layer extending into the fluid.[70,71] Previous studies have indicated that while the double layer structure arises due to potential differences at the material surface, the thickness of the compact layer is dependent on the composition of the solution and ranges from an incomplete monolayer to a stacked multilayer.[32,70,71] The complete electrical double layer transitions

to the bulk solution with a rate constant defined by the Debye length. In nanopores with radii on the scale of the Debye length, overlap may occur in the diffuse layer, producing the characteristic ion selectivity observed in nanoscale pores and the unusual behavior of these nano-devices. Controlling the electrical properties at the nanopore surface will allow tailoring of device behavior by manipulation of the electrical double layer.

Because of the inflexibility of chemically modified nanopores, there is a need to develop a nanopore that allows active modification of behavior. The properties of chemically modified nanopores are defined at time of fabrication. Chemically modifying nanopores to achieve rectification in a reproducible manner is a difficult-to-control process requiring iterative fabrication and testing. In the nanoscale regime, slight variations in nanopore geometry can have significant effects on nanopore performance. In sensor applications where the geometry and electrical properties of the nanopore can affect signal quality, tight control of nanopore behavior is needed. While it is possible to tune surface-modified nanopore properties to a particular application, doing so requires changes to nanopore chemistry or fabrication of new nanopores. Control through an application of electrical potential would allow the device's behavior to be modified in real-time. Active control over nanopore conductance would permit the creation of a large number of uniform devices by correcting individual variation at time of use. In sensing applications, active control would allow real-time optimization of acquisition while reducing costly fabrication steps. Control over nanopore conductance would include the ability to gate the nanopore, introducing the possibility of electrically actuated nanoscale valves and pumps.

4.2 <u>Methods</u>

    4.2.1 <u>Experimental Methods</u>

Suspended membranes were prepared on undoped silicon wafers using conventional photolithographic processes. The suspended membranes consisted of a layer of silicon nitride (Si_3N_4) and a layer of gold (Au). Gold was bonded to the Si_3N_4 layer with a titanium adhesion layer. Nanopores were prepared in the Si_3N_4/Au membranes using focused ion beam (FIB). The initial diameter of these nanopores was confirmed to be between 100 and 200 nm via scanning electron microscopy (Figure 4.1a). The nanopore diameter was subsequently reduced by electroplating gold at a current of 200 nA. The change in nanopore geometry was monitored by periodically measuring the nanopore conductance in 100 mM aqueous KCl solution. Plating was discontinued once conductance decreased to 10-20 nS, corresponding to a minimum diameter of <10 nm, typically after 40 minutes of plating.[39,59]

Prepared chips were placed in a custom fluidics cell filled with electrolyte solutions of various concentrations (Figure 4.1b). These solutions included NaCl, KCl, and KI in concentrations between 10^0 and 10^{-7} M at pH of 4, 7, and 10. Trans-pore potential generation and simultaneous ionic current measurement was accomplished with a patch clamp amplifier (Molecular Devices, Axopatch 200B, CA) and two silver/silver chloride (Ag/AgCl) electrodes. Current traces were recorded using custom data acquisition software (National Instruments, Labview, TX), acquired at a rate of 142 Hz. Prior to each measurement, the measured ionic current was zeroed by adjusting the potential across the Ag/AgCl electrodes. The zero current condition occurred at a potential of 150 mV

between the Ag/AgCl electrodes indicating that a naturally occurring electric field is intrinsic to the nanopore. The gold plated surface of the nanopore was electrically biased by a potentiometer (Princeton Applied Research, Versastat MC, TN) in ascending and descending steps of equal magnitude and duration through the gold contact pad on the chip (Figure 4.1b).

a.
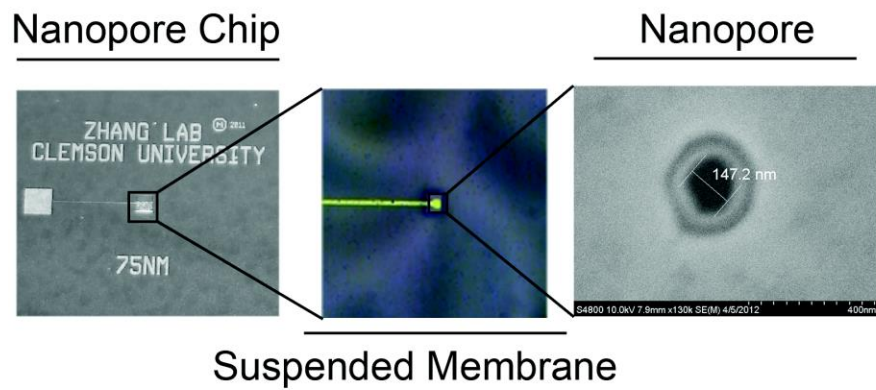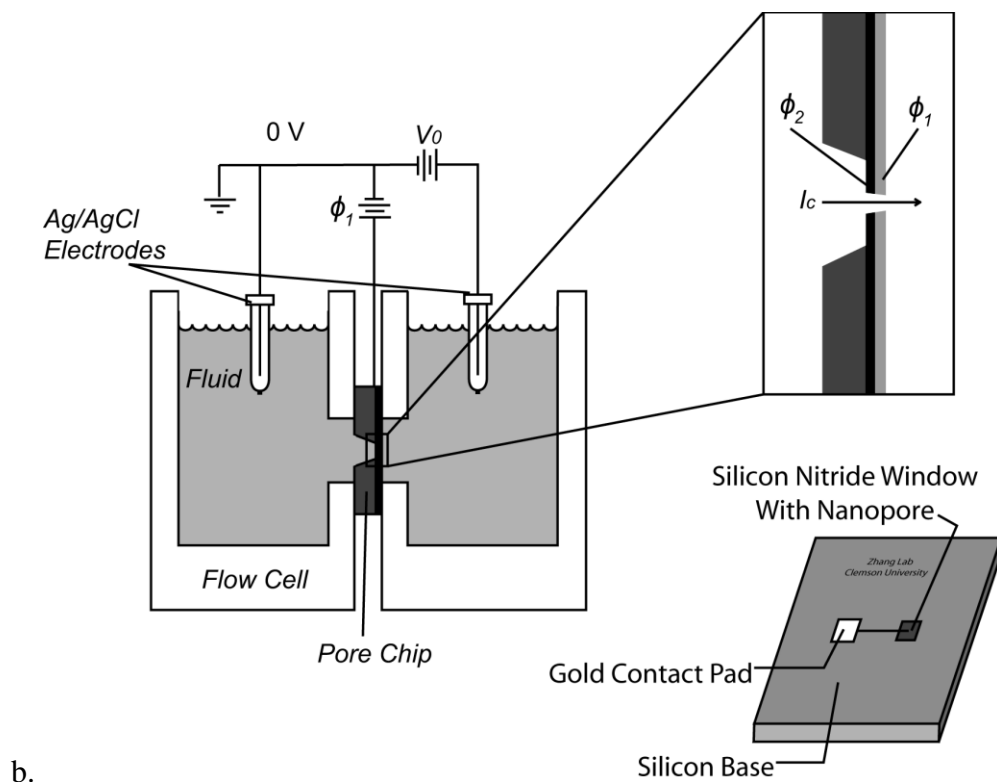
Figure 4.1. a. A nanopore chip contains a gold contact pad and a suspended gold and
Si$_3$N$_4$ membrane. The diameter of the nanopore, as fabricated, was confirmed by
scanning electron microscopy to be within 100 to 200 nm. b. The nanopore chip was
sandwiched between two halves of a custom flow cell. A driving electric field was
established between the fluid reservoirs and the resulting ionic current is detected with
two Ag/AgCl electrodes. The gold surface of the nanopore is electrically addressed
through the contact pad on the chip.

4.2.2 *Modeling Considerations*

The 2-dimensional axisymmetric model used in this study (illustrated in Figure 4.2) is
an extension of previous work considering the fluidic behavior of nanopores.[32] The

nanopore system considered in this study consisted of a conical shaped nanopore formed in a membrane consisting of two thin layers (one of Si_3N_4 and one of gold). The potential at the nanopore surface is defined by the applied electrical bias (φ_1) on the gold portion and work function potential (φ_2) on the Si_3N_4 portion (values given in Table 2).[32,62,72] Ionic current was obtained for axisymmetric conical nanopore models with a variety of geometric configurations, solutions, and electrical conditions. Steady state and time dependent results were obtained. We used a continuum-level multiphysics finite element modeling package (Comsol 4.2a) to solve the governing equations simultaneously. Computation was performed on the Clemson Palmetto Cluster with 8 cores and up to 450 GB of memory.

4.2.3 Governing Equations

Electrokinetic nanofluidic flow is described by the Poisson, Nernst-Planck, and Stokes equations. The electric potential is governed by the Poisson equation:

$$\nabla^2 V = -\frac{\rho_c}{\varepsilon_0 \varepsilon_r}$$

Equation 4-1

V is the distribution of potential through the model, ρ_c is the distribution of charges in the model, and ε_0 and ε_r represent the vacuum and relative electrical permittivities, respectively. The potential distribution is bounded by a longitudinal electric field applied between the far ends of the reservoirs (V_0, Figure 4.2), the applied bias (φ_1), and work function potential (φ_2) at the wall of the nanopore. ρ_c describes only the distribution of

ions in the fluid. The compact layer of the electrical double layer, by definition, has zero net charge, so within the compact layer region the Poisson equation simplifies to $\nabla^2 V = 0$. The electrical permittivity of the fluid and nanopore were defined by the materials (given in Table 2).

The compact layer consists of immobilized solvent and adsorbed ionic species with a net charge of zero. Due to the non-uniform distribution of species within this layer, we considered the permittivity of the compact layer to vary smoothly from the permittivity of the nanopore material to the permittivity of the fluid. We used a previously validated sigmoidal function to define the smoothly varying permittivity within the compact layer.[32,62,72]

$$\varepsilon = \frac{\varepsilon_s - \varepsilon_p}{1 + \exp(gr_0 - h)} + \varepsilon_p$$
Equation 4-2

Here, ε_s and ε_p represent the permittivities of the solution and pore material, respectively. The term r_0 is the local radius of the nanopore, which in a conical geometry is a function of position along the length of the nanopore. The fitting terms g and h were empirically determined to fit the curve within the compact layer.

Diffusive flux, electrophoretic flux, and electroosmotic flux of dissolved ions in the fluid are governed by the Nernst-Planck equation:

$$\nabla \cdot \left(-D_j \nabla c_j - z_j \mu_{m,j} F_c c_j \nabla V \right) + u \cdot \nabla c_j = R_j$$
Equation 4-3

81

Here D_j is the diffusion coefficient, c_j is the concentration distribution, z_j is the ion

valence, and $\mu_{m,j} = \dfrac{D_j}{k_B T}$ is the mobility of species j. F_c is Faraday's constant. V is the

distribution of electric potential defined by the Poisson equation. R_j is a production term

for any chemical reactions that occur in the system, however because the fluid is a

simple, bivalent, aqueous electrolyte, no chemical reactions are expected. The solution is

given a constant concentration at the far ends of the reservoirs (c_0, Figure 4.2).

The flow of solution through the nanopore is governed by the Stokes equation:

$$\rho_m (u \cdot \nabla) u = \nabla \cdot \left[-PI + \gamma \left(\nabla u + (\nabla u)^\tau \right) - \frac{2}{3} \gamma (\nabla \cdot u) I \right] + \vec{F}_V$$

$$\nabla \cdot (\rho_m u) = 0$$

Equation 4-4

Here, ρ_m is the fluid density, u is the fluid velocity, τ is the viscous stress tensor, P is

pressure (no pressure gradients were applied to the model), γ is viscosity, I is an identity

matrix, and $\vec{F}_V$ is an electroosmotic volume force. The volume force

$\left(\vec{F}_V = F_c \overset{i}{\Sigma}\left(z_j c_j \right) \cdot \nabla V \right)$ results from interactions between the polar solvent and mobile

charged species in the fluid. Since the compact layer is adsorbed to the surface of the

nanopore, the nanofluidic flow is bounded by the plane of closest approach of the

compact layer (the outer Helmholtz plane). In some nanofluidic systems (particularly the

case of single walled carbon nanotubes), there is evidence that a perfect fluidic slip

condition occurs at the outer Helmholtz plane.[10,31,32,37] However, there is no evidence of a

slip plane in conical Si_3N_4 nanopores and inclusion of a slip condition in this model did

not significantly increase the ionic current or the contribution of electroosmosis.[60] Therefore, in this model, a no-slip fluidic boundary condition was set at the outer Helmholtz plane. Coupling the Nernst-Planck, Poisson, and Stokes equations fully describe the nanofluidic system.
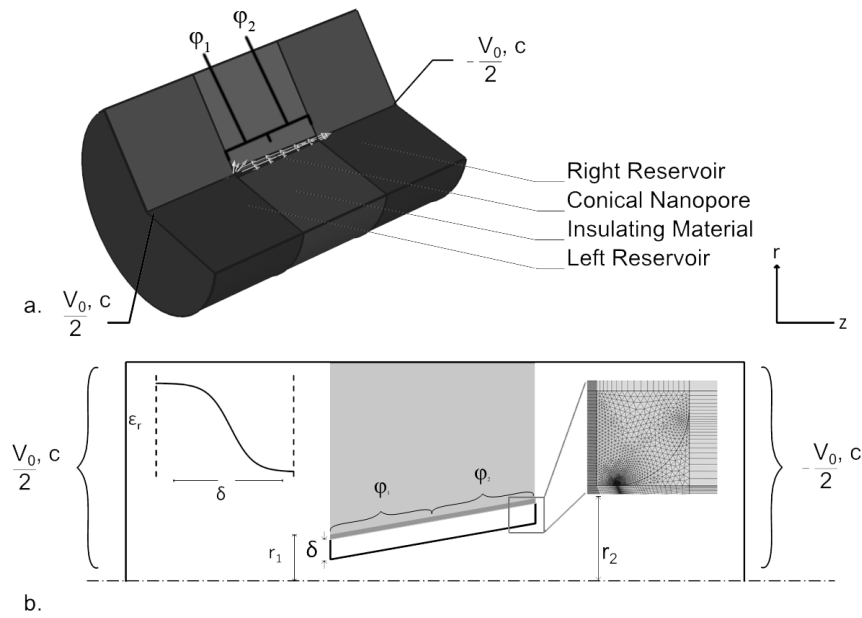
Figure 4.2. a. An isoperimetric view of the nanopore model geometry. b. A representation of the axisymmetric (about the dashed line) model. *Left Inset:* The permittivity of the compact layer was defined as smoothly varying between the permittivity of Si_3N_4 ($\varepsilon_r = 7.5$) and the permittivity of the solution ($\varepsilon_r = 80$). *Right Inset:* The inner edges of the compact layer were rounded in order to reduce computational difficulty at the mouths of the nanopore. V_0 is the applied trans-pore potential, c is the concentration of the bulk fluid, δ is the thickness of the compact layer (0.44 nm was used as an average value, based on previous work[32,71]), φ_1 is the bias

83

applied to the wall of the nanopore through the gold layer, φ_2 is the unbiased surface potential of the Si$_3$N$_4$, and r_1 and r_2 are the radii of the small and large openings of the conical nanopore, respectively.

Table 2. Constants, variables, and values.

Symbol	Description		Unit
A	Average cross sectional area of the conical nanopore		nm^2
a	General power law coefficient		1
b	General power law exponent		1
c	Concentration of the bulk solution in the reservoirs		millimolar
c_j	General concentration term for solvated electrolytes		millimolar
D_j	Diffusion coefficient for solvated electrolytes	D$_{Cl}$	$2.03 \cdot 10^{-5}$ (cm^2/s)
		D$_K$	$1.96 \cdot 10^{-5}$ (cm^2/s)
		D$_I$	$2.05 \cdot 10^{-5}$ (cm^2/s)
		D$_{Na}$	$1.33 \cdot 10^{-5}$ (cm^2/s)
δ	Thickness of the compact layer		0.44 nm
ε_r	Relative permittivity		
ε_0	Permittivity of free space		$8.8542 \cdot 10^{-12}$ (F/m)

ε_p	Permittivity of the device substrate	Si$_3$N$_4$	7.5
ε_s	Nominal permittivity of the electrolyte solution		80
F_c	Faraday's constant		96485.34 (C/mole)
$\vec{F}_V$	Volume force		N/m^3
G	Conductance		nS
G_{eo}	Electroosmotic conductance		nS
G_{ep}	Electrophoretic conductance		nS
g	Fitting term for smoothly varying permittivity in the compact layer		
γ	Fluid viscosity		Pa s
h	Fitting term for smoothly varying permittivity in the compact layer		
I	Identity matrix		
$J_{ep,j}$	Electrophoretic flux		mol/s
Kn	Knudsen number		1
L	Nanopore length		nm
μ_{eo}	Electroosmotic mobility		m^2/(V s)
$\mu_{m,j}$	Mobility of solvated electrolytes	$\mu_{m,Cl}$	$8.23 \cdot 10^{-13}$ (s mole/kg)
		$\mu_{m,K}$	$7.95 \cdot 10^{-13}$ (s mole/kg)
		$\mu_{m,I}$	$8.31 \cdot 10^{-13}$ (s mole/kg)

		$\mu_{m,Na}$	$5.39 \cdot 10^{-13}$ (s mole/kg)
P	Pressure		Pa
φ_1	Bias applied to the gold surface of the nanopore		V
φ_2	Surface potential due to the material work functions		-0.2 V
r_0	Radius of the nanopore at an arbitrary position		nm
r_1	Radius of the small opening of the nanopore		nm
r_2	Radius of the large opening of the nanopore		nm
R_j	Rate of production of solvated electrolytes		mole/(s m^3)
ρ_c	Distribution of charge carriers within the model		C/m^3
ρ_m	Fluid mass density		kg/m^3
σ	Electrolyte solution conductivity		S/m
T	Temperature		296.65 (K)
T_L	Laplace time constant		s
τ	Viscous stress tensor		
u	Fluid velocity		m/s
V	General potential term within model		V
V_0	Potential applied across the length of the channel		0.15 (V)
V_{vol}	Volume of the biased portion of the nanopore		nm^3
z_j	Valence of solvated electrolytes	z_{Cl}	-1

z_K	+1
z_I	-1
z_{Na}	+1

4.3 Results and Discussion

4.3.1 Gating behavior

In nanopores with a relatively small minimum diameter (as a result of iterative gold plating), a strong gating effect was observed. Figure 4.3a shows the steady-state trans-pore conductance due to electrical bias (φ_1) applied to the gold layer. While under an external electric field (V_0), the electrical bias was modulated between -600 mV and + 600 mV in 200 mV incremental steps. The current response was large under negative bias and small under positive bias, indicative of variable on/off states. Under positive bias, the trans-pore conductance was nearly constant and not significantly different from zero, indicating that the net ionic current is eliminated due to gating. Figure 4.3b shows a typical current trace over time. We estimate the minimum diameter ($2r_1$) of the nanopore to be <10 nm based on the fact that this type of rectification typically occurs only for nanopores with sufficiently small diameter.[39,59] Figure 4.3a also shows the steady-state trans-pore conductance obtained from numerical modeling. The numerical conductance exhibits a similar trend as the experimental one. Specifically, under positive bias, it is constant and near zero (-2.79 ± 3.31 nS), representing an off state, and under negative bias it increases linearly with the magnitude of the electrical bias, representing an on

state. From the modeling we further noted that the slight difference between the numerical and experimental results may be attributed to the variation in the taper angle of the conical nanopore wall. As shown in Figure 4.3a, by varying the taper angle we observed that the experimental results were enveloped on both the upper and lower sides by the numerical wide-angle and narrow-angle models, respectively. The steady-state conductance response of the nanopore under positive and negative biases is due to the net polarity of the majority ions within the nanopore (Figure 4.3c). When the bias is negative, the ions in the biased and unbiased regions have the same polarity, allowing a homogeneous ion flux (which is governed by nanopore geometry, solution concentration, and bias magnitude, as previously discussed). When the bias is positive, the opposing polarities of the ions in the biased region and the unbiased region result in a non-conducting state due to the ion selectivity of the nanopore region. Under a constant, cross-pore potential, the ions in the two regions will be driven in opposite directions, but be unable to move through the opposing region due to the charge selectivity of the electrical double layer imposed by the surface potential.
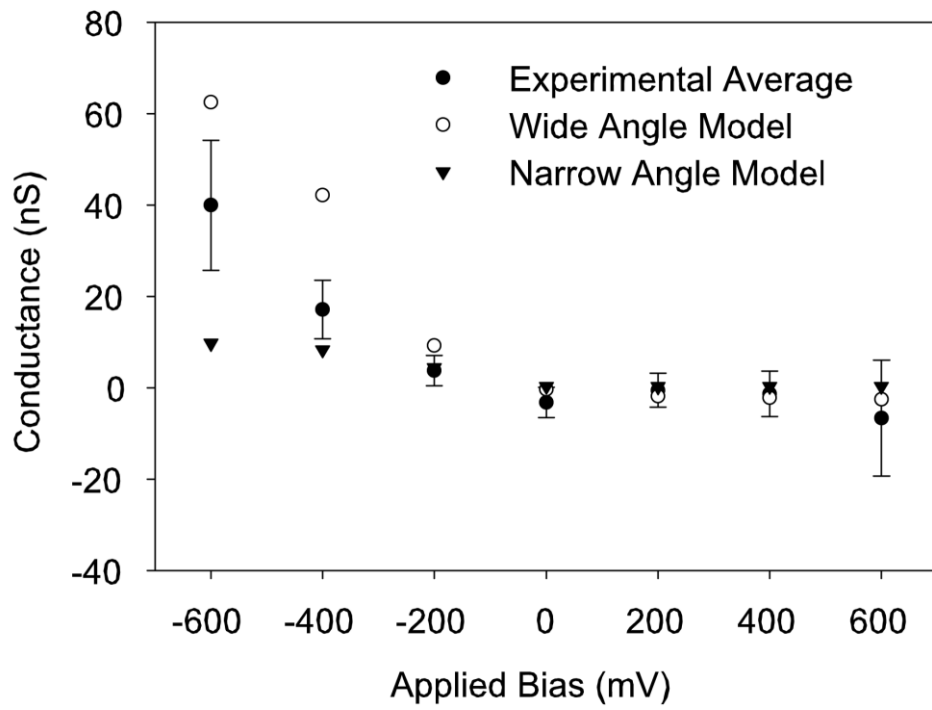
a.
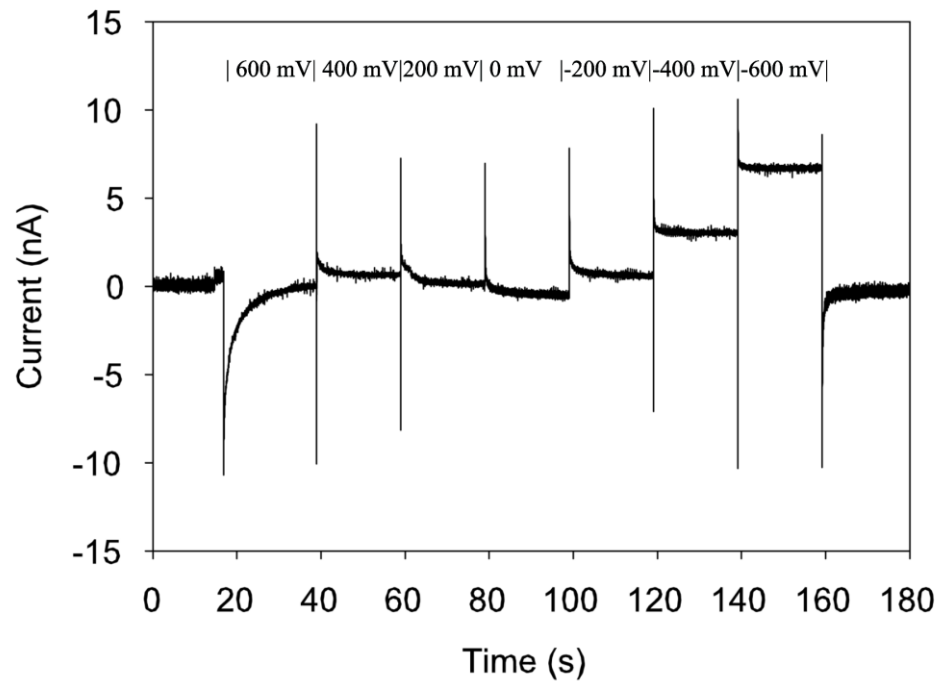
b.
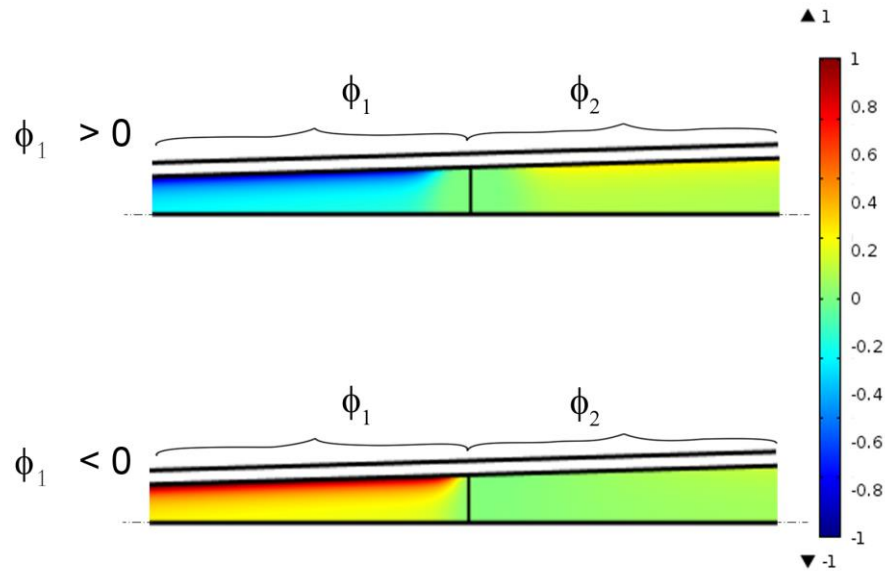
c.

Figure 4.3. a. The conductance through the nanopore under a constant trans-pore potential (V_0) was a function of the bias applied to the nanopore (φ_1) and the taper angle of the nanopore wall. The narrow angle model refers to a model with a ratio of r_1:r_2 of 1:2 and the wide angle model refers to a model with a 1:4 ratio (1.15° and 3.43°, respectively). b. The current was recorded as the bias potential (φ_1) was stepped through a range of values (here from 600 mV to -600 mV in -200 mV steps). Current and conductance measurements were taken from the steady-state region. c. The polarity of the charged fluid stored in the nanopore is opposite the polarity of the surface potential. When the applied bias (φ_1) and unbiased surface potential (φ_2) have the same negative polarity, the fluid carries a net positive charge throughout the nanopore. When the

applied bias $\left(\varphi_1\right)$ is positive and unbiased surface potential $\left(\varphi_2\right)$ is negative, the fluid is divided into regions with net negative and net positive charge, respectively, resulting in the off state of the nanopore.

4.3.2 *A look into transport mechanics*

From the numerical models, we noted that the ionic conductance is mainly driven by electrophoretic conduction and not much by electroosmosis. Figure 4.4a shows the trans-pore conductance due to electrophoresis and electroosmosis under the applied electrical bias along with the estimated electrophoretic conductance. Under negative bias, the electrophoretic conductance can be related to the applied bias by a linear best-fit relationship $\left(G_{ep} = -0.0122\varphi_1 + 1.9\,\text{nS}, \quad \varphi_1 < 0\right)$. The estimated electrophoretic conductance $\left(G_{ep,est} = -0.004\varphi_1 + 1.9149\,\text{nS}, \quad \varphi_1 < 0\right)$ is derived from the average conductivity of the solution and the geometry of the nanopore $\left(G_{ep} = \sigma\dfrac{A}{L}\right)$, where L is the length of the nanopore and A is the average cross-sectional area, and conductivity (σ) is estimated from the ionic strength. The linear relationship between the ionic conductance and applied bias in the on state was found surprising, given the complexity of ionic transport in a nanopore. However, the linear relationship was confirmed by a good fit in both experimental and numerical results ($R^2 = 0.9412$ in experiment, $0.9630 < R^2 < 0.9635$ in the numerical models). Here the enhancement of electrophoretic conductance over the estimated value is indicative of the contribution of a net charge in the diffuse layer. Clearly, the electrophoretic conductance under positive bias is small

($G_{ep} = -8 \cdot 10^{-5} \varphi_1 - 0.3069 \, \text{nS}, \; \varphi_1 > 0$), corresponding to an off state. In such an off state, φ_1 and φ_2 (the work function of the Si_3N_4 layer) have opposite electrical polarities, thus resulting in regions with mutually exclusive ion selectivity that is believed to inhibit a net trans-pore current. On the other hand, under all the bias potentials considered in this study, the contribution of electroosmosis is negligible ($G_{eo} = 5 \cdot 10^{-6} \varphi_1 - 0.0025 \, \text{nS}$). Even though electroosmosis is responsible for the large currents observed in cylindrical nanochannels,[10,32] the conical shape of this nanopore inhibits any significant contribution from electroosmosis.

From our modelling results, we also found that the conductance response is related to the taper angle of the nanopore and the work function (or surface potential, φ_2) of the unbiased region. The slope of the on state conductance response (Figure 4.3a) could be replicated in the numerical model by increasing the taper angle (from 1.15° to 3.43°) or by increasing the magnitude of the unbiased surface potential from $\varphi_2 = -0.2V$ to $\varphi_2 = -0.3V$. While the unbiased surface potential is considered as a material property related to the work function, in practice the potential may vary due to unintentional changes to the crystalline structure or ion doping during the FIB fabrication step. The taper angle affects the geometry-induced resistance of the nanopore (similar to the way that increasing the minimum diameter of the nanopore decreases resistance, increasing the taper angle decreases resistance), and φ_2 affects the nanopore conductance response by altering the ionic strength and charge in the unbiased region (a similar effect is seen in single walled carbon nanotubes with various surface potentials [32]). The electrophoretic

conductance (G_{ep}) through a nanopore is governed by $G_{ep} \propto \int J_{ep,j} dA$, where $J_{ep,j}$ is the electrophoretic flux $\left(J_{ep,j} = -D_j \left(z_j c_j \nabla V \right) \right)$, and $A = \int dA$ is the minimum cross sectional area in a conical nanopore. Within the nanopore, the potential term (V) is locally modulated by the surface potentials φ_1 and φ_2. The net charge $\left(z_j c_j \right)$ carried by the electrolyte is proportional to the nanopore surface potentials. From the definition of electrophoretic flux, we see that the charge induced flux is also proportional to the diffusion coefficient of the charged species. Therefore the electrophoretic conductance (G_{ep}) may be considered to be a function of potential and geometry factors, $G_{ep} \propto \left[-D_j \varphi_2 \left[A \right] \right]$. Based on this expression, we wonder whether the conductance response of the nanopore is mediated primarily through the surface-potential route or a geometric route. Since the surface potential (φ_2) of the unbiased region is material related (and constant in a given nanopore), we decided to seek answers by using electrolytes with different diffusion coefficients. So, if it is through the surface-potential (φ_2) route, nanopore conductance should be expected to be sensitive to change of the charged species (e.g., K^+ or Na^+), and if through the geometric route the conductance should be insensitive to change of species.

Numerical models were constructed with either elevated unbiased surface potential magnitude (φ_2, the high potential model) or with a larger taper angle (increased large radius r_2, the wide angle model) and evaluated in either KCl or NaCl solution. Numerical models with increased angle and potential were used in order to amplify any effect for comparison purposes. The obtained results were compared with the measured

conductance in KCl or NaCl solution. Figure 4.4b shows the differential conductance

between KCl and NaCl for each model and from the experiment. Clearly, the differential

conductance of the high potential (φ_2) model is more sensitive to the biasing potential

than the wide angle model. The differential conductance of the narrow angle model was

not significantly different from that of the wide angle model (data not shown, taper angle

of 1.15° and $\varphi_2 = -0.2V$). The experimental result displays very weak sensitivity to the

change in supporting electrolyte. These results suggest that the nanopore conductance is

mainly affected by its geometry rather than chance alteration of the unbiased surface

potential.
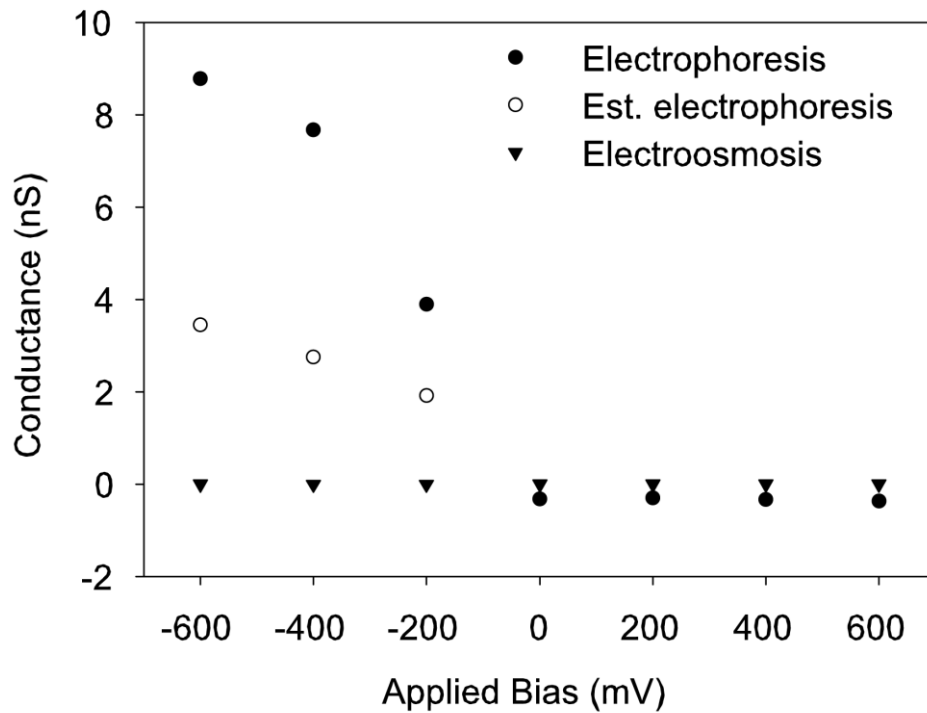
a.
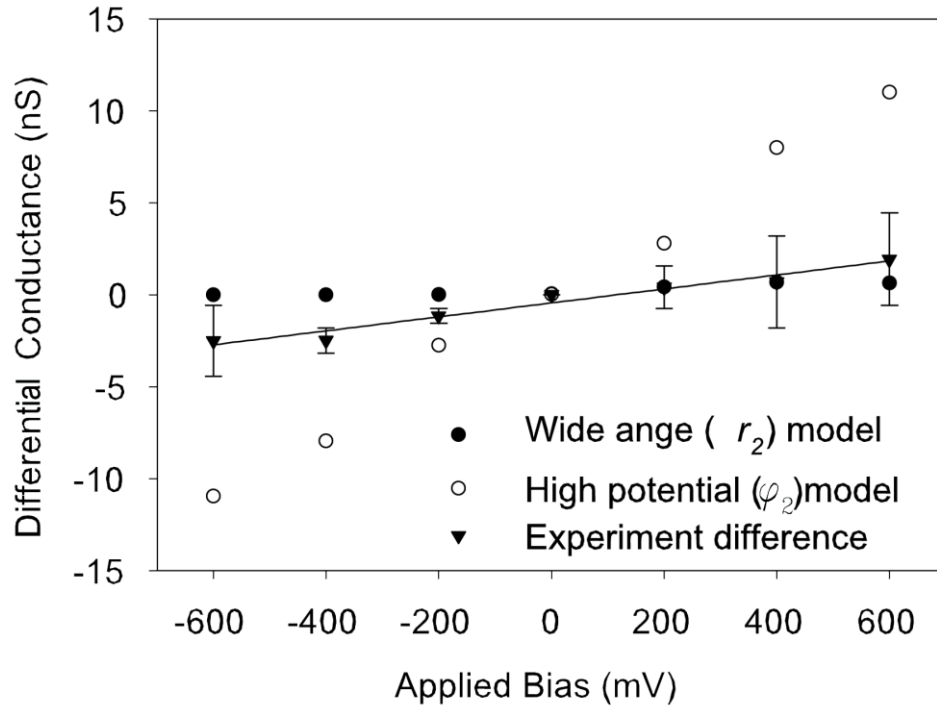
b.

Figure 4.4. a. The conductance is driven by electrophoresis under negative bias with negligible contribution from electroosmosis. Under positive bias, the electrophoretic conductance is very small, corresponding to the non-conducting state of the nanopore. At all considered biases, the electroosmotic conductance was at least 10^5 times smaller than the corresponding electrophoretic conductance. b. The slope of the differential conductance between KCl and NaCl solutions is dependent on the applied bias in the high potential (φ_2) model and it is independent of the applied bias in the wide angle model. Experimentally, the differential conductance showed very weak dependence on the applied bias which is consistent with a wide nanopore angle (small slope).

4.3.3 The effect of nanopore size on conductance

To further investigate the effect of nanopore size, we examined the conductance of a large pore (produced by FIB without the pore-narrowing electroplating step; diameter ~150 nm) and a small pore (after electroplating; diameter <10 nm) first under an unbiased condition and then under a highly negative (φ_1=-600 mV) biasing condition. Figure 4.5a shows the resulting conductance driven by the trans-pore potential (V_0) when no biasing is applied for the large and small pore devices along with the numerical result. The measured conductance exhibits a good linear relationship with the concentration of electrolyte (large pore: $G = 826c + 11.87$; small pore: $G = 8.0253c + 2.872$; numerical pore: $G = 1.8218c + 0.0176$, where c is concentration in units of molar and G is conductance in nanosiemens). The linear relationship between conductance (G) and concentration (c) was based on goodness of fit for the empirical data ($0.5746 < R^2 < 0.9998$). The goodness of fit of a linear relationship extended to the modeling results as well ($0.9946 < R^2 < 0.9957$). Since the numerical model was based on a scaled-down nanopore geometry (due to computational limitations), the resulting numerical conductance is smaller than the experimental results at all concentrations, as expected due to the proportional relationship between nanopore size and conductivity. Smaller nanopores typically result in lower ionic currents than larger nanopore (even in conditions of comparable ionic strength).[38,39] Because our numerical model is constrained to be several orders of magnitude smaller than the physical nanopore due to computational limitations (see Figure 4.6c for size estimates), it is reasonable to expect that the numerical conductance will also be several orders of magnitude smaller than our

experimental observations. However, because the conductance is a function of the nanopore geometry, applied bias, supporting electrolyte concentration, and distribution of charge within the nanopore there is no reason to expect a simple relationship between nanopore size and conductance. No measureable difference in conductance was observed between the three solutions investigated (KCl, KI, and NaCl) and pHs in any nanopore. Figure 4.5b shows the conductance for the large (150 nm diameter), small (<10 nm diameter), and numerical nanopores under the highly negative biased condition. Overall, the conductance of all cases is higher than those in Figure 4.5a, respectively. The conductance of the large pore showed some sensitivity to changes in pH (large pore, pH 4: $G = 253c + 11.484$, pH 10: $G = 283.79c + 7.88$, p $<$ $7.4 \cdot 10^{-6}$). No statistically significant difference was found between pH 4 and pH 7 or between pH 7 and pH 10 (data not shown). The conductance of the small pore appeared insensitive to changes in pH (small pore: $G = 29.096c + 11.234$). Previous studies have suggested that the conductance in nanopores at low concentrations is inversely proportional to pH due the influence of proton transport.[86] Our observed proportional relationship between conductance and pH in the large pore is contrary to this argument, indicating that the conductance at low concentration is more strongly influenced by the applied bias (φ_1) than by proton transport. We speculate that some other mechanism, such as pH regulated change to the work function of the nanopore and/or bias potential, may be responsible for the observed behavior. As with the unbiased conductance of the numerical nanopore, the biased concentration/conductance relationship was similarly well described by a linear relationship with reduced magnitude due to the small, scaled down volume of the

numerical pore (numerical pore: $G = 6.288c - 0.06462$). Figure 4.5c illustrates the effect of altering the trans-pore potential V_0 on the conductance through the large pore under various applied biases (φ_1). No gating effect was observed due to the relatively large, sub-micron diameter of this nanopore. Altering the trans-pore potential merely creates an offset in conductance.
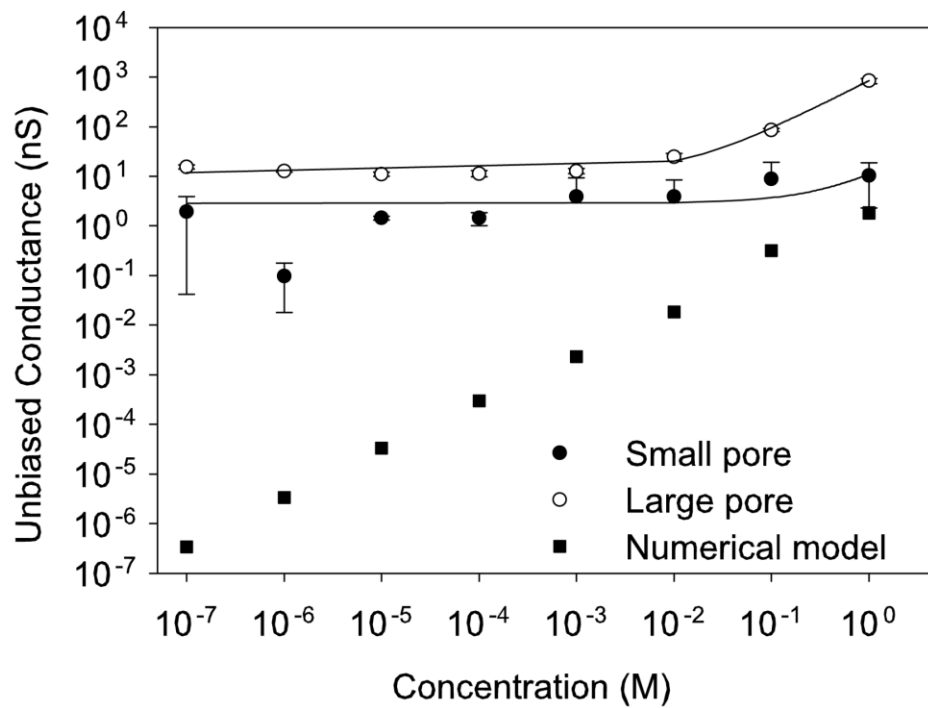
a.
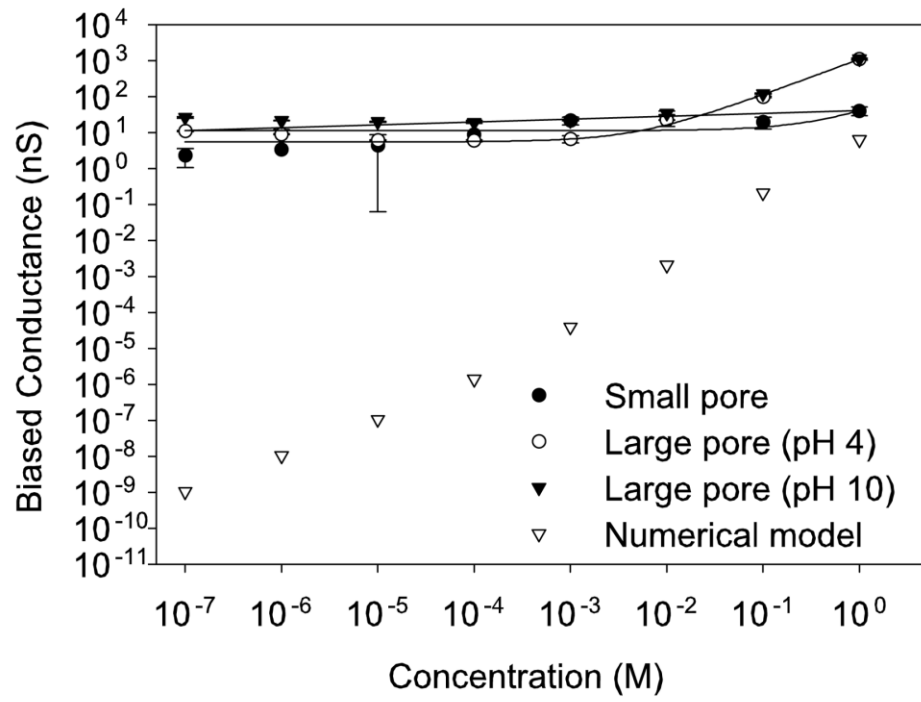
b.
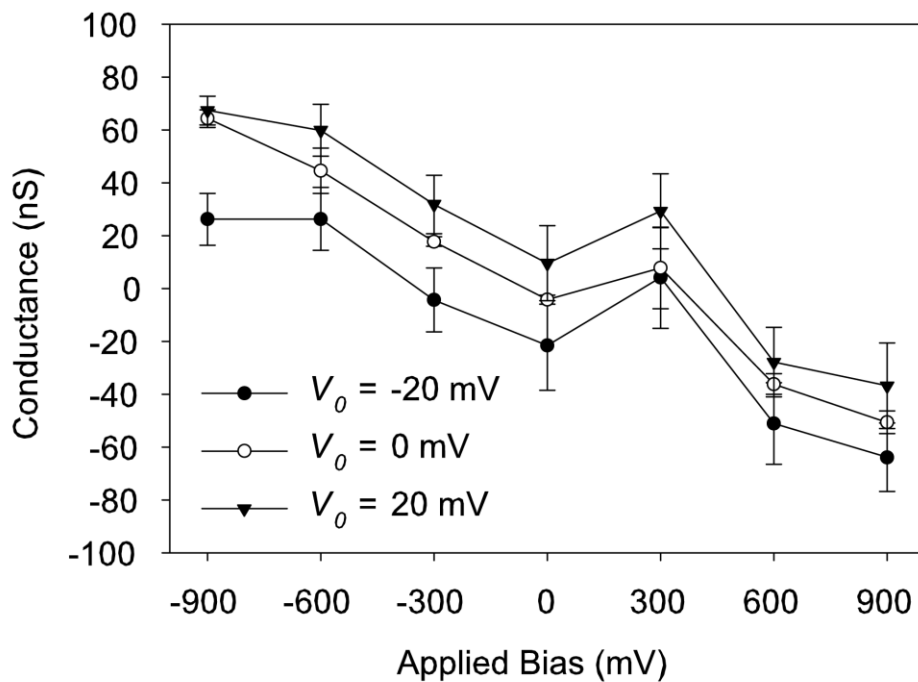
c.

Figure 4.5. a. Variation of conductance for a small and large nanopore and the numerical

model as a function of concentration when no bias (φ_1) is applied. b. Variation of

conductance as a function of concentration when the maximum negative bias is applied.

The solution with pH 10 had a higher conductance than the solution with pH 4 in the

large pore and all three pores show no dependence on the type of supporting electrolyte.

c. Variation of conductance with the applied bias under three different trans-pore

potentials for the large pore.

4.3.4 *The transient charging behavior*

When the applied bias was altered, a surge of ionic current developed and decayed into

a steady state, as shown in Figure 4.3b. Figure 4.6a shows representative transient ionic

conductance that develop due to applying the maximum bias from the ground state in both experiment and the numerical model $(\Delta\varphi_1 = \pm 600mV)$. The polarity of the transient current is dependent on the polarity of the change in bias, with increasing biases resulting in rising current and decreasing biases resulting in falling current. This relationship between the polarity of the change in bias and the direction of the transient current was consistent in all nanopores under all experimental conditions. Preliminary analysis of the transient currents indicated that the curves consist of complex exponential decay, indicative of a combined resistive and capacitive charging event. In order to determine the fundamental decay time constant, the complex conductance was obtained in the frequency domain and separated into storage and loss components (the real and imaginary parts of the Laplace transform, respectively) as discussed in ref. [87]. The fundamental decay time constant was the inverse of the fundamental frequency of the complex conductance loss spectrum. Transient ionic currents occur due to a reorganization of the ionic distribution within the biased region of the nanopore (Figure 4.6b). The number of charges within the nanopore was derived from the numerical model and consists of the net charge of the ions in the diffuse layer ($q = F_c V_{vol} \sum z_j c_j$) and experimentally derived by integrating the transient currents with respect to time. The fluid within the nanopore accumulates charge within the electrical double layer in response to the potential at the nanopore surface. The charge accumulated in the fluid can be separated into two distinct regions that correspond to the gold layer (the biased region) and Si_3N_4 layer (the unbiased region) of the nanopore. During a transient charging event, the number of charges in the nanopore region surrounded by the unbiased portion of the

nanopore does not significantly change (Figure 4.6b), which is consistent with the expectation that charges accumulate in the double layer to screen the surface potential. The number of charges in the biased portion (Figure 4.6b) is linearly proportional to φ_1 (numerical model: $q = -255.13\varphi_1 + 14.957$, experimental integration: $q = -8 \cdot 10^7 \varphi_1 - 7 \cdot 10^9$), indicating that changes in this region are responsible for the transient behavior and the steady-state asymmetric conductance response. The linear relationship between charge (q) and applied bias $\left(\varphi_1\right)$ was unexpected given the complex and often non-linear relationship between electrical double layer capacitance and surface potential. However, in both our numerical and experimental results, the relationship appears to be reasonably regarded as linear ($R^2 = 0.9588$ in experiment, $R^2 = 0.9921$ in the numerical model) for the pores we tested. The transient current may be expected to have an initial large magnitude as the number of charges quickly enter or exit the bias region before the current reaches steady state, with the polarity of the change in current dependent on whether the change in bias prompts an accumulation or reduction in stored charge.

The time constant is independent of the change in the magnitude of the applied bias. The time dependent form of the numerical model was solved for $\varphi_1 = \pm 200\,\text{mV}$ and $\varphi_1 = \pm 600\,\text{mV}$ transitions. The numerical transient currents display a time dependency similar to the experimentally observed transient currents, but on a smaller scale due to the smaller volume and number of species in the numerical model. Figure 4.6c shows the effect of scaling the biased volume on the magnitude of the time constant. The volume of

the nanopore was estimated based on known parameters and the steady-state conductance. The relationship between the biased volume of the nanopore (estimated with a 95% confidence interval) and measured time constant is best fit by a power relationship ($T_L = a\,\varphi_1{}^b$), where b is a value between 0.274 and 2.7215 with an average value of 0.4258. The time constant of the numerical model was calculated for the wide and small angled models which formed upper and lower bounds on the steady-state conductance (Figure 4.6c). The relationship between biased volume and time constant is best fit by a power relationship in the numerical model, similar to the experimental device. The range of exponents in the small and large angle models is 0.2391<b<3.0711, which contains the range of experimental exponent values.
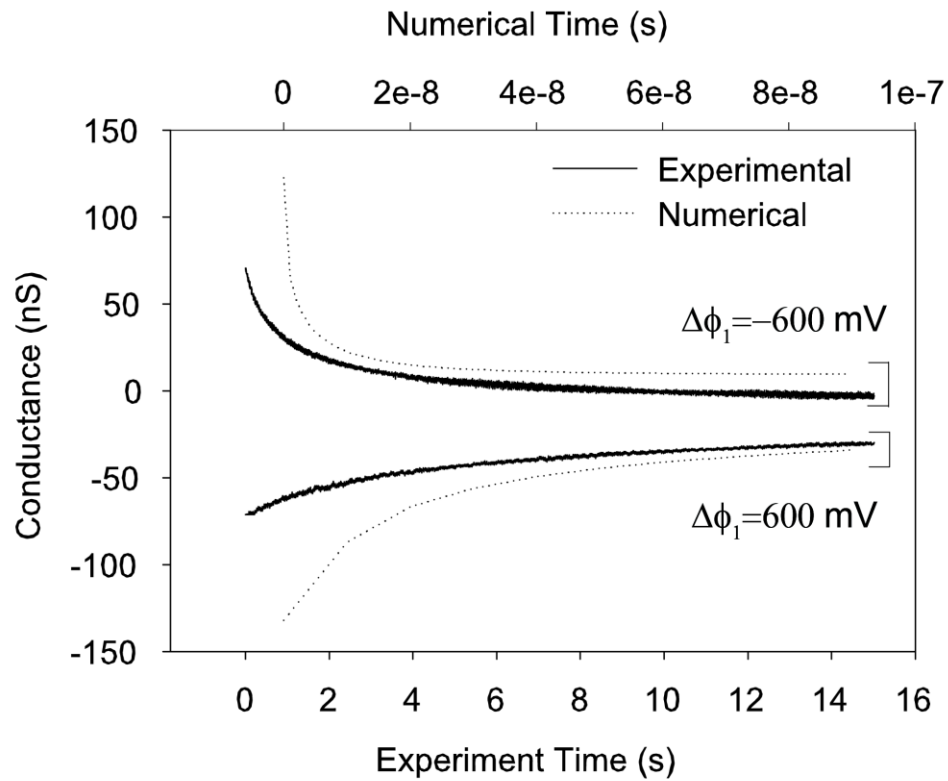
a.
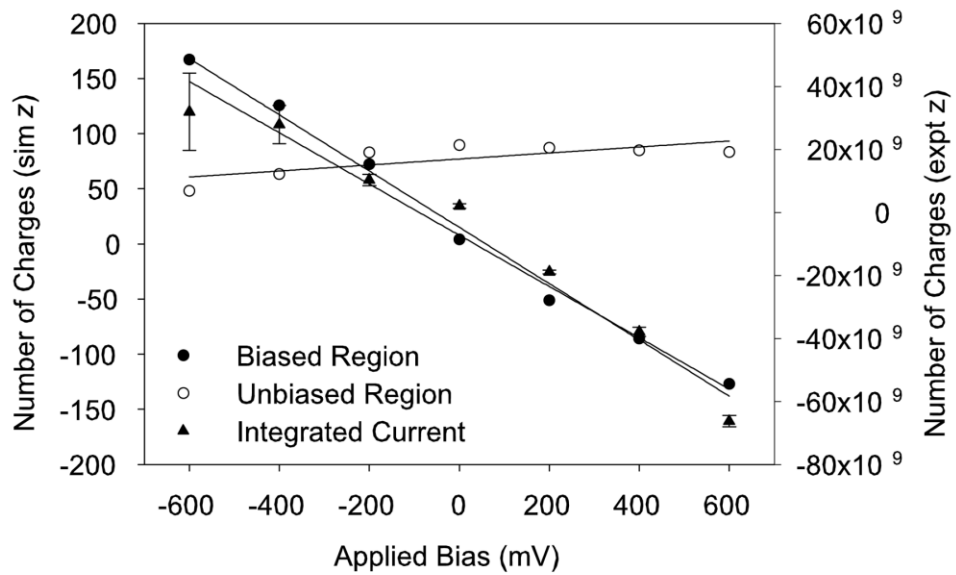
b.
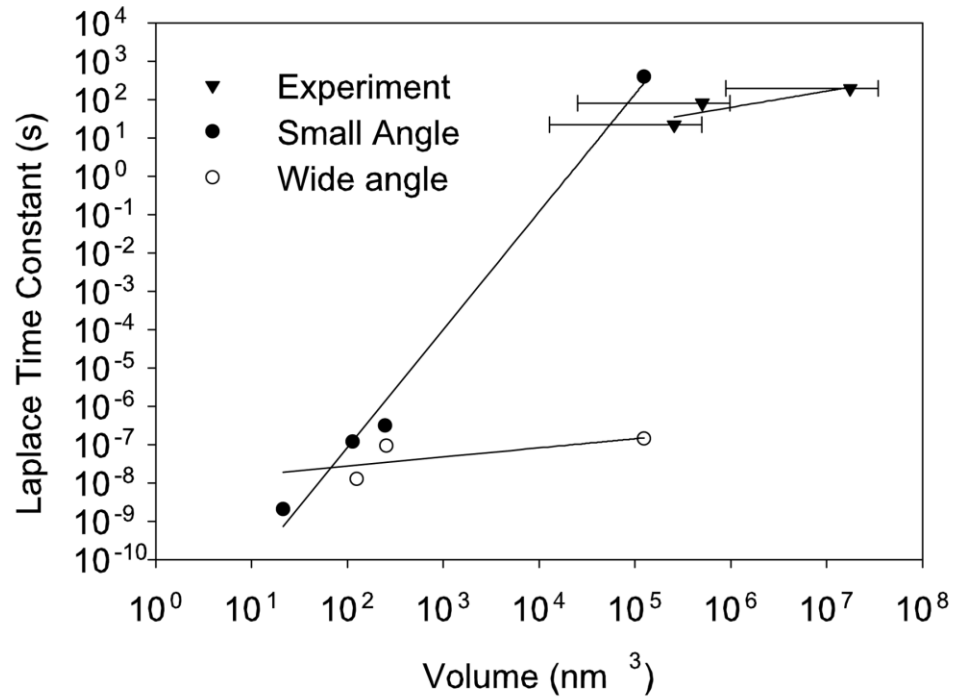
c.

Figure 4.6. a. Typical transient currents obtained from the nanopore and numerical model

for a potential transition (φ_1) from 0 mV to $\pm$ 600 mV. b. The charge stored in the two

regions of the nanopore changes in response to the applied bias. c. The time constant is

proportional to volume of the biased region of the nanopore. The observed experimental

relationship is captured between the results for the narrow and wide angle numerical

models.

4.4 Conclusion

A nanopore was fabricated in layers of Si_3N_4 and gold. Modulation and gating of the

ionic current was achieved by externally controlling the electrical potential of the gold

portion of the nanopore. The conductance through the nanopore was insensitive to the

type of supporting electrolyte and pH. The insensitivity of the nanopore to the species of the cation indicates that the conductance is primarily influenced by the conical geometry of the nanopore. For very small nanopores with unbiased steady state conductance < 20 nS in 100 mM KCl, a zero net flux state was induced by different ion polarities in the Si_3N_4 and gold-plated layers of the nanopore. Analysis of the transport mechanisms of the nanopore indicate that the current is driven by electrophoresis with negligible electroosmosis. Time dependent currents were observed when the bias (φ_1) was instantaneously altered. The characteristic decay time constant was proportional to the biased volume of the nanopore and insensitive to the magnitude of the change in bias. The transient currents were attributed to changes in the number of charges required to screen the bias (φ_1) applied to the nanopore wall.

The nanopore system described here demonstrates that the balance between the structure of the electrical double layer and surface potential may be exploited to produce novel effects. The charge stored in the electrical double layer is the chief mediator of both steady-state and time dependent nanopore behavior. Altering the charge density of the fluid within the nanopore produces variable conductivity while creating regions with incompatible ion selectivity enables gating of the ionic current. Real-time electrical control of conductance will enable fast optimization in systems where the device sensitivity and acquisition rate is dependent on nanopore conductance. Active control of conductance will allow uniform, parallel, multi-nanopore devices to be constructed, despite physical variations between nanopores on-chip. By allowing control of the device at the time of use, costly fabrication optimization steps may be eliminated. Modifiable

conductance and gating suggest that electrically modified nanopores may be useful in nanofluidic devices as logic gates and valves. The relationship between the electrical double layer and the electrostatic bias suggests that it may be possible to develop an operating modality sensitive to the structure of the electrical double layer.

CHAPTER 5 : DETECTING AND IDENTIFYING SMALL MOLECULES IN A NANOPORE FLUX CAPACITOR

5.1 Introduction

A new method of molecular detection in a metallic nanopore was developed and characterized with experimental and numerical methods. Measurements were made for the charging potential of the electrical double layer capacitance as charge-carrying small molecules translocated the nanopore. Signals for the charging potential were found to be correlated to the physical properties of analyte molecules. We were able to distinguish molecules with different valence charge or similar valence charge but different size. The relative magnitude of the signals from different analytes was consistent over a wide range of experimental conditions, suggesting that the detected signals are likely due to single molecules. Numerical modeling of the nanopore system indicated that the double layer potential signal may be described in terms of disruption of the electrical double layer (EDL) structure due to the size and charge of the analyte molecule, in agreement with Huckel and Debye's analysis of the electrical atmosphere of electrolyte solutions.

Nanopore devices for detecting and identifying small molecules and sub-molecular units have been developed with a range of mechanisms and applications. The most commonly cited use for nanopore sensors is in nucleic acid sequencing. [20,24,88–90] Because of the very small (nanoscale) sampling volume of this type of sensor, it is possible to temporally and spatially isolate individual molecular and sub-molecular analytes.

However, a reliable method of transducing the translocating analyte into signals relevant to the physical and chemical properties is needed.

The nanopores used for sensing may be biological in origin (for example, based on α-hemolysin proteins) or solid-state devices. Biological nanopores have so far fallen short of their expected performance. They are difficult to customize, and have limited possibilities for signal transduction.[90] Alternatively, solid-state nanopores are highly customizable and in many cases are compatible with standard thin-film fabrication techniques. Nanopores developed for molecular sensing applications typically rely on measurements of the ionic through-current as a signal transduction mechanism, where the signal arises due to occlusion of the nanopore by the analyte.[20,39,91] Transverse detection methods have been developed in order to overcome the high noise level of the ionic current signal, however, these methods typically result in an inherent sensitivity to the orientation of the analyte within the nanopore, which limit the usefulness of any derived signal.[23,4419,2621,25]

Thus far in the study of nanopores, the electrical double layer (EDL) has primarily been considered with regards to transport properties, rather than any sensing applications. In any sufficiently small nanopore, the analyte must move through the electrical double layer during translocation. In the small space within the nanopore, the electrical double layer occupies the entire volume, resulting in regions of charge selectivity which can cause enhanced ionic current and current gating effects.[10–12,14,32,38,59] It has been shown that many of the transport properties of nanopores may be explained in terms of the structure of the electrical double layer within the lumen.[32] Therefore, it is important to

understand the properties, structure, and effects of the electrical double layer in a nanopore.

The energetic properties of the electrical double layer have been largely neglected in nanopore sensing applications, even though the electrochemical potential of the electrical double layer within a nanopore is determined by the molecular contents of the solution. A general analytical approach to considering the electrochemical potential of a solution of charged molecules was considered by Huckel and Debye. This approach offers insight into the relevant parameters to consider in nanopore sensing. When an electrolyte is dissolved, the free energy of the solution is a function of the concentrations, valence charges, permittivities, and radii of the components of the electrolyte solution. The expression for the potential energy stored in an electrolyte solution can be expressed as a sum of the thermodynamic potential of the molecules in solution and the electrical atmosphere created by the presence of charged molecules: $(\phi = \phi_k + \phi_e)$, where ϕ is the total electrochemical potential of the solution, ϕ_k is the physical potential, and ϕ_e is the electrical atmosphere.[5] The total potential may be calculated as sum of the contributions of all types of molecule (j) in the solution from $j = 0$ to s, where $j = 0$ refers to the solvent. The physical potential (ϕ_k) is the sum of the number of molecules of type j with thermodynamic potential ϕ_j for all s types of molecules in the solution. Physical potential was described by Planck as:

$$\left(\phi_k = \sum_0^s N_j \left(\varphi_j - k_B \log(X_j) \right) \right)$$
Equation 5-1

111

(where N_j is the number of molecules of type j, φ_j is the thermodynamic potential of molecules of type j, k_B is the Boltzmann constant, and X_j is the mole fraction of j). The contribution of the electrical atmosphere as defined by Huckel and Debye includes consideration of the size, permittivity, number, and charge of the molecules in solution. The potential of the electrical atmosphere was found by summing the distributed electric field of each molecule in the solution and may be written:

$$\left(\phi_e = \sum_{0}^{s} N_j \frac{z_j^2 q^2}{\varepsilon T} \frac{x}{3} \chi_j \right)$$

Equation 5-2

where z_j is the valence charge of j, q is the elementary charge, ε is the permittivity of the solution, T is the temperature, and x is the inverse of the Debye length. The term χ_j is an expansion of a complicated integral and is a function of the Debye length ($\lambda_D = 1/x$) and the radius (r_j) of molecules of type j: $\left(\chi_j = 1 - \frac{3}{4} x r_j + \frac{3}{5} x r_j - ... \right)$. The physical potential (ϕ_k) accounts for the free energy and Brownian motion of uncharged molecules, while the electrical term (ϕ_e) considers the sum of the contributions of each molecule in solution to the electrical atmosphere of the solution. In this study, because we are interested in electrical interactions, our system will be determined by the electrical atmosphere term (ϕ_e). When an electrolyte solution is placed in contact with an electrode, a charge gradient described by the Gouy-Chapman-Stern model of the electrical double layer forms in response to the electrical potential of the surface. [70] The electrochemical potential stored in the electrical double layer must be balanced by the

potential of the electrode. In a system in which the electrode potential is not fixed, the energetic balance is determined by the electrochemical potential of the electrical double layer and the charge accumulated on the electrode. According to Planck, Huckel, and Debye, the energetic balance may be expected to be a function of the valence, size, concentration, and identity of the constituent species of the solution. By measuring the potential at the nanopore electrode, we may get a signal that represents the structure and properties of the constituent species in the solution. Because the analyte molecules must move through the EDL within a nanopore, we may detect alterations to the EDL structure due to the physical and electrical differences between the supporting electrolytes and analyte molecules. In such a nanopore system, analyte orientation has less effect on the measured signal than in other nanopores like the tunnelling or conductance types due to the symmetry of the measurement in a nanopore ring electrode. Additionally, the mechanism responsible for the ionic current signal is not precluded by the detection of the electrical double layer signal. This mechanism should provide complementary measurements of individual molecular analytes by allowing simultaneous collection of both ionic current and double layer potential signals. By exploiting the changes that occur in the electrical double layer structure when an analyte translocates a nanopore, we demonstrate a new double layer detection method sensitive to transient alterations to the electrochemical potential within the nanopore.

5.2 <u>Methods</u>

5.2.1 Experimental Methods

The fabrication and arrangement of the nanopore system is similar to what has been described in our previous work.[4] Briefly, a nanopore was formed in a thin membrane by electron beam (e-beam) lithography and inductively coupled plasma etch. The thin membrane was composed of a support layer of LPCVD Si_3N_4 (50 nm) and an electrode layer of gold (15 nm), bonded by a thin titanium adhesion layer (Figure 5.1a). The e-beam lithography patterned nanopore was defined to have a diameter of 10 nm and a range of e-beam doses were applied. Nanopores formed in this way were evaluated in 100 mM NaF solution and those with a conductivity of <2 nS were selected for further experimental evaluation, where conductance <20 nS typically corresponds to a minimum diameter of <10 nm in solid-state nanopores.[39] A diameter range of 1-10 nm was estimated by noting that rectification and electrical double layer overlap effects (such as conductance gating) are typically only observed in nanopores smaller than 10 nm and that the size of the analytes considered approach a maximum diameter of 0.8 nm.[4]

The prepared nanopore chip was placed in a fluidics cell containing an analyte solution consisting of an aqueous mixture of the analyte molecule (citric acid, hydroquinone, oxalic acid, or ascorbic acid in this study) at a low concentration (10^{-8} M) and a supporting electrolyte (NaF) in a range of concentrations from 10^{-7} to 1 M with logarithmic increments (Figure 5.1a). Because NaF dissociates into Na^+ and F^-, and F^- will form HF in solution (due to HF being a weak acid), it was important to ensure that the concentration of HF was negligible compared to the concentration of the molecular analytes and supporting electrolytes. Within the nanopore, the solution was determined to

have a pH of 12. The concentration of HF at this pH is expected to be at least an order of magnitude smaller than the concentration of the analyte molecules, and we treat this as negligible. The specific analytes used in this study were chosen to have distinct acid dissociation constants (pKas) and to be relatively similar in size (Table 3). In order to explore the effect of pH, citric acid was evaluated at pH 2.8, 3.9, 5.5, and 8.5 (values chosen to fall on distinct valence charge levels relative to the pKa) with and without NaCl as a supporting electrolyte. NaCl was chosen as the supporting electrolyte in this pH experiment in order to maintain a homogeneous ion population with the titration reagents, NaOH and HCl. It was desirable to avoid using HF as a titration reagent, due to the risk of damaging the nanopore device and because HF is a weak acid. In low pH conditions, the concentration of undissociated HF would increase to non-negligible levels. Since HCl and NaOH are a strong acid and base, respectively, there was no risk of producing undissociated molecules at low or high pHs. In order to investigate any dependency of the signal on the analyte concentration, the molecular analytes were evaluated in concentrations from 10^{-8} to 10^{-2} M in 10^{-5} M NaF solution.

In all cases, a constant trans-pore potential (10 mV) was applied across the nanopore between the two reservoirs of the fluidics cell. The gold layer of the nanopore was charged by a constant electrical current (37.4 ± 3.2 pA). The ionic current through the nanopore and the electrical potential measured at the gold layer were digitized and recorded. The trans-pore potential and ionic current were produced and acquired by a patch clamp amplifier (Molecular Devices, Axopatch 200B, CA) and two silver/silver chloride (Ag/AgCl) electrodes. The signal traces were recorded at 80 kHz using custom

software (Mathworks, Matlab 2012a, MA). The constant charging current was produced with an external potentiostat (Princeton Applied Research, Versastat MC, TN). All experiments were conducted at room temperature with system components operating relative to a common electrical ground.
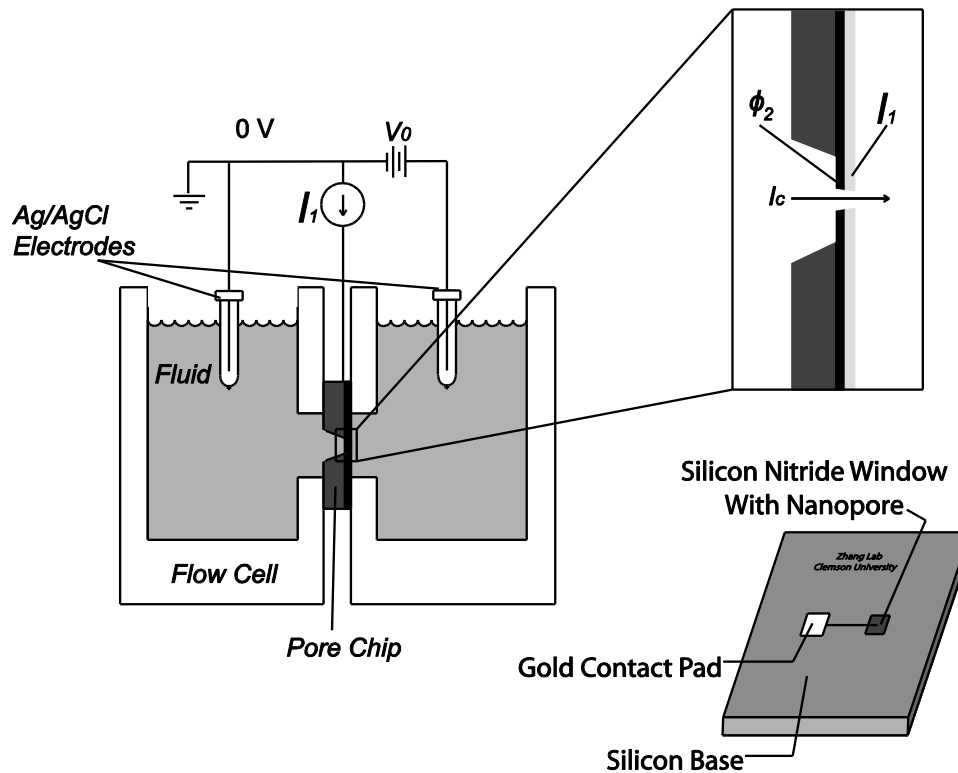
a.
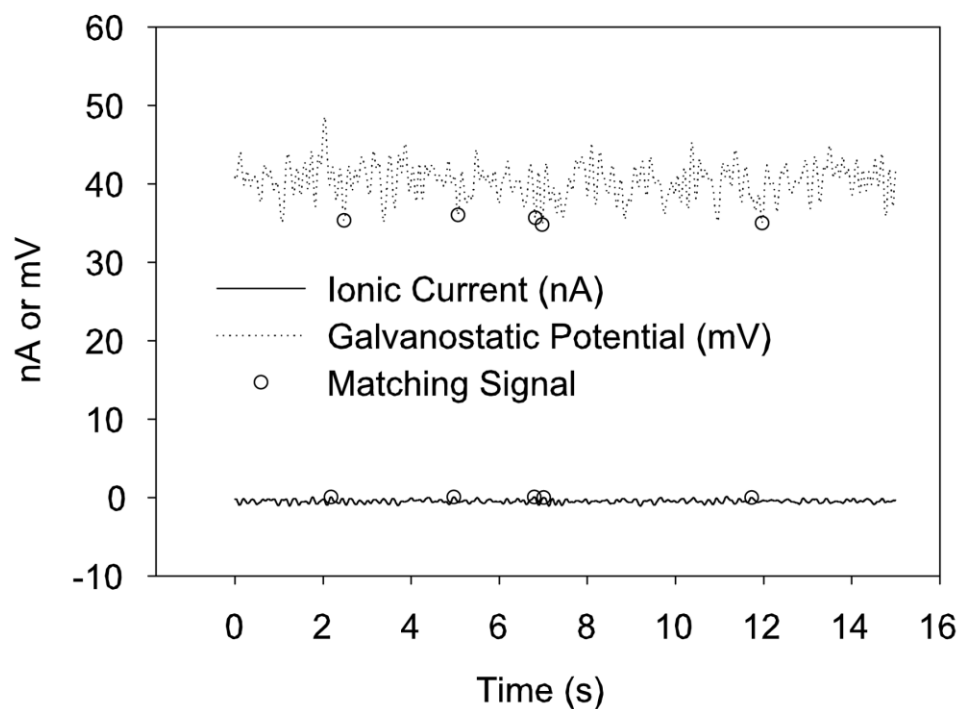
b.

Figure 5.1. a. The nanopore system includes a Si_3N_4/gold nanopore (Si_3N_4 is grey, gold is light grey) and a supporting solution. The solution contains the analyte of interest which is transported through the nanopore. An electric field is generated across the nanopore by application of a voltage clamp, allowing the ionic current through the nanopore to be monitored. A constant electrical current is supplied to the gold layer of the nanopore. b. The signals collected were differential measurements occurring in tandem, measured from the local baseline of the ionic current and double layer potential traces.

To quantify simultaneous transient signals in the ionic current and double layer potential traces, a custom data sorting algorithm was developed (Figure 5.1b). A sliding window was implemented with a width 5 s. Signal magnitude was calculated as the

difference between the central point and mean level within the sliding window. In order for a point to be recorded as a transient signal, the point must occur simultaneously in both the ionic current and double layer potential traces, be at least twice the standard deviation of the baseline, and a local extrema. In this way, random noise is screened and translocation events are confirmed by both the established ionic current signal and the novel double layer sensing mechanisms. The algorithm was implemented in a custom software package (Mathworks, Matlab 2012a, MA) and all data analysis occurred in post-processing.

Table 3. Molecular analytes and supporting ion characteristics

	Citric Acid	L-Ascorbic acid	Oxalic acid	Hydro-quinone	K+	Na+	Cl-	F-
pKa 1	3.14	4.1	1.23	10.35				
pKa 2	4.75	11.7						
pKa 3	6.39							
Expected Valence Charge	-3	-2	-1	-1	1	1	-1	-1
molar mass (g/mole)	210.14	176.12	90.03	110.11	39.10	22.99	35.45	19.00
density (g/cm^3)	1.67	1.65	1.90	1.30	0.86	0.97	1.56	1.51
estimated spherical radius (nm)	0.37	0.35	0.27	0.32	0.26	0.21	0.21	0.17
Polarizability (Bohr^3)	69.87	83.33	55.22	61.42	32.75	7.64	1.25	0.26
permittivity	1.78	2.23	3.31	2.11	2.10	1.41	1.06	1.02

5.2.2 Numerical methods

To have a better understanding of the underlying physics, a numerical model of the nanopore system was developed by extending previous modeling work in a finite element multiphysics modeling package (Comsol 4.4).[32] The model was constructed in 2-dimensions with axisymmetry, to take advantage of the rotational symmetry of the

nanopore (Figure 5.2a and b). Fully coupled Nernst-Planck, Stokes, and Poisson equations were solved over the appropriate model domains, as discussed in our previous work (model parameters are listed in Table 5). The electrolyte solution consisted of aqueous NaF. The surface potential (φ_2) of the Si_3N_4 layer of the nanopore was defined in a manner consistent with previous studies and the work function potential of Si_3N_4. In order to simulate the double layer charging of the electrical double layer capacitance at the gold layer, the surface of the gold layer was defined in terms of the potential across a capacitor in an equivalent circuit.[32,62,72] The overall charging behavior observed in the experimental system was modelled as an equivalent circuit in the numerical model (Figure 5.2a). The equivalent circuit was necessary to account for the system impedance and the steady-state charging behavior of the nanopore. The capacitor voltage (V_{DL}) was considered in the numerical model with a potential defined by the capacitor charge and the double layer capacitance:

$$\left(C_{EDL} = \mathcal{E}_0 \left(\frac{\delta^2 V}{\delta r \delta V_{DL}} \right) \right)^{62,72,92}$$

Equation 5-3

The double layer capacitance was coupled to the governing equations in the model and self-consistently and iteratively solved. The permittivity of the supporting ions was calculated by solving the Clausius-Mossotti relation for permittivity using polarizability (α') values (Table 3). Polarizability was obtained from density functional theory calculations performed with Gaussian quantum mechanical modeling software (Gaussian, Gaussian 09, CT). The permittivity of the supporting cation defined the permittivity of

the compact layer at the nanopore surface. The time domain response of the double layer potential is described by the expression:

$$V_{DL}(t) = I\left(\frac{e^{-\frac{t}{R_2 C_{EDL}}}}{C_{EDL}} + R_1(\delta(t) - 1)\right)$$

Equation 5-4

where the terms correspond to the electrical elements in the equivalent circuit shown in Figure 5.2a and $\delta(t)$ is the Dirac-delta function. Experimentally, the potential across the constant current source ($V_I(t)$) is recorded for processing. The difference between these terms (V_I and V_{DL}) is the potential across the resistor R_1 ($V_1 = IR_1$), which disappears in the difference measurement of the double layer signal. The time dependent potential measured at the current source is:

$$V_I(t) = I\left(\frac{e^{-\frac{t}{R_2 C_{EDL}}}}{C_{EDL}} + R_1\delta(t)\right)$$

Equation 5-5

a.

Right Reservoir
Conical Nanopore
Insulating Material
Left Reservoir
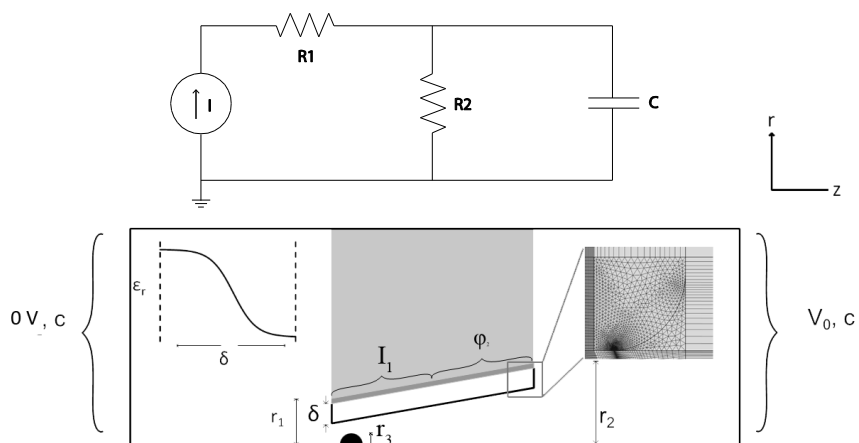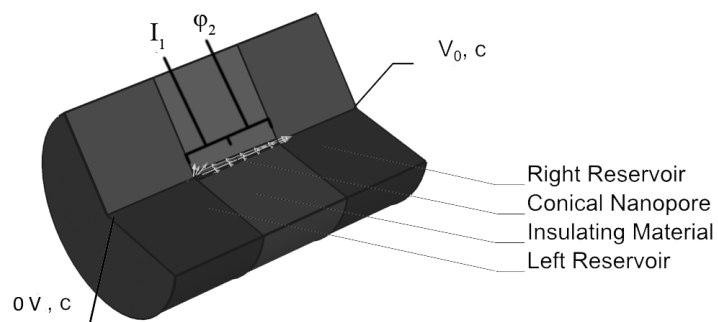
b.

Figure 5.2. a. The system was modelled as a conical nanopore in an axisymmetric

coordinate system. A compact layer was explicitly defined as region of adsorbed ions and

solvent at the wall of the nanopore. The electrical permittivity within the compact layer

121

smoothly varied from the permittivity of the electrolyte cation to the solution permittivity (left inset). The corners of the compact layer were rounded at the nanopore openings to reduce computational load (right inset). A circuit model is shown for the charging of the double layer. R_1 is the input resistance and R_2 is the leakage resistance. C is the double layer capacitance at the nanopore/solution interface. A charged spherical particle was evaluated within the nanopore lumen at charges levels of $z_j = -1$, -2, and -3 and radii of 0.2, 0.3, and 0.4 nm. b. A 3D view of the rotated conical geometry of the numerical model.

5.3 Results

5.3.1 *The EDL signal in various concentrations of supporting electrolyte*

The measured double layer potential signals for the analytes are shown in Figure 5.3a. It shows that the magnitude of the double layer signals for citric acid (CA) and ascorbic acid have logarithmic relationships with supporting electrolyte concentration (CA: $R^2 = 0.9084$, AA: $R^2 = 0.9033$). The logarithmic relationship was a poor fit for the double layer signals for oxalic acid (OA) and hydroquinone (HQ), which appeared to be constant for all supporting electrolyte concentrations considered. All comparisons between different analytes were significant within any given concentration ($p < 10^{-5}$), including the lowest quality (lowest signal to noise ratio, SNR) measurements at the 1M condition. The discrimination of the signal between molecular analytes decreases at high supporting electrolyte concentrations with a decrease in SNR near 1 M in NaF (Figure 5.3b). However, the relative signal magnitude for the analytes is consistent at all

122

concentrations of NaF. Overall, hydroquinone was observed to produce the most positive signal magnitude, with oxalic acid, ascorbic acid, and citric acid producing more negative signals in that order. At high concentrations, the quality (SNR) of the signal decreases. Saturation of the solution at high concentrations was observed as saturation of the steady state double layer potential in both numerical and experimental nanopores and as saturation of the charge density within the biased region of the nanopore in the numerical model (Figure 5.3c).
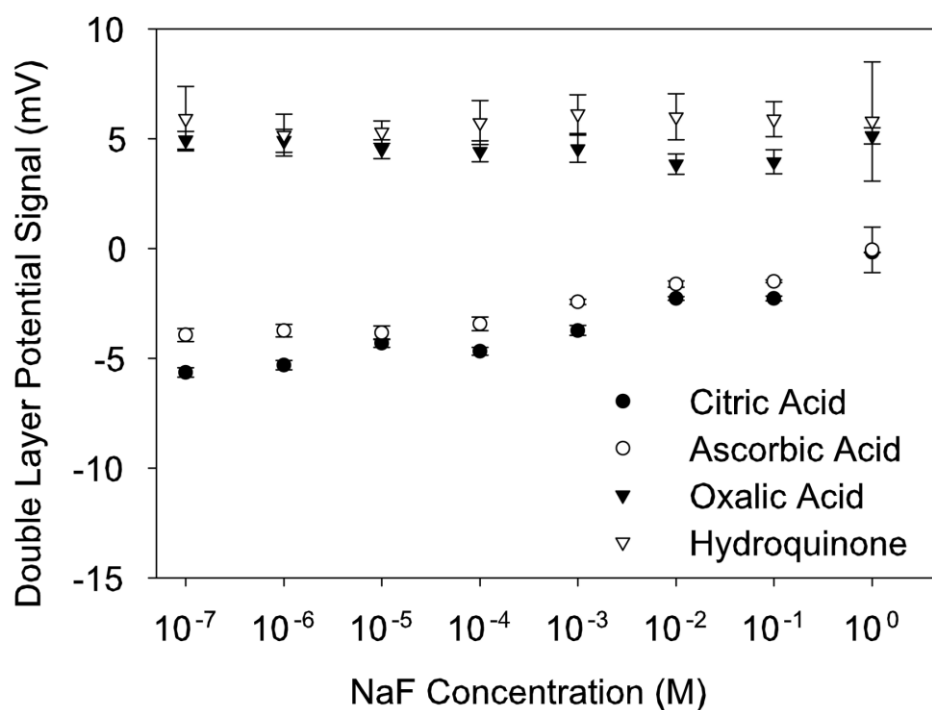
a.
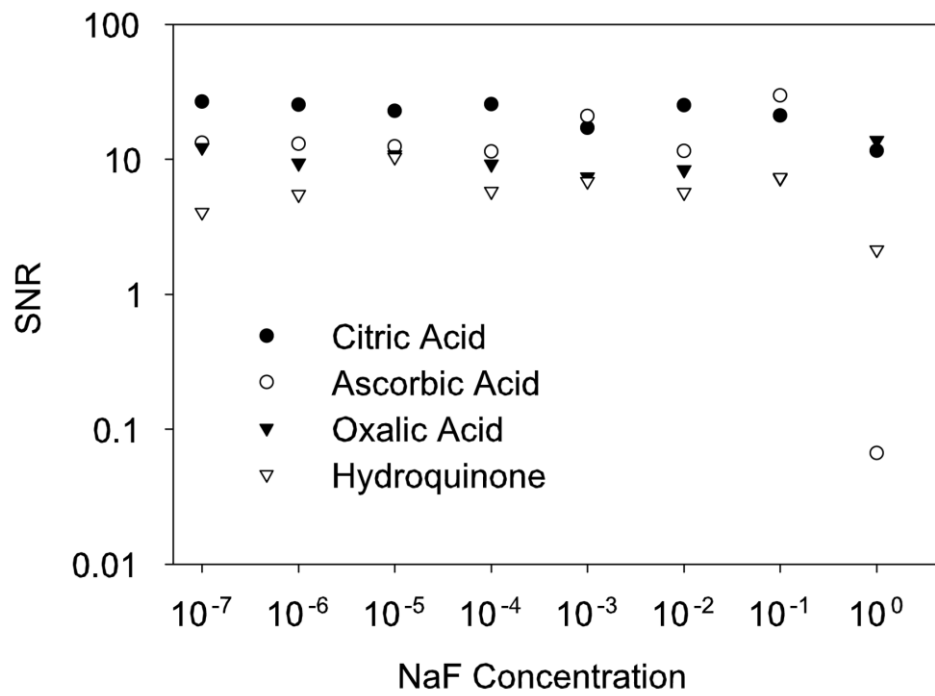
b.
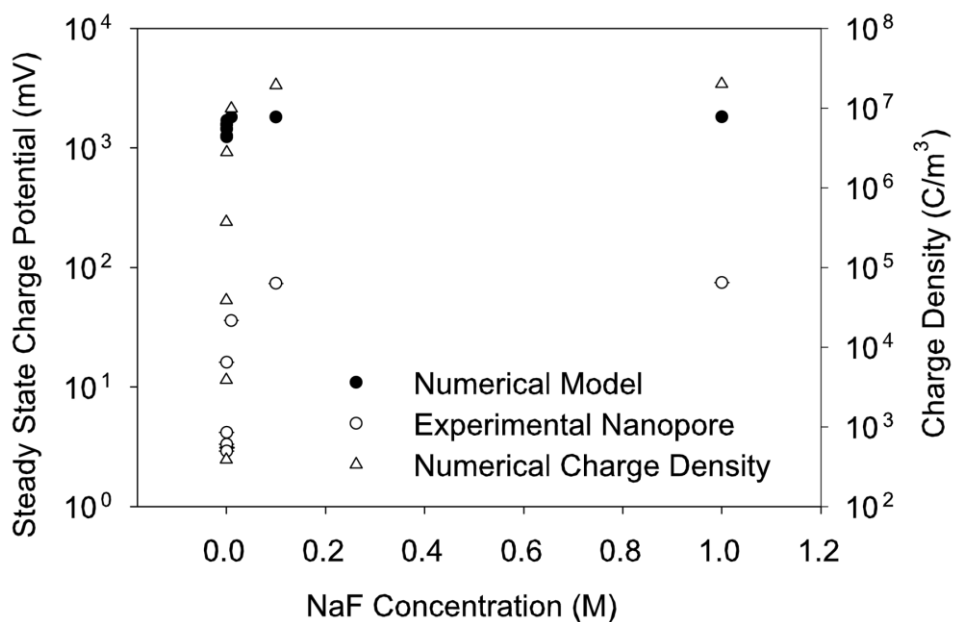
c.

Figure 5.3. a. The double layer potential signal is logarithmically related to the concentration of supporting electrolyte in NaF. In NaF, sensitivity decreases at high concentrations. b. The signal to noise ratio (SNR) varies by supporting electrolyte concentration and analyte species in NaF. The SNR drops off precipitously at 1 M NaF (corresponding to saturation of the NaF solution). c. The loss of signal sensitivity at high concentrations is correlated to the saturation of the steady-state potential in both experimental and modeling systems. Saturation of the charge density within the biased region of the nanopore was observed in the numerical model, corresponding to the loss of signal quality at high concentrations of supporting electrolyte.

5.3.2 *The effect of pH on the EDL signal*

The double layer potential signal appears to be insensitive to change in pH of the solution while the ionic current signal tends to increase with decreasing pH, especially in the 1M NaCl case (Figure 5.4a and b). Linear regression indicates that the double layer potential signal is not dependent on pH ($p > 0.2$) for citric acid in solution with pH of 2.8, 3.9, 5.5, or 8.5. The pH values were chosen in order to produce different levels of charge on the citric acid analyte based on the analyte's dissociation constants. Figure 5.4b shows that the ionic current signal is affected by the electrolyte concentration and pH, where the signal has an inverse relationship to pH at high concentrations (the signal decreases for higher pH values, $p < 0.05$ for the 1M case). The ionic current is weakly related to pH at low concentrations ($p > 0.05$ for the 0M case).
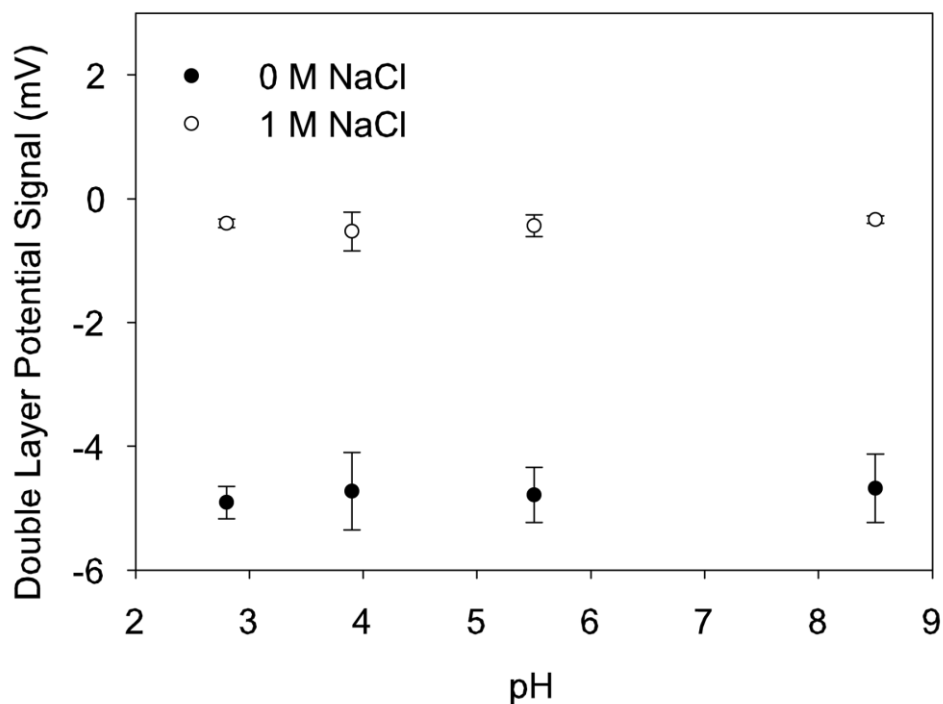
a.
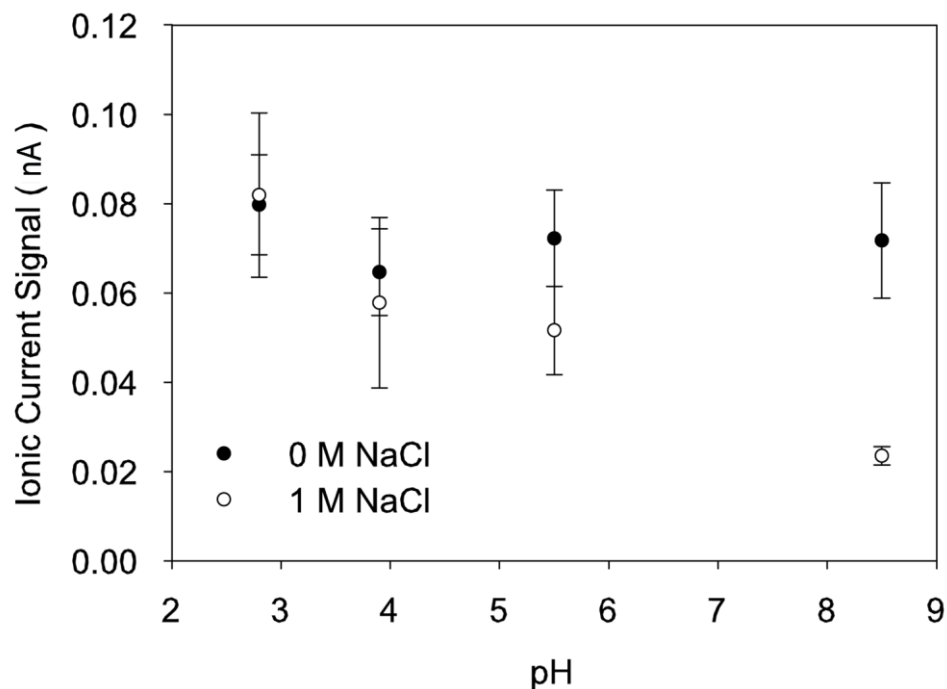
b.

Figure 5.4. a. The double layer potential signal of citric acid is insensitive to pH at both high and low supporting electrolyte concentrations. b. The ionic current signal is sensitive to the pH of the solution, increasing in magnitude at low pH.

5.3.3 *The effect of analyte concentration on the EDL signal*

The double layer potential signals exhibited weak dependence on the concentration of the analyte (Figure 5.5a). The double layer potential signals associated with the different analytes exhibited the same relative magnitudes presented in Figure 5.3a with similar SNRs (Figure 5.5b). The difference between the highest and lowest double layer potential signals (the signals from citric acid and hydroquinone, respectively) decreased at analyte concentrations $> 10^{-5}$ M (from ~15 mV at analyte concentrations $<= 10^{-5}$ M to ~10 mV at

analyte concentrations > 10^{-5} M). The decrease in signal range indicates a transition in the electrolyte solution consistent with our modeling results of multiple analyte particles within the nanopore (Figure 5.5c). Considering 2 or 3 additional analyte particles near the sensing region of the nanopore of the numerical nanopore model reduced the range of the double layer signal, which is consistent with our experimental results.
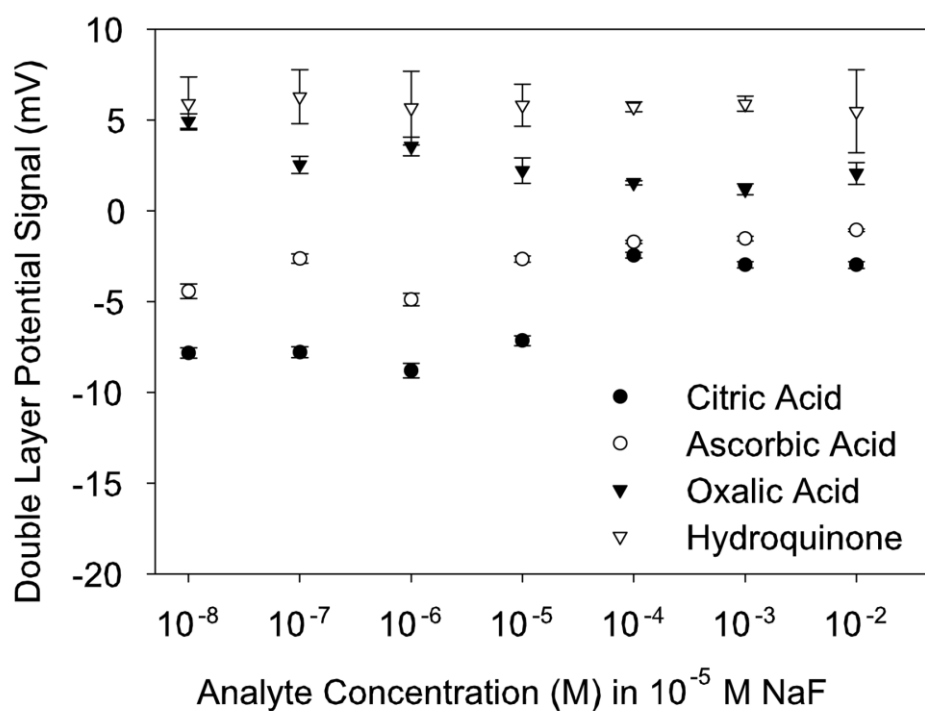
a.
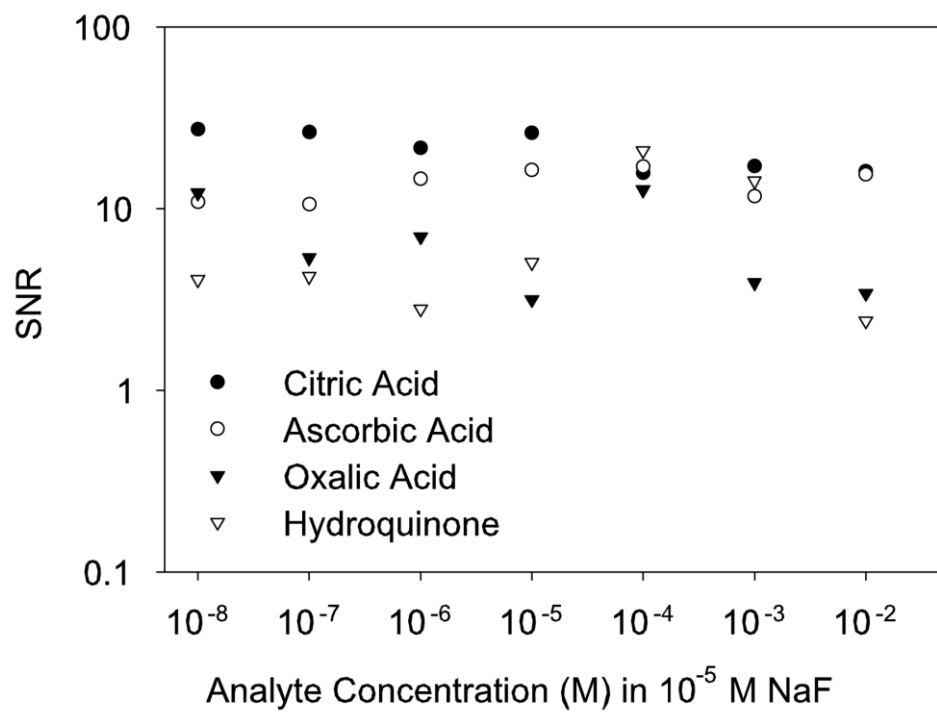
b.
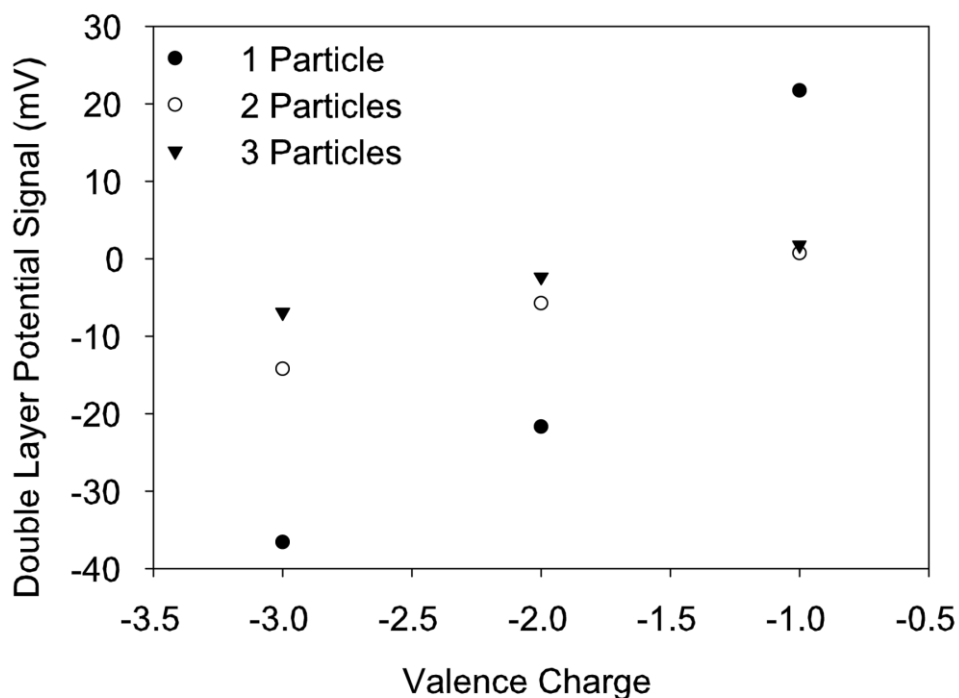
c.

Figure 5.5. a. The rank ordering of the signals from the molecular analytes in 10^{-5} M NaF was consistent for a wide range of analyte concentrations. The signal range is decreased at concentrations greater than 10^{-5} M, corresponding to the transition in dominant electrolyte from NaF to the molecular analyte. The decrease in signal range may be explained by an increase in probability that additional molecular analytes may be present near the nanopore. b. The signal to noise ratio of the double layer potential signal at all analyte concentrations was comparable to the original measurements in varying concentrations of supporting electrolyte. c. Our numerical results indicate that the presence of additional molecules within the unbiased lumen of the nanopore reduce the range of the double layer signal.

5.3.4 *The effect of analyte size and charge in the numerical model*

Figure 5.6a shows the double layer potential response in the numerical model for particles with charges of z_j = -1, -2, and -3 in NaF, which shows a similar trend as that observed experimentally for analytes with different valence charges. More negatively charged analyte particles produce more negative double layer potential signals. Figure 5.6b shows the change in the double layer potential caused by uncharged analyte particles of various sizes in NaF. At all concentrations, the effect of the size of the analyte particle only minimally contributes to the difference between signals. However, the presence of an analyte particle will produce a signal with diminished magnitude at high concentrations. Changing the permittivity of the analyte particle had no effect on the double layer potential signal (data not shown). However, considering the permittivity of the electrolyte ions at the surface of the nanopore (within the compact layer) was a critical factor in producing agreement between experimental and numerical signals.
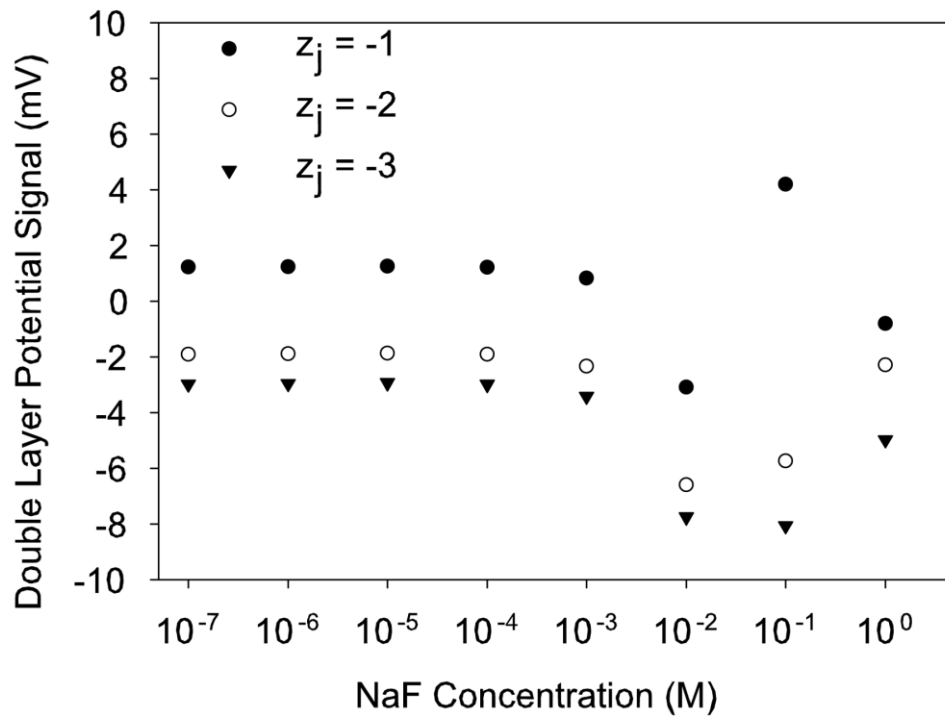
a.
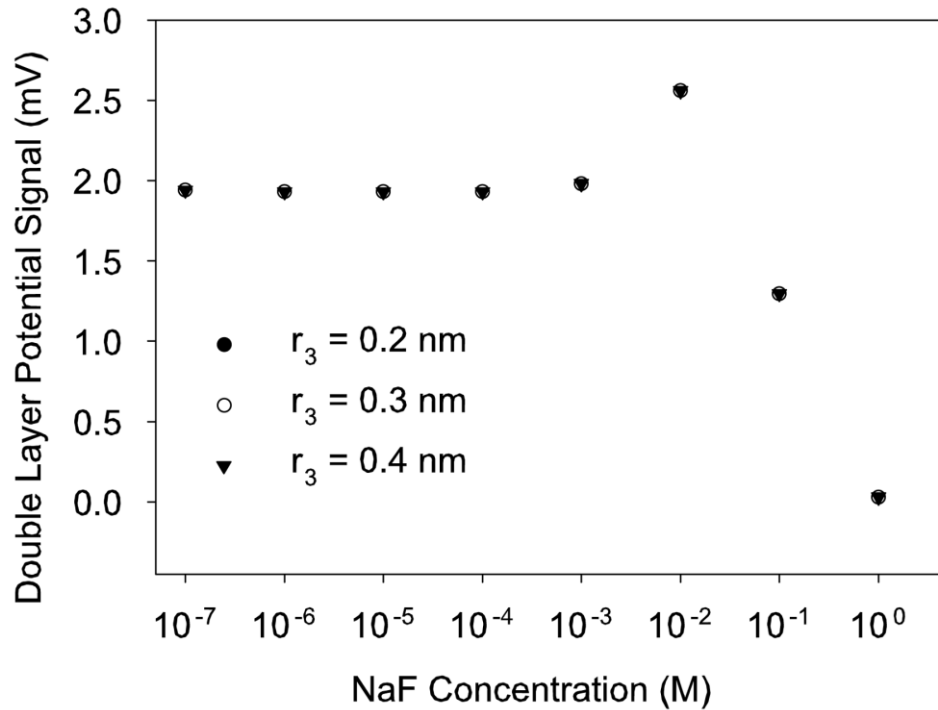
b.

Figure 5.6. a. The modelled double layer potential signal for analyte particle of radius 0.3 nm in NaF indicates that the sensitivity to particle charge is consistent with the experimental observations. Sensitivity is lost at high concentrations in NaF, similar to what was observed experimentally. b. The modelled double layer potential is perturbed by the presence of an analyte particle with finite size. Size of the particle had little influence on the double layer potential in the model at low concentrations and did not contribute much to the identification of analytes.

5.4 Discussion

5.4.1 Consideration of analyte effect on the EDL signal

The double layer potential signal at a given concentration of supporting electrolyte is primarily proportional to the expected charge of the analyte, however the difference between the signals generated by oxalic acid and hydroquinone (both are expected to carry the same valence charge) indicate that other physical parameters also have measureable influence. Perturbations of the electrical double layer by an analyte molecule produce the double layer potential signal. We examined the effect of the size, permittivity, and charge of an analyte molecule on the electrochemical properties of the solution within the nanopore, keeping with Debye's analytical result for the electrical potential of a solution. The effect of changing the size of the molecule in the numerical model is small, indicating that the difference in signal between analytes is only weakly influenced by the size of the analyte molecule in the range considered. The size effect in the model is much smaller than observed experimentally between oxalic acid and hydroquinone, indicating a possible limitation of the model. The change in signal due to the charge of the analyte molecule is more important to identifying the analytes than the effect of molecule size. The analytical characterization of the electrical potential of an electrolyte solution can be related to the effect of molecule size and charge; where changing the size of the analyte molecule alters the electrical atmosphere of the solution (ϕ_e) through the displacement effect described by Huckel and Debye, while changing the charge of the analyte molecule affects the electrical atmosphere through both the addition of the analyte valence charge and the compensatory charge accumulation within the solution.

5.4.2 The chemical conditions of the EDL in a nanopore

We consider the physical source of the double layer potential signal in terms of charge balance between the nanopore electrode and the solution within the nanopore. The charge density and structure of the EDL is related to the valence charge and size of the molecular analyte per our experimental observation and numerical modelling. Since the valence charges of the analytes are dependent on the local pH, we may expect the double layer potential to be dependent on the intraluminal pH. We explored the interactions governing this signal by varying the pH of the supporting electrolyte solution. Our experimental observations indicate that the double layer signal is insensitive to the solution pH while the ionic current signal is negatively correlated to pH at high supporting electrolyte concentrations. The concentration dependence in the pH effect in the ionic current signal is likely related to buffering of the solution at high concentrations. The amount of titration reagent needed to change the pH in the high concentration case is larger than in the low concentration case, amplifying the pH effect. When the pH is lowered, the number of hydrogen ions H^+ is increased and the ionic current signal tends to increase. This correlation implies that the ratio of charge carriers ($H^+:Na^+$) in the nanopore increases at low pH while the total number of charge carriers is governed by the electrical balance between the surface and solution. The ionic current signal increases due to a relative increase in diffusion coefficient because of the increased proportion of H^+ ions in the nanopore volume ($D_H^+ > D_{Na}^+$, Table 5). Since the density of charge carriers ($\sum z_j n_j$) is a function of supporting electrolyte concentration and analyte molecule in a charged nanopore, the double layer potential signal does not change as a function of pH.

We speculate that the double layer signal is mediated by the balance of charge density in the EDL and the potential at the electrode. In order to characterize this energetic balance, we estimate the pH of the intraluminal environment by considering the variable valence charges of the analytes. Table 4 lists the expected charge on each analyte at different pHs based on the pKas of the individual analytes. The ordering of the double layer signal magnitudes implies that the observed signal is consistent with an intraluminal pH of more than 12, at which point the analytes can be expected to carry a maximal negative charge.

Table 4. The valence charge of the molecular analytes at different pHs.

pH	1	2, 3	4	5, 6	7, 8, 9, 10	11	12
Citric Acid	0	0	-1	-2	-3	-3	-3
L-Ascorbic acid	0	0	0	-1	-1	-1	-2
Oxalic acid	0	-1	-1	-1	-1	-1	-1
Hydroquinone	0	0	0	0	0	-1	-1

5.4.3 *Evidence of a single molecule source*

We believe that the experimentally measured double layer potential signal is the result of single molecule translocation events. Our observation of the fixed order of the signals from different analytes for a range of analyte concentrations indicates that the analytes translocate in fixed proportions. That is, if the signal is due to a single molecule, it is always a single molecule that translocates, and if it is groups of more than one molecule,

the number of molecules in that group is consistent across analytes for a given concentration. Our modeling results indicate that additional molecules in the non-sensing (unbiased) region of the nanopore will result in a smaller signal range while additional molecules in the sensing region will result in a wider signal range (where signal range means the difference between the signals of citric acid and hydroquinone or the difference between valence charge -3 and -1 molecules in this study). Experimentally we can see that the signal range appears to decrease for analyte concentrations greater than the supporting electrolyte concentration, 10^{-5} M (Figure 5.5a). Because there is good agreement between our modeling and experiment signals in terms of signal range and magnitude, we relate these effects by considering the increased probability of multiple analyte molecules near the nanopore at high analyte concentrations. It is likely that additional analyte molecules are near the nanopore at high analyte concentrations, while the fixed ordering of the signals indicates that the presence of these molecules do not strongly alter the signal. These results suggest that the signal arises due a single analyte molecule translocating per detected event.

5.4.4 *Effects of saturation of the solution*

We believe that the decrease in SNR at high supporting electrolyte concentrations occurs due to saturation of the solution within the nanopore (saturation of NaF is near 1 M in standard conditions, 0.96 M at 21° C; saturated solution was reached at approximately 1M in this study). The SNR is consistent for electrolyte concentrations <1M, and the sudden decrease in SNR at 1 M NaF is indicative of a saturation effect,

since saturation of the solution would preclude significant changes to the electrochemical potential of the EDL. By considering the charge density and steady state double layer potential as response curves, we can explain the loss of signal quality at high concentrations of supporting electrolyte (Figure 5.3c). The increase in steady-state potential and charge density (derived from the model) slows at high concentrations, and a similar effect occurs experimentally to the Debye potential. The decrease in slope of the response curves at high concentration will result in smaller signals from the analytes, resulting in the decrease in SNR observed at high concentrations of supporting electrolyte. The observation that the measured steady state potential and charge saturation follow similar curves suggests that this may be a useful method for quantitatively characterizing solutions containing charged species, as well as a method of characterizing individual analyte molecules.

5.5 <u>Conclusion</u>

A new modality for detecting and identifying small molecular analytes in a nanopore was demonstrated. The double layer potential signal is dependent on the change in Debye potential in the solution within the nanopore due to the valence charge and size of the analyte molecule. The magnitude of the double layer potential signal is insensitive to pH and logarithmically related to the concentration of the supporting electrolyte. The ionic current signal is sensitive to pH indicating that the overlapped double layer region in this nanopore is primarily populated by positively charged species. The relative magnitude of the double layer signals from different analyte molecules is only weakly sensitive to the

concentration of the analyte in solution, indicating that the signal is due to single molecules translocating the nanopore. The double layer potential signal derived from the converged numerical model of the system reflected the experimental trends, confirming the dependence of the signal on the charge of the analyte and a weak dependence on the size of the molecule. In numerical and experimental studies, the potential signal was found to be consistent with Debye's analysis of the electrical effect of charged species in solution. The double layer potential signal offers a fundamental improvement over the ionic current signal in that the potential signal is independent of the solution pH and the transport parameters of the analyte molecule.

Table 5. Constants, variables, and values.

Symbol	Description	Unit
a_j	Activity of j	1
A	Minimum cross sectional area of the conical nanopore	nm^2
α'	Polarizability volume	$Bohr^3$
c	Concentration of the bulk solution in the reservoirs	millimolar
c_j	General concentration term for solvated electrolytes	millimolar
C_{EDL}	Electrical double layer capacitance	F/m^2
d	Density	g/cm^3

D_j	Diffusion coefficient for solvated electrolytes	D_{Cl}	2.03e-5 (cm^2/s)
		D_K	1.96e-5 (cm^2/s)
		D_{Na}	1.334e-5 (cm^2/s)
		D_F	1.475e-5 (cm^2/s)
		D_{H+}	7.9e-5 (cm^2/s)
δ	Thickness of the compact layer		nm
e	Electronic charge		1.602e-19 C
ε_r	Relative permittivity		
ε_0	Permittivity of free space		8.8542e-12 (F/m)
ε_p	Permittivity at the wall of the nanopore		2
ε_s	Nominal permittivity of the electrolyte solution		80
F_c	Faraday's constant		96485.34 (C/mole)
$\vec{F}_V$	Volume force		N/m^3
g	Fitting term for smoothly varying permittivity in the compact layer		
γ	Fluid viscosity		Pa s
γ_j	Activity coefficient of j		1
h	Fitting term for smoothly varying permittivity in the compact layer		

I	Identity matrix	
I_l	Electrical current applied to gold layer	pA
k_B	Boltzmann constant	1.381e-23 (m^2 kg/s^2 K)
Kn	Knudsen number	1
L	Nanopore length	nm
λ_D	Debye length	nm
M	Molar mass	g/mole
μ	Electrochemical energy of a solution	J/mole
μ^0	Standard electrochemical energy of a solution	J/mole
μ_{eo}	Electroosmotic mobility	m^2/(V s)
$\mu_{m,j}$	Mobility of solvated electrolytes	$\mu_{m,Cl}$ 8.23e-13 (s mole/kg)
		$\mu_{m,K}$ 7.95e-13 (s mole/kg)
		$\mu_{m,Na}$ 5.48e-13 (s mole/kg)
		$\mu_{m,F}$ 6.05e-13 (s mole/kg)
N_{AV}	Avogadro's number	6.022e23
N_j	Number of particle j in solution	1
P	Pressure	Pa

φ_2	Unbiased surface potential due to the material work functions	-0.2 V
φ_e	Debye electrical potential of a solution	V
φ_j	Thermodynamic potential of particle j	V
φ_k	Classical Planck potential of a solution	V
Q_0	Double layer electrode charge	C/m^2
r_0	Radius of the nanopore at an arbitrary position	nm
r_1	Radius of the small opening of the nanopore	nm
r_2	Radius of the large opening of the nanopore	nm
r_3	Radius of the simulated particle	nm
r_j	Radius of particle j	nm
R	Gas constant	8.314 (J/mole K)
R_j	Rate of production of solvated electrolytes	mole/(s m^3)
ρ_c	Distribution of charge carriers within the model	C/m^3
ρ_m	Fluid mass density	kg/m^3
T	Temperature	296.65 (K)

τ	Viscous stress tensor		
u	Fluid velocity		m/s
V	General potential term within model		Volts
V_0	Potential applied across the length of the channel		0.15 (V)
V_{DL}	Double layer potential		V
x	Inverse of the Debye length		1/nm
X_j	Mole fraction of j		1
z_j	Valence of charged particles	z_{Cl}	-1
		z_K	+1

CHAPTER 6 : DUAL CHANNEL DNA SEQUENCING IN A NANOPORE FLUX CAPACITOR

6.1 Introduction

We present a dual channel DNA sequencing system in which measurements are made in parallel for the ionic current and the electrochemical potential of the electrical double layer within a solid-state nanopore. By increasing the quantization of the two measurement channels and considering a multi-nucleotide DNA input with a hidden Markov model approach, we are able to tune the nanopore sensor system for higher sequencing accuracy. The double layer potential signal alone was sufficient to produce DNA basecalling accuracy of >99% in the evaluation set of short DNA. The maximum sequence accuracy of the ionic current signal alone was found to be limited to less than 80% with the same evaluation set of DNA. When the resolution of the measurement channels (and therefore the sequencing accuracy) was at a sub-maximal value, we were able to produce higher accuracy than in either individual channel by combining the measurements in parallel. By establishing this approach of dual channel sequencing with consideration of the multi-nucleotide resolution of the nanopore sensor, we demonstrate a new method of high accuracy DNA sequencing with unmodified DNA in a non-functionalized, solid-state, nanopore. This method requires only minimal reagents consisting of the electrolyte solution and DNA sample. No operational lifetime for the device has been noted, with measurements made from the same device over a timescale of months with no noticeable degradation.

Nanopores have long been considered as the future of DNA sequencers, where DNA is passed through a nanopore and each nucleotide base is read as it translocates.[20,21,24,39,81,93] Many varieties of nanopores with variations in structure, materials, and signal transduction mechanisms have been introduced since the idea was first published in 1995.[94,95] The accuracy of the sequences produced by these methods does not yet compete with state-of-the-art next generation sequencers. The range of transduction mechanisms that have been developed with the goal of producing a nanopore DNA sequencer include monitoring the ionic current through the nanopore (the blockade signal), functionalized sites within the nanopore, tunneling electrodes across the nanopore, and transverse conductance measurements in a molecularly thin material.[17,19,22,23,25,42] However, in all cases there have been some limiting factors which preclude high accuracy basecalls, such as high noise levels, non-constant translocation factors, limited nucleotide resolution, or proneness to analyte orientation in the nanopore.

In the typical case, nanopore sensors rely on measurement of the ionic current through the nanopore, which arises due to the transport of charged species. Changes in the ionic current occur due to physical occlusion of the nanopore and the translocation of charged analytes.[20,39,91] In DNA sequencing applications, a chain of negatively charged nucleotides move through the nanopore, but the translocation rate may vary depending how much of the strand has passed through the nanopore.[74] This limitation means that the ionic current signal from a given nucleotide may be sensitive to both the particular nucleotide properties and the location of the nucleotide on the strand, as well as the physical and electrical conditions of the nanopore. Because of this sensitivity, along with

145

high noise levels in the sub-molecular measurement, DNA sequencers relying on this method alone typically require additional systems to control translocation rate. In our previous work, we have demonstrated a new nanopore sensing technique that complements the ionic current method while being less sensitive to the transport mechanics of the analyte.

We have previously developed a novel method of molecular detection in a nanopore that is sensitive to changes in the electrochemical potential within the nanopore. By detecting changes to the electrochemical potential of the solution within the nanopore using an axisymmetric ring electrode, this electrochemical method of nanopore sensing reduces dependence on analyte orientation and minimizes sensitivity to analyte velocity. While the electrochemical method alone is still sensitive to the relatively high noise levels of sub-molecular measurements, it also allows simultaneous collection of the ionic current signal. The consideration of simultaneous, dual channel, sub-molecular measurements allows us to consider combined measurements with decreased statistical uncertainty.

Since it is possible to simultaneously measure the double layer potential and ionic current through the nanopore, we developed an error tolerant DNA sequencing method in which the two sensing modalities may be used individually or in combination. By manipulating the quantization of the outputs in the sensor design, we are able to account for the situation where multiple nucleotides are interrogated by the sensor (1 or 2 nucleotide combinations). Key advantages of this device are that the nanopore may be produced by nanoscale fabrication techniques with conventional solid-state materials, the

146

device is reusable with a long operational life, and requires only minimal reagents (aqueous electrolyte solution and DNA). By taking a computational and machine learning approach with a dual-channel signal, we demonstrate a method of improved nanopore sequencing without chemical modification of the DNA or sophisticated translocation controls.

## 6.2 Methods

6.2.1 Experimental Setup

Our nanopore sensing apparatus has been described in our previous work. Briefly, a thin membrane composed of 50 nm of LPCVD SiN and a thin (10 nm) gold electrode was prepared. A nanopore was patterned on the thin membrane with electron beam lithography and etched with inductively coupled plasma. The conductance of the nanopore in 100 mM NaF was 2 nS, consistent with nanopores with diameter <10 nm as found in our previous studies and literature.[39] The nanopore was placed in a flow cell with an aqueous, 1 mM NaF solution containing purified dsDNA at pH 10. PH was adjusted by addition of NaOH solution in order to denature the DNA. Only one type of DNA was sampled per acquisition experiment. DNA was purified PCR product with length 154-463 bp. DNA was driven through the nanopore under an electric field (0.5 V/m) established between the two fluid reservoirs by a pair of calomel electrodes. The gold ring electrode of the nanopore was charged with a small constant electrical current (37.4 ± 3.2 pA) and the charging potential was recorded. The ionic current between the calomel electrodes and the charging potential at the ring electrode were digitized at 80

kHz with custom Matlab software (Mathworks, Matlab 2013a, MA) and a National Instruments data acquisition board (National Instruments, NI PCI-6221, TX). The data acquisition hardware operates with clock speeds up to 833 kHz and 16 bit precision. The ionic current and double layer potential traces are filtered with a digital passband filter (70-1500 Hz, 50 dB/dec) in order to eliminate as much noise as possible while maintaining high resolution signals. The dual channel acquisition was evaluated in post-processing with a sophisticated custom basecaller algorithm. Hidden Markov model (HMM) training was processed on the Clemson Palmetto Cluster with up to 550 GB of memory. Over the course of developing the basecaller algorithm to a high level of sophistication (months), repeated measurements from the same devices showed no signs of degradation.
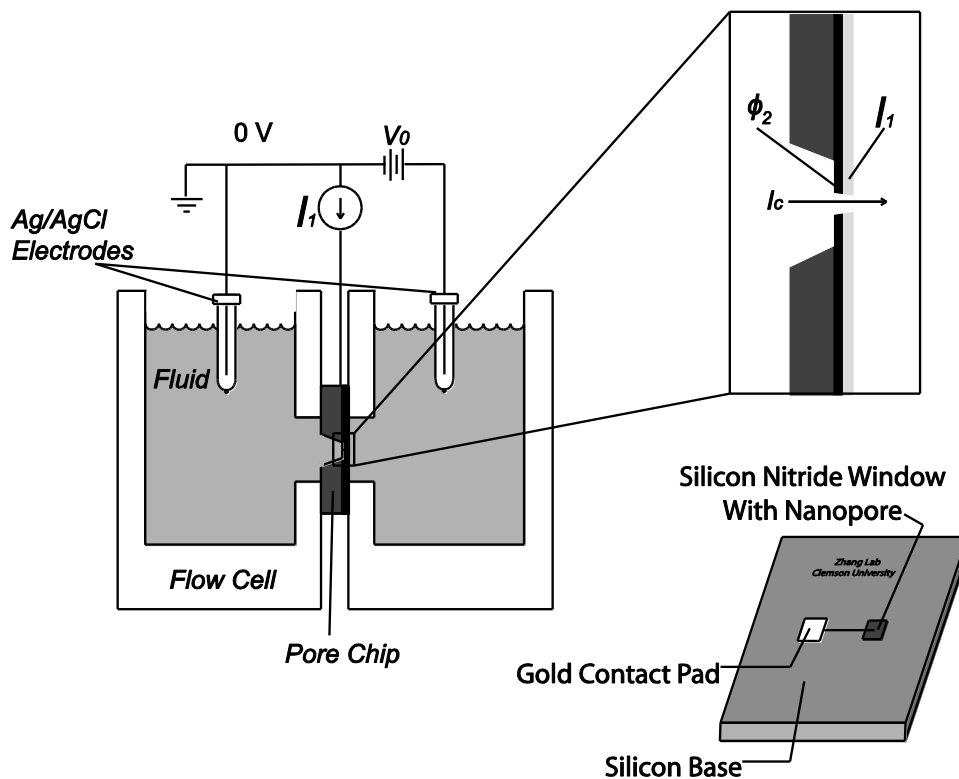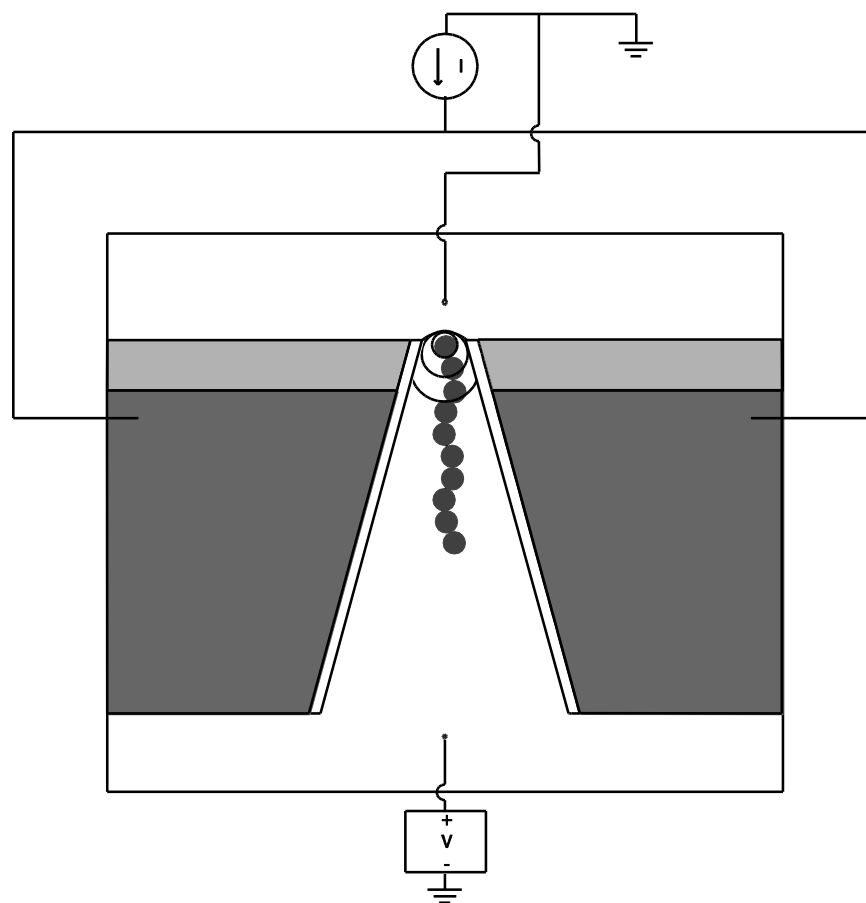
b.

Figure 6.1. a. Experimental setup diagram. b. Diagram of the 1-3 nucleotide sensing

regions as DNA translocates the nanopore.

6.2.2 *Algorithm Description*

Designing a non-functionalized sensor is an exercise in mapping the signal source to

the sensor outputs in a reliable and error-tolerant way.[96] In a general case, there is a set of

input symbols (the input space) and a set of output symbols (the output space), with the

sensor serving as a noisy function transforming data between the spaces. The input space

consists of the set of allowable inputs to the sensor and the output space consists of the

set of signals which may be generated by the sensor. In order to properly map the signal

source (*n*-nucleotide segments) to sensor outputs (quantized electrical signals), we must have an idea of the number and range of the symbols in each space. In an ideal situation, the signal source would be the 4 bases (A, G, C, T) and the output signal would be quantized to 4 levels. However, fabrication of a nanopore sensor with true single-nucleotide resolution has proven to be difficult, and even devices which get close to the desired size are affected by high noise levels. It has been shown that considering a multi-nucleotide signal source where the input signal is a measurement of a short segment of DNA (for example, a 3 nucleotide region composed of the nucleotide of interest and the 2 nearest neighbors) can increase the accuracy of the ionic current signal in determining the correct sequence of the parent strand.[97] When DNA is the signal source, the size of the input space increases in powers of 4 (due to the 4 base nucleotides), so that for a sensor with *n*-nucleotide resolution, there must be 4^n inputs and at least as many output symbols. For example, if *n* = 1, the 4^1 symbols in the input space are {'A', 'G', 'C', 'T'}. If *n* = 2, the $4^2 = 16$ symbols in the input space are {'AA', 'AG', 'AC', 'AT', 'GA', 'GG', 'GC', 'GT', 'CA', 'CG', 'CC', 'CT', 'TA', 'TG', 'TC', 'TT'}, and for n = 3, there are $4^3 = 64$ input symbols consisting of triplets like 'AAA'. In order to reduce collisions (where multiple inputs map to the same output), it is desirable to increase the number of symbols in the output space compared to the number of input symbols. In a nanopore, the high noise levels of any individual data channel will likely limit sufficient resolution in the output to allow discrimination between the different sensor inputs. At some point the resolution of the sensor outputs will fall below the channel noise level and similar outputs will be statistically indistinguishable. Improving the resolution of the output may be done

by reducing the noise of the sensor as much as possible, or by statistically reducing the uncertainty of the output by considering multiple parallel measurements. By leveraging reduced uncertainty of the dual acquisition of ionic current and double layer potential signals, we are able to increase the number of levels in the output beyond that of any individual channel.

In the output space, since the measurements are made in two separate, parallel channels, any signal from one channel may be paired with one from the other. If the output of each channel is quantized into 4^m levels, the total number of levels in the output space is 4^{mi+mv}, where m_i is the exponent in the ionic current channel and m_v is the exponent in the electrochemical potential channel (base 4 is used here to simplify size comparisons between the input and output spaces). For example if $m_i = m_v = 1$, then the 4 symbols in each output channel may be combined in 4^{1+1} ways (using the symbols 1, 2, 3, and 4, the combined output space contains the elements {11, 12, 13, 14, 21, 22, 23, 24, 31, 32, 33, 34, 41, 42, 43, 44}). Thus, due to our dual channel approach, the total size of the output space is the product of the size of the spaces of the individual channels. Even though the sensor must be designed with at least one distinct output symbol for each input symbol (at least 1 to 1 mapping), having more output symbols than input symbols will reduce the probability of mapping a collision. In order to satisfy the minimum requirements of 1 to 1 mapping, the relationship between exponents (m_i+m_v) and n must be such that $(m_i+m_v) >= n$, where $(m_i+m_v) >> n$ is desirable. By manipulating the size of the output space in this way, we are able to accommodate both the multi-nucleotide resolution of our nanopore sensor and reduce the probability of collisions between the

input and output to a negligible level. In evaluation of a wide range of values for m_i and m_v, some cases for large values (m_i or $m_v > 7$) were not able to be completed with the resources available.

Within the two data channels, the beginning and end of DNA strand translocation events were identified by an edge detection algorithm. The length of time between the ends of translocation events was used as a criterion to identify segments which likely contain DNA signals. Time segments which fall in an empirically determined range were identified as likely translocation targets (Figure 6.3). These data segments were further sub-divided into regions corresponding to nucleotide events, where nucleotide events were demarcated by local extrema within the data segment. In each data segment and nucleotide region, correlation of the position of demarcations in both the ionic current trace and double layer potential trace was considered as a requirement for further processing. Essentially, simultaneously occurring data segments with similar duration were identified in the two data channels. The positions of extrema within pairs of data segments were compared. Data segments with similar duration and extrema positions were retained. Each data segment was converted to a vector of signal values consisting of the value at the midpoint of each nucleotide event. The signal value vectors from the sensor were each quantized to 4^m levels with a least squares method within a fixed, empirically determined range (30 mV range for the double layer potential signal and 1.2 nA range for the ionic current signal). With the ionic current and double layer potential data normalized, the rank sequences are quantized into a 4^{mi+mv} sized space using the formula: $S = 4^{mi} S_{DL} + S_{IC}$, where S is the encoded signal, S_{DL} is the rank sequence from

152

the double layer potential channel, and S_{IC} is the rank sequence from the ionic current channel (Figure 6.2). The encoded signals were decoded into the 4^n input space with a hidden Markov model (HMM). A separate HMM was trained for each combination of n, m_i, and m_v. Sensor data that was decoded into 4^n space with a multi-nucleotide HMM was deconvolved into the 4 base values using the discrete convolution vector $f(x) = 4^x$, where x falls in the range $[0, n\text{-}1]$.

DNA samples with known sequence were used to train HMMs for a range of values of n, m_i, and m_v. The training data consisted of 96 data files from 32 DNA samples with over 10^5 reads from PCR amplified DNA (154-463 bp in length). The HMMs were evaluated on a data set containing 3 DNA samples (3 data files). Training consisted of obtaining the sensor output via experiment and estimating the transition and emission probability matrices of the HMM with chosen values of n, m_i, and m_v. On the input side, known sequences of the DNA were numerically encoded using the key-value pairing: T = 0, G = 1, A = 2, C = 3. The encoded, known, input sequence was convolved with a vector to produce the sequence in 4^n-space, where n is the multi-nucleotide resolution of the sensor. The convolution vector is the discrete function $f(x) = 4^x$, where x falls in the range $[0, n\text{-}1]$. Simply, the vector contained n elements where each element is *4* raised to its index in a zero-indexed vector system: $(4^0, 4^1, 4^2, \dots, 4^{n-1})$. In this system, the convolution vector for two nucleotide resolution ($n = 2$), is $(4^0, 4^1) = (1, 4)$. For three nucleotide resolution (n = 3), the vector is $(4^0, 4^1, 4^2) = (1, 4, 16)$, etc. The encoded 1-nucleotide sequence is transformed into a higher n-nucleotide resolution sequence by taking the convolution of the sequence with the appropriate convolution vector. Discrete

convolution finds the cross product between the reversed convolution vector and the first n elements of the sequence, sums the elements of the cross product, and then iterates along the length of the sequence vector. For example, to transform a sequence of 5 nucleotides in 1-nucleotide ($n = 1$) input space (T, G, A, C, T) = (0, 1, 2, 3, 0) into 2-nucleotide ($n = 2$) input space, the sequence is convolved with the convolution vector $f(\text{x})$ = $(4^0, 4^1)$, where x takes the values of [0, 1]. The convolved sequence is

$(4^1 \cdot 0 + 4^0 \cdot 0), (4^1 \cdot 0 + 4^0 \cdot 1), (4^1 \cdot 1 + 4^0 \cdot 2), (4^1 \cdot 2 + 4^0 \cdot 3), (4^1 \cdot 3 + 4^0 \cdot 0),$ which

simplifies to $(0, 1, 6, 11, 12)$. The encoded and convolved sequence was considered as the sensor input and the digitized nucleotide event vectors were considered as the sensor output. Accuracy was evaluated by finding the proportion (as a percentage) of matching bases between the predicted and expected sequences, where the expected sequences were provided by the DNA supplier.
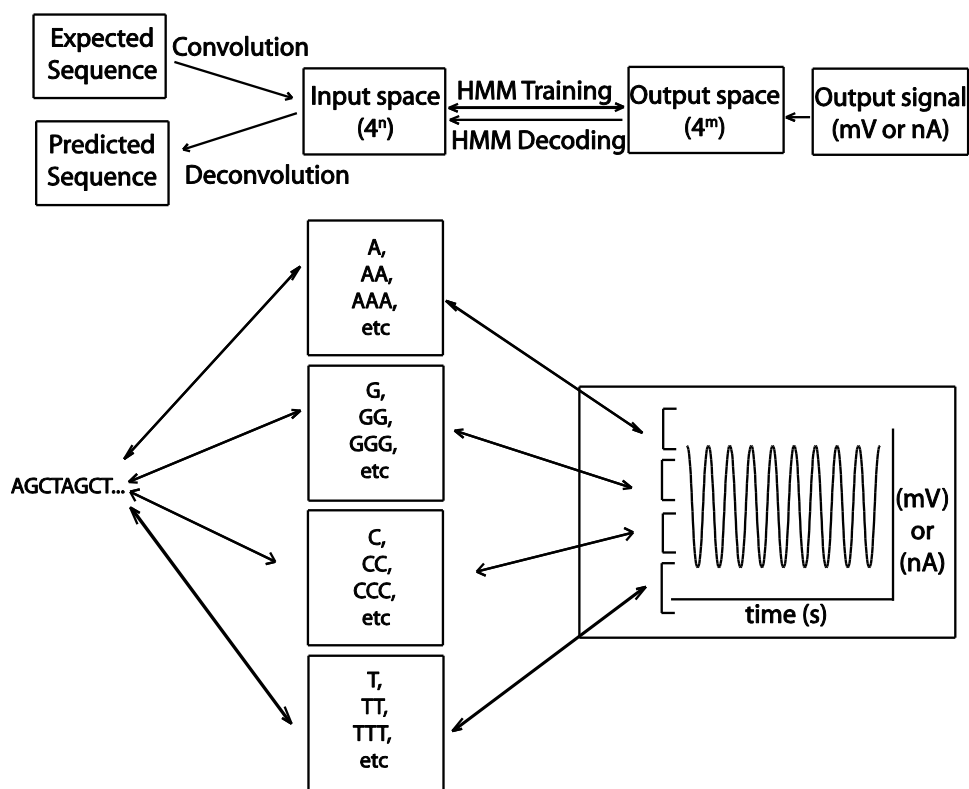
a.

Figure 6.2. The flow of information in the nanopore sequencing system. The expected

DNA sequence is transformed into 4^n space while the output sensor data is quantized into

4^m space. The hidden Markov model is trained by comparing the input and output spaces.

To determine the sequence of a DNA sample from the sensor output, the output is

quantized, decoded, and deconvolved.

6.3 <u>Results and Discussion</u>

Translocation events were detected by identifying sequential transitions in the data

traces by an edge detection algorithm. Figure 6.3a shows a typical distribution of the

duration of translocation events detected in the filtered double layer potential data. The

distribution of the durations is bimodal with a first peak centered at 20.8 ms and a second

155

peak shown here centered at 69.2 ms, although the location of the second peak is dependent on the length of the DNA strand under investigation. A bimodal distribution of translocation events is consistent with observations of DNA translocation studies, where the first peak is typically noise or incomplete translocation events.[23,98] The second peak (shown in Figure 6.3b) has a variable location that is linearly correlated to the length of the DNA strand $\left(t = 0.0112 + 0.0002\text{L}, \text{R}^2 = 0.9744\right)$, where t is time in seconds and L is the length of the DNA strands in nucleotides. The location of the first peak is not correlated to the length of the DNA sample. The linear relationship between the length of the DNA strand and translocation time indicates that the translocation is fast, with an average rate of 200 μs/nucleotide. The time resolution of our measurements was 12.5 μs (80 kHz), so the translocation events and nucleotide signals are well sampled at this translocation rate. A rate of 200 μs/nucleotide is similar to what has been observed for electrokinetically driven DNA translocation in solid-state and α-hemolysin nanopores.[40,81]
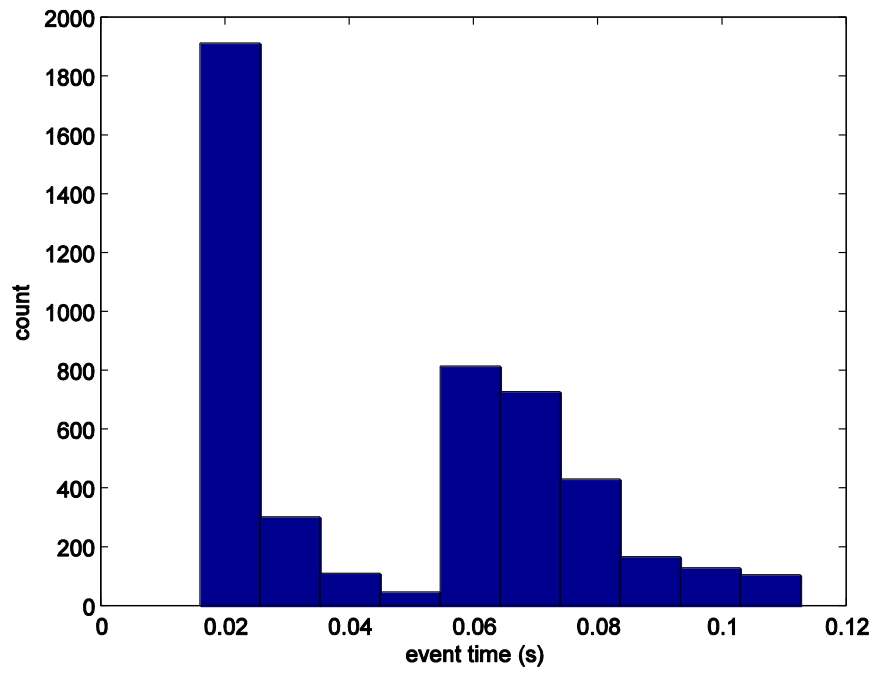
a.
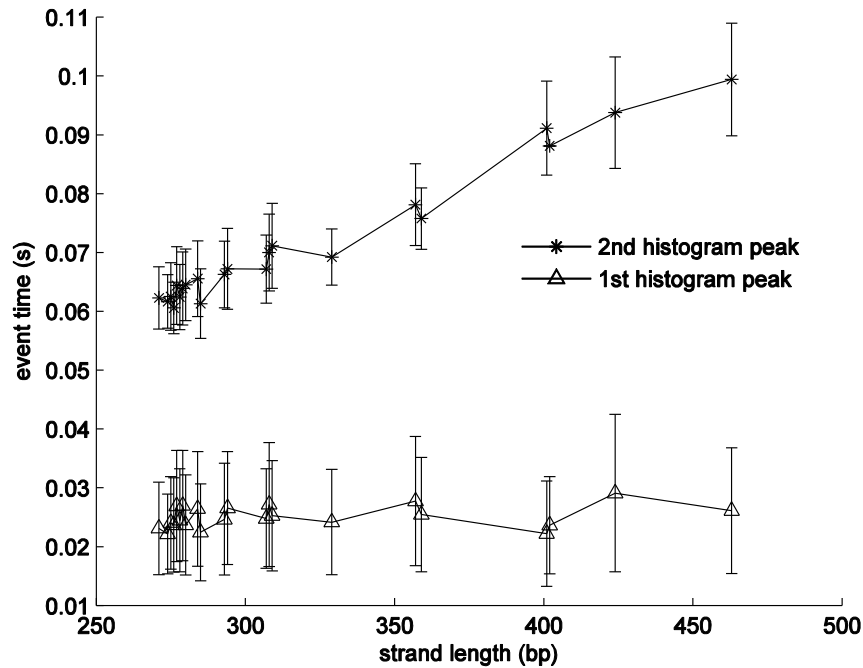
b.

Figure 6.3. a. The bi-modal distribution of translocation events observed in the double layer potential signal trace. b. The translocation time associated with the second peak is linearly related to strand length.

Figure 6.4 shows the signal resolution and accuracy of the double layer potential signals from the evaluation data set as a function of the size of the output space for 1 and 2 nucleotide resolutions. Figure 6.4 indicates that the accuracy of the double layer potential is constant in each case when the output space is quantized to fewer than 4^7 levels (16384 levels). Above 4^7 levels in the output space, the accuracy of the double layer potential signal rapidly increases with increased quantization. Quantization of the double layer potential output was increased up to 4^9 levels, at which point accuracy approaches 100% for all cases considered. The maximum accuracy observed is 99.3% for

1-nucleotide resolution and 94.9% for 2-nucleotide resolution, all occurring at the 4^9 quantization level. For each sample in the evaluation data set, the accuracy of the double layer potential was higher for the 1-nucletide resolution case compared to the 2-nucleotide resolution case, suggesting that the double layer potential signal is generated by single nucleotide segments of the DNA sample. The output resolution of the sensor increases with increasing quantization of the output, since the maximum range of the electrical output is fixed. For quantization levels from 4^1 to 4^9, the resolution of the double layer potential ranged from 4.25 mv to 114 nV (where the output resolution is the signal range divided by the number of quantization levels). The accuracy of the basecalls increases rapidly at quantization levels greater than 4^7 (corresponding to a resolution of 1.8 μV). The smallest resolution observed is much smaller than expected due to the typical noise level of the signal, however, the HMM method is error tolerant and clearly offers advantages in this case.
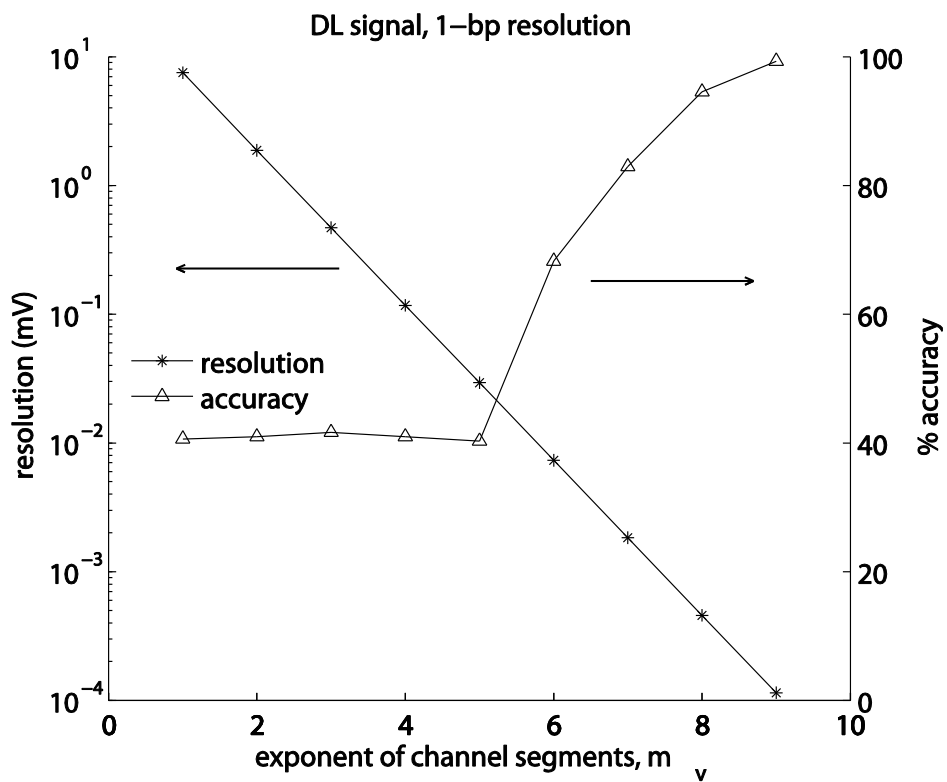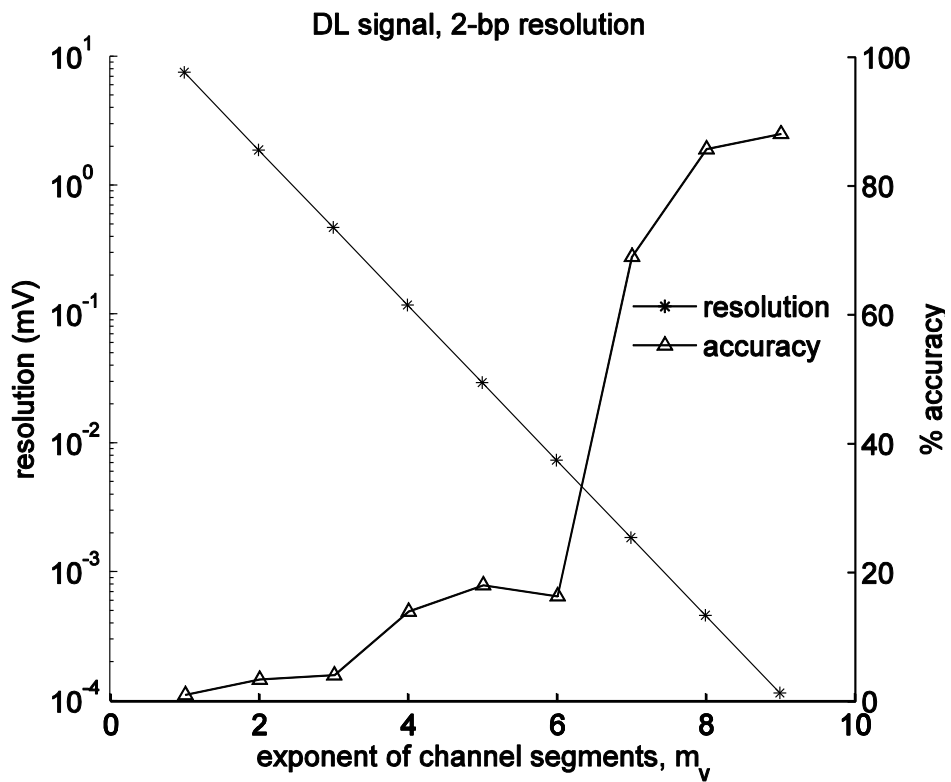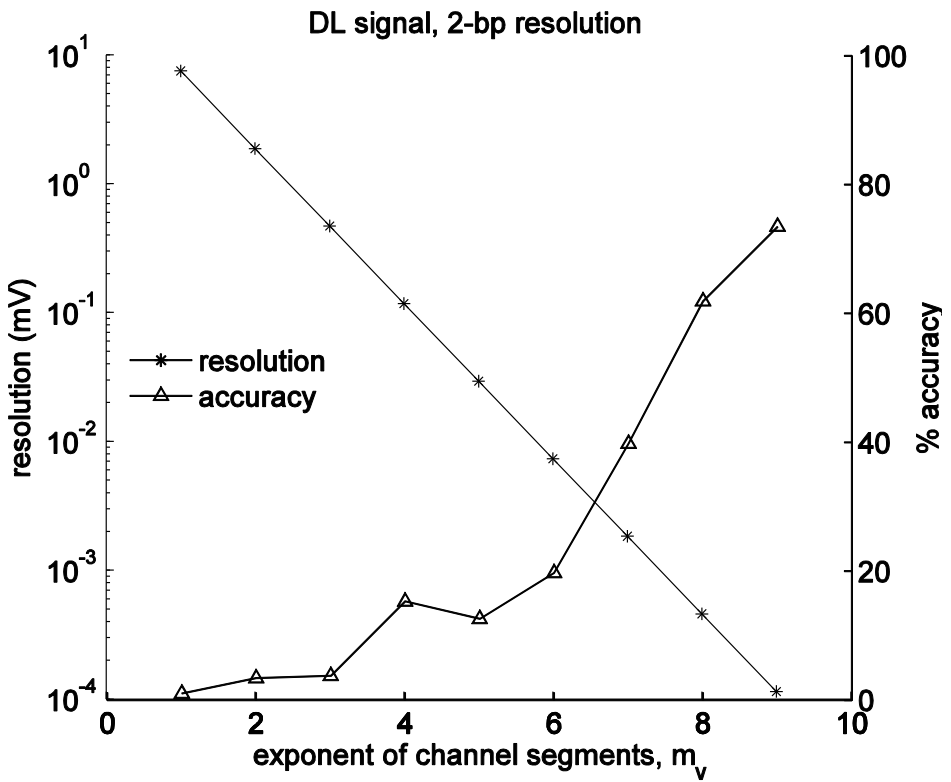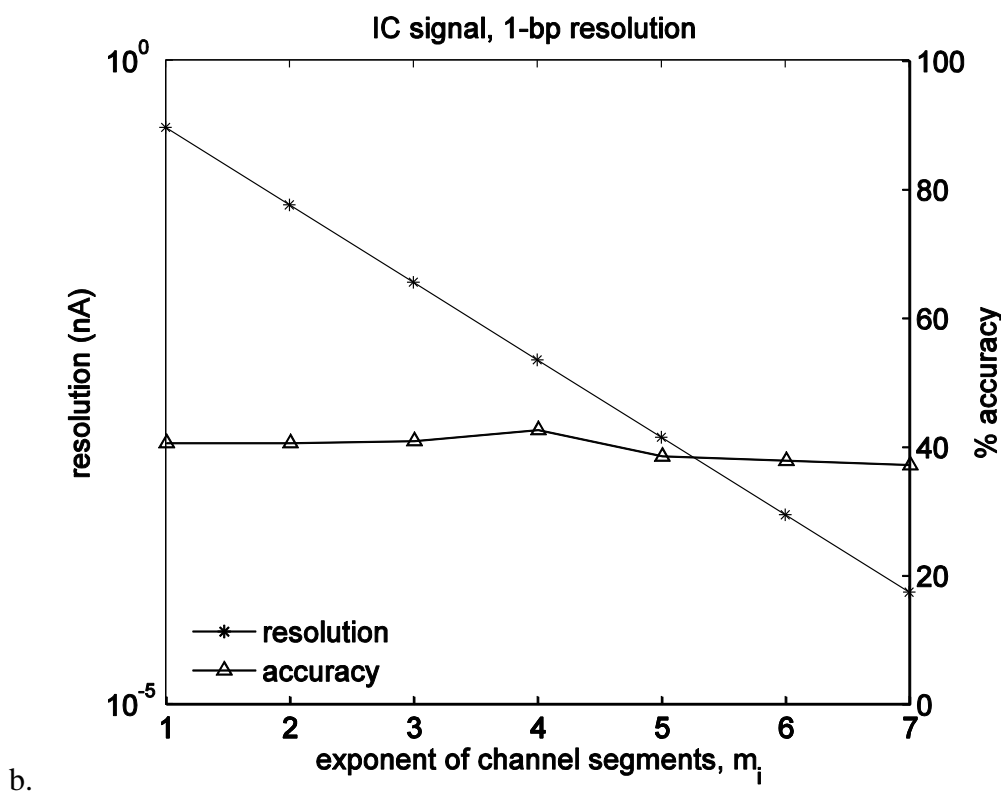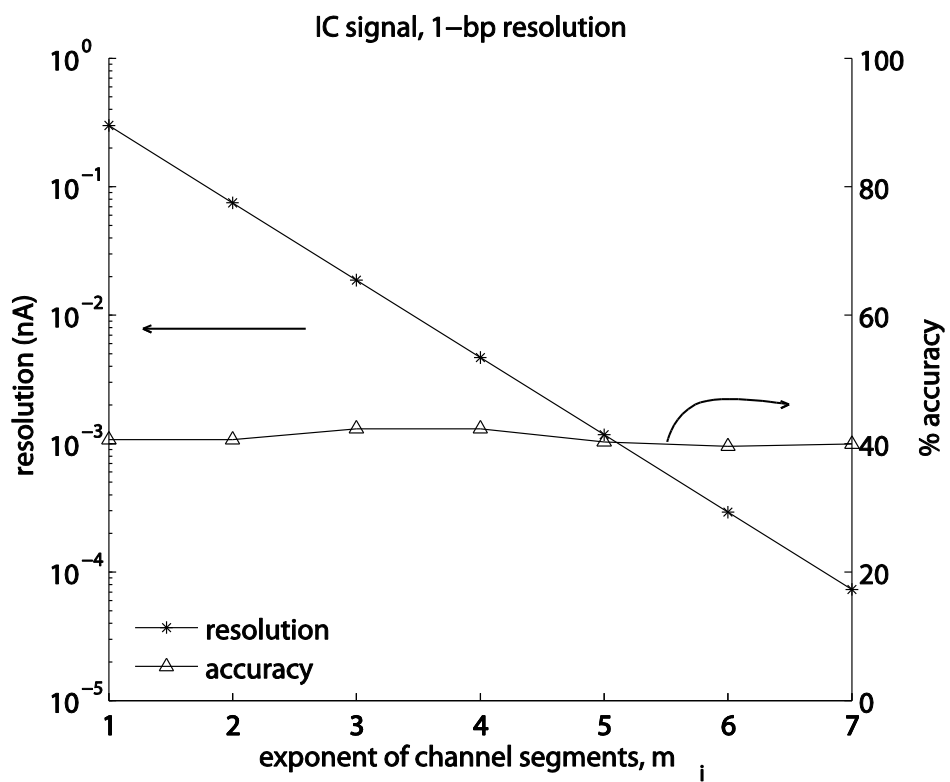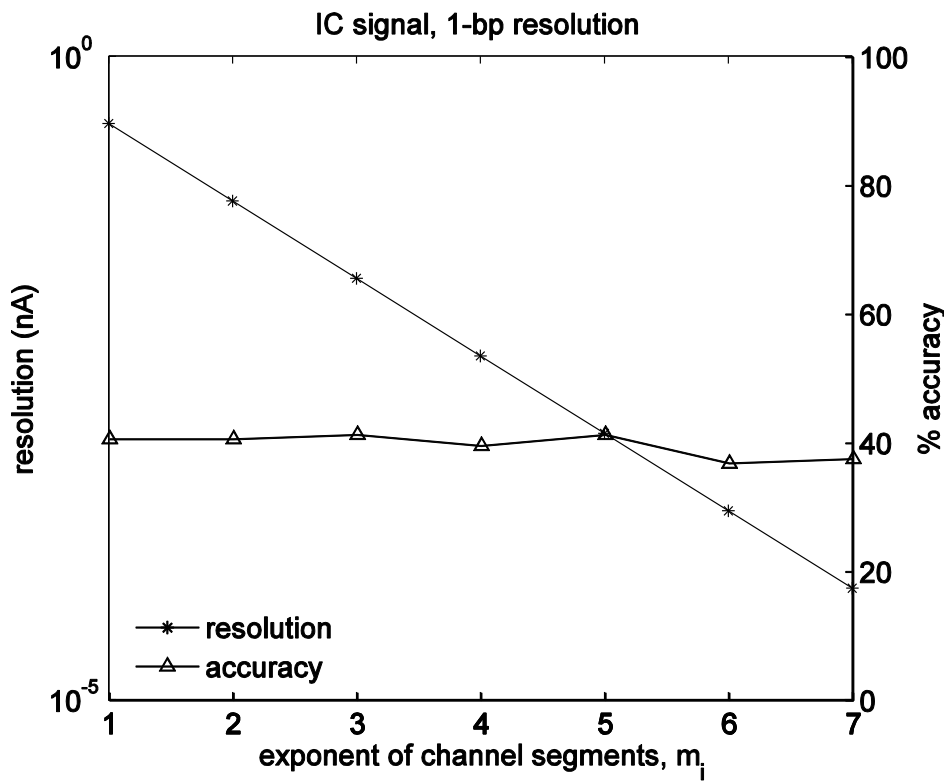
a.
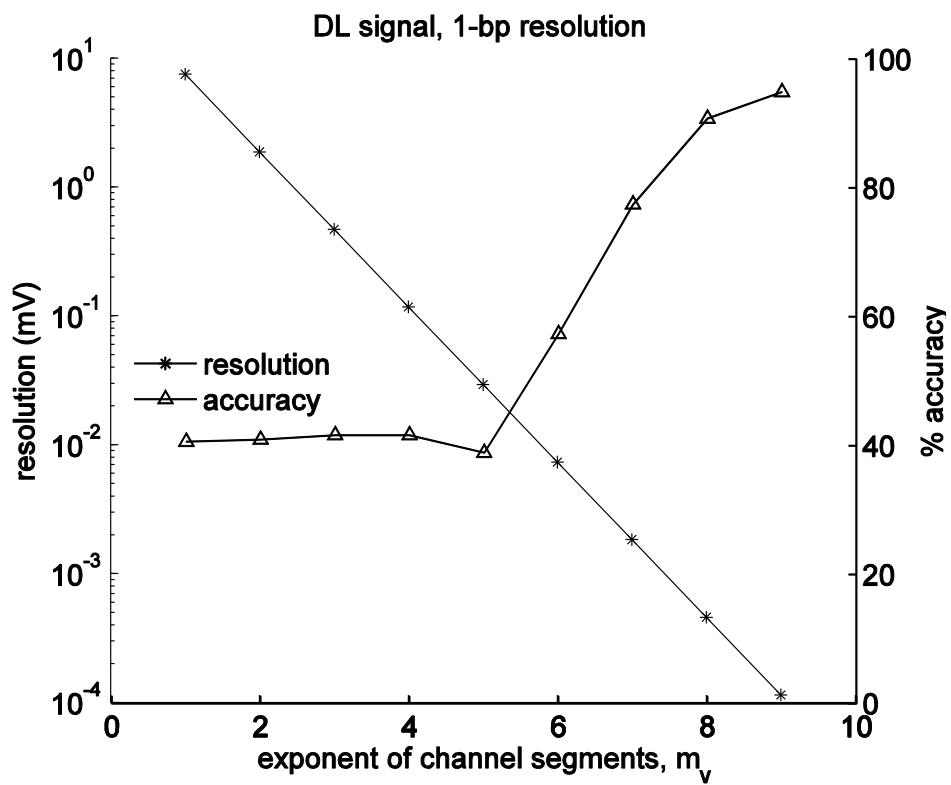
b.
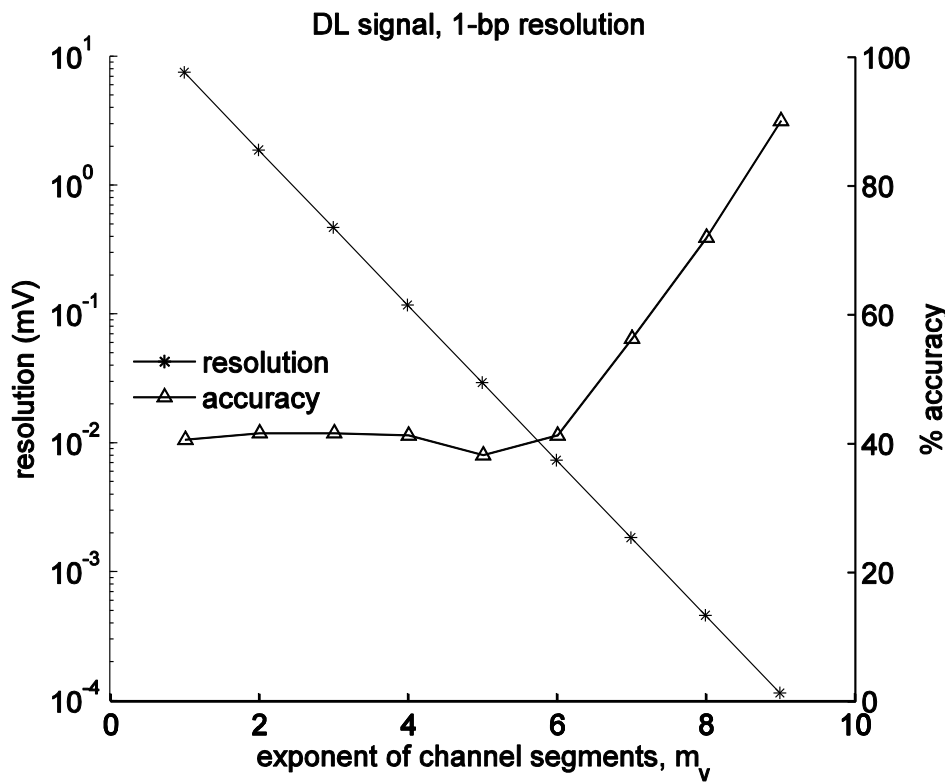
c.
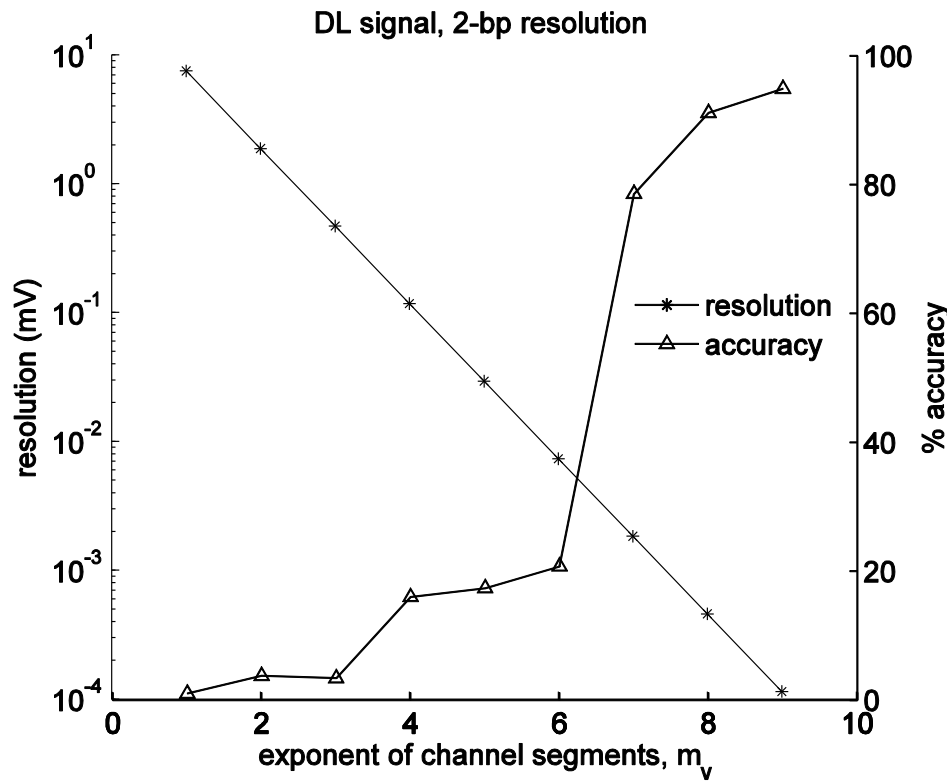
d.

e.

f.

Figure 6.4. a. The accuracy and output resolution of the sensor for the double layer potential signal with 1-nucleotide resolution in the three DNA samples of the evaluation set (a-c) and 2-nucleotide resolutions (d-f) in the same data set. In evaluation sample 1 (a, d), sample 2 (b, e), and sample 3 (c, f), the 1-nucleotide resolution has the higher accuracy in the double layer potential signal.

Figure 6.5 shows the percent accuracy of the evaluation data set from the ionic current channel alone. For the 1-nucleotide case (Figure 6.5a-c), the accuracy shows no dependency on the quantization level of the output. The 2-nucleotide case (Figure 6.5d-f) does show a dependency on quantization level of the output, and accuracy increases up to 77.6% at the highest quantization level (4^9, corresponding to a 4.6 fA quantized step size). Previous studies have shown that considering the actual nucleotide resolution of the nanopore will increase the accuracy of the basecalls when using a HMM method.[97] The high accuracy of the 2-nucleotide resolution case (Figure 6.5d-f) indicates that the ionic current signal is related to 2-nucleotide regions of the translocating DNA. The fact that there is a dependency on nucleotide resolution in the ionic current signal, but not the double layer potential signal, indicates that these different modalities are independent and do not share the same sub-molecular resolution. It is understood that DNA will stretch to more than twice the relaxed distance between bases (stretch to 0.58-0.75 nm from 0.34 nm) in a small nanopore under a moderate electrical field. [53,99,100] The thickness of the narrow, metallic region of this nanopore is in the range of 5-10 nm, which is much larger

than the expected length of 1 or 2 bp segments of DNA. However, our previous modeling work has indicated that the nanopore signals are generated in the narrowest portion of the nanopore (the cross section with the minimum area and smallest radius of curvature) such that the actual sensing length of the nanopore is much smaller than the total length of the nanopore and similar to a 1- or 2-nucleotide segment of DNA (0.5 - 1.2 nm).
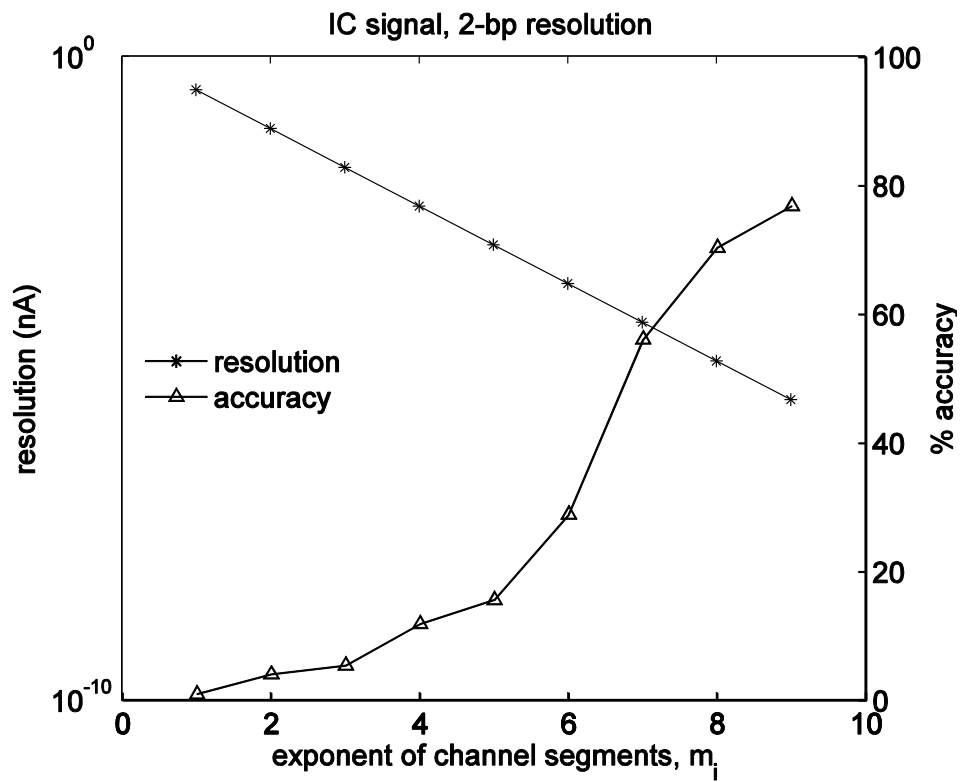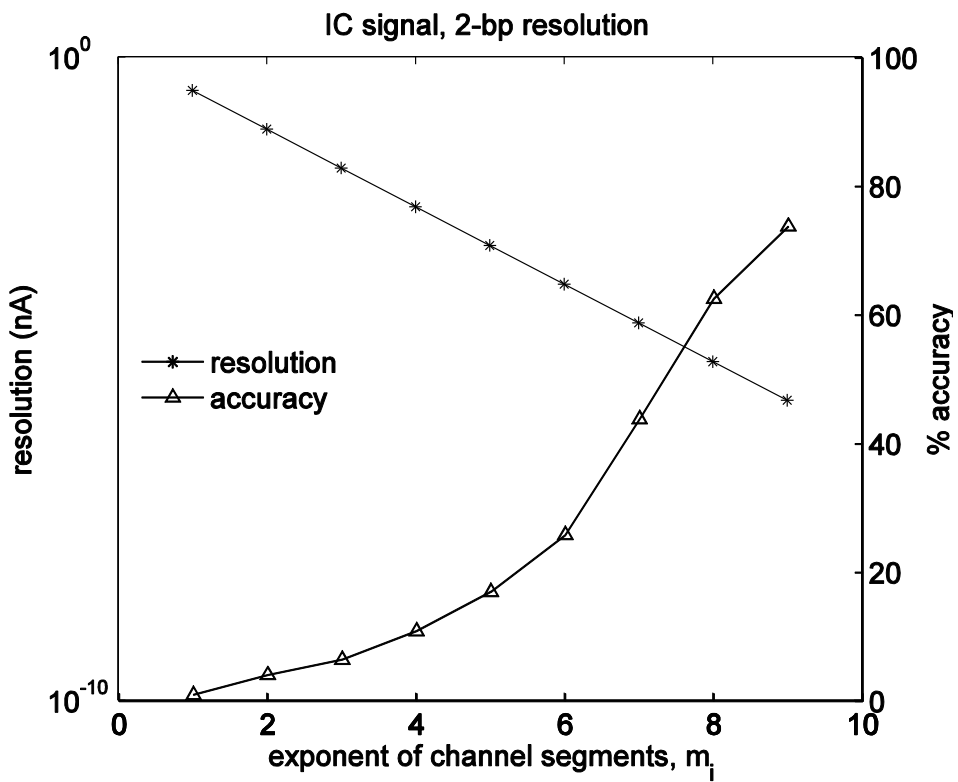
a.

b.

c.

d.

166
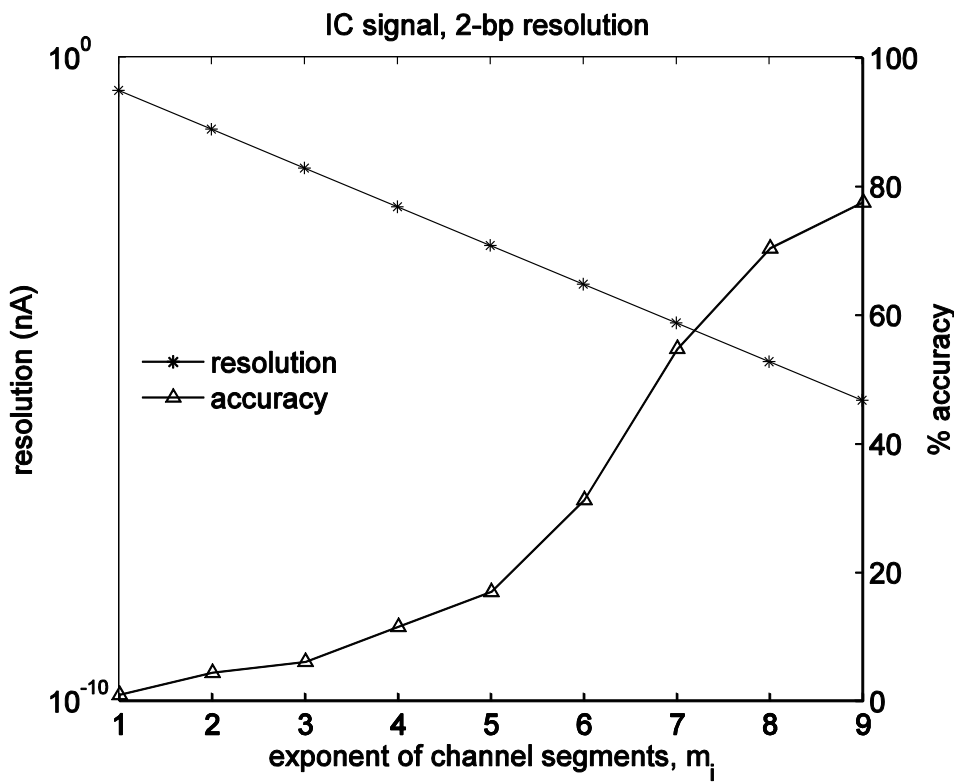
e.

f.

Figure 6.5. The accuracy and output resolution of the sensor for the ionic current signal with 1-nucleotide resolution in the three DNA samples of the evaluation set (a-c) and 2-nucleotide resolutions (d-f) in the same data set. In evaluation sample 1 (a, d), sample 2 (b, e), and sample 3 (c, f), the 2-nucleotide resolution has the higher accuracy in the ionic current signal.

Figure 6.6 shows the results of considering the dual encoded measurements of the ionic current and double layer potential. The dual channel measurements tend to have higher accuracy than the individual channels when the quantization of the individual channels are mid-range. When the accuracy of one channel is much lower than the other, the dual measurement accuracy may be lower than the higher individual channel accuracy as in maximum case where the double layer potential is producing >99% accuracy but the ionic current accuracy is limited to <80%. The dual channel method offers a trade-off in terms of computational speed and complexity, where lower resolution signals are simpler due to the smaller output spaces, but higher resolution in the double layer potential channel offers better single-molecule, single-read accuracy.

bp_res = 1

a.

bp_res = 2
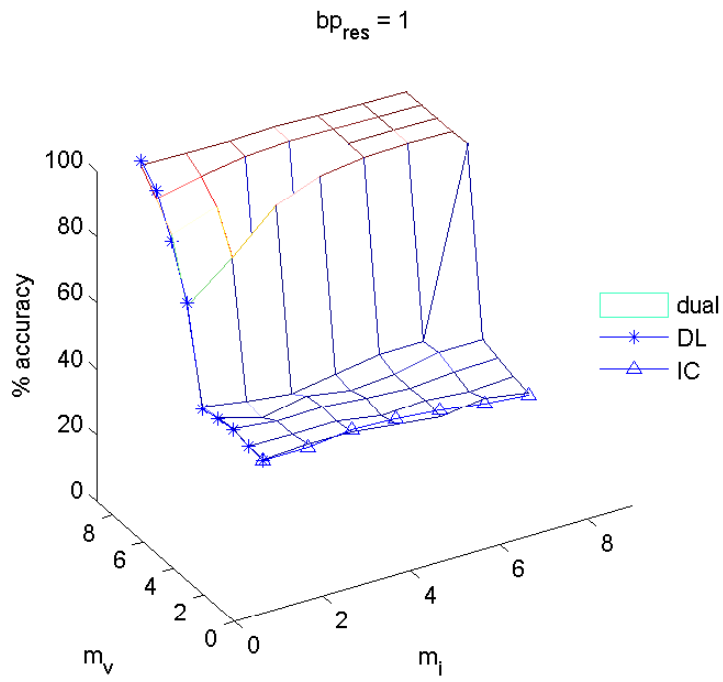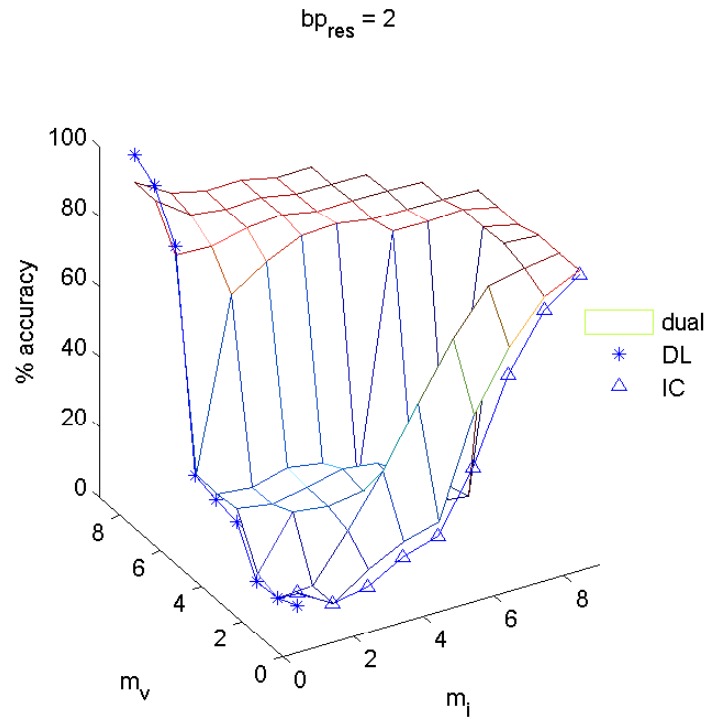
b.

Figure 6.6. Effect of independently changing the size of the output spaces of the ionic current (triangles), double layer potential (stars), and combined (surface) data channels with 1-nucleotide resolution (a) and 2-nucleotide resolution (b) on the sequencing accuracy. The accuracy of the combined data channels tends to be better than either of the individual channels. The dual channel accuracy is highest when considering 2-nucleotide resolution.

6.4 Conclusion

By considering double layer potential, ionic current, and combined channel acquisition methods in a nanopore sensor, we are able to attain high accuracy and resolution when sequencing individual DNA molecules. Based on the dependence of the accuracy on output quantization, the smallest discernible signal resolution of each channel was found to be 4.6 fA in the ionic current channel and a minimum resolution of 114 nV in the double layer potential channel at the 4^9 quantization level. We expected that the noise level would put an upper limit on the resolution of the sensor, but no such limit was observed in the range of resolutions considered. The non-functionalized method developed here may be improved by further reducing the noise levels of the measurements, decreasing the n-nucleotide resolution of the nanopore, or increasing the number of data channels output from the sensor. The difficulty of increasing the number of channels is that additional detection methods likely require additional materials to be deposited on the nanopore, and it would be difficult to maintain a low n-nucleotide resolution with a physically thicker nanopore. However, the double layer potential signal offers extremely high (>99%) accuracy in single-molecule, single-read DNA sequencing

of the short dsDNA samples in this study while the dual channel method can offer high accuracy (>90%) at lower resolution, offering a computational trade-off. The nanopore sequencing device is itself reusable and individual devices have been in use over a period of months in the development of this technology. The high speed and the minimal, cheap reagents (NaF, NaOH, and H_2O) required for this method make the technology promising for widespread genomic and genetic applications.

CHAPTER 7 : SUMMARY, CONCLUSION, AND FUTURE WORK

7.1 <u>Introduction</u>

Throughout this project the primary innovation has been manipulation and sensing of the electrical double layer in the nanopore. We began be establishing a numerical model of the electrical double layer. The model took into account features of the EDL that had previously been neglected in nanopore studies, but which we showed to be practically relevant. Namely, by including the compact layer and considering the work function potentials of the nanopore materials, we were able to show that the ionic conductance and material dependence could be accounted for in a harmonious and theoretically complete way. We then proceeded to experimentally probe this double layer structure by manipulating the surface potential of the nanopore. By changing the surface potential, we were able to control the nanofluidic characteristics of the nanopore in a predictable way. Expanding our numerical model gave us insight into the mechanics of the interactions and allowed us to refine our understanding of the behavior of the EDL in a nanopore. Specifically, we were able to correlate the charge density of the fluid in the nanopore with the applied potential, which can be characterized as a balance between the electrochemical potential in the EDL and the surface potential. Practically, this is manifested as a linear correlation between ionic charge in the solution and the potential at the nanopore surface. Such characterization allows us to directly relate the nanopore surface potential to the contents of the nanopore lumen. By altering the electrochemical

potential of the solution within the nanopore, we were able to produce changes to the nanopore surface potential. We introduced analyte molecules with known physical and electrical properties into the nanopore, which altered the charge density and electrochemical potential of the solution. In response to the changes to the solution due to the analyte molecules, the nanopore surface potential will also change. In effect, EDL detection is the inverse of EDL manipulation, where changes to surface potential alter the charge and structure of the EDL and vice versa. Further, because the electrochemical potential is related to the charge and size of the analytes, the response is graded and can be linked to the specific properties of the analytes. This specificity in the surface potential response indicated that the EDL signal would by useful for identifying translocating analytes. This was first shown with small molecules, where the signal was shown to have good sensitivity to the analyte charge and size, so that similarly charged analytes could be separated based on size and vice versa. The method was expanded with the analysis of DNA as the analyte. DNA was chosen because of the interest in new, faster, single molecule sequencing methods and also to prove the method, since the nucleotide bases all carry similar charge, are similar sizes, and are closely packed in the DNA chain. By increasing the dynamic range of the sensor output and linking the DNA input to the digitized output using a hidden Markov model approach, we were able to produce very high single molecule accuracy. The high level of customizability for the basecaller algorithm coupled with the high accuracy of the resulting sequences indicates that there is still much work to be done in improving the method and tuning the device to specific applications.

7.2 <u>Numerical Model of the Electrical Double Layer in a Nanopore</u>

Our numerical model of the electrical double layer in a nanopore was developed in a continuum modeling software package (COMSOL 4.2a). The primary considerations that differentiated this model from previous studies are the consideration of the work function potentials of the solution and materials, and the consideration of the compact layer. These two considerations served to bring our understanding of the behavior of electrolyte solution within the nanopore into alignment standard electrochemical theory.

By considering the work function potential, we are able to relate the structure of the electrical double layer to the material properties of the nanopore. A surface potential controlled double layer is significant in that previous studies of nanopores considered the source of the double layer to be charge trapped on the nanopore surface. The source of the charge was considered to be deposited during fabrication or due to unintended functionalization. This explanation is insufficient, as there is little actual evidence that such charging occurs and such charge would not necessarily explain the material dependence of the double layer effects. A surface potential explanation also brings the study of the electrical double layer in a nanopore into alignment with more classical studies of the electrical double layer, where the structure is considered at the interface of a biased electrode in solution. The electrode solution interface is a key structure in this project, since we are interested in both manipulation and detection of the electrical double layer.

In this model of the electrical double layer in a nanopore, we assumed the compact layer could be modelled as a cylindrical shell at the surface of the nanopore. This is significant in that the volume of the compact layer occludes a portion of the nanopore, effectively reducing the hydrodynamic diameter and concentrating the diffuse layer in the center of the nanopore. We made simplifying assumptions about the compact layer, namely, that the shape of the compact layer is a cylindrical shell. This is clearly an approximation, since at the molecular level (which the scale of this model approaches), the compact layer consists of ions and solvent molecules packed at the surface. This packed compact layer would have sub-nanometer variations on the surface as the packing would be imperfect and stochastically vary with position. Further, we found that the thickness of the compact layer is related to the electrolyte concentration, indicating that the compact layer varies between a sparse adsorbed layer and a packed multilayer. So likely the sub-nanometer surface roughness will vary along with the compact layer thickness. However, we were able to explain most of the observable effects of the double layer on the conductance through a nanopore by considering the thickness of the compact layer alone, with no consideration of surface roughness. We further justify this simplification by the several studies available of electrolyte conductance through our model system (single-walled carbon nanotubes) which indicates that the flow is essentially frictionless. By considering a compact layer with variable thickness which is controlled by the electrolyte concentration, we demonstrated a new model of the solution and interactions within the nanopore which is consistent with studies of the electrical double layer and experimental observation of nanopore behavior. Characterisation of the

electrical and solution contributions to EDL structure and behavior allowed us to consider direct manipulation of the EDL for electrofluidic control by externally manipulating the conditions of the nanopore.

7.3 <u>Electrical Double Layer Manipulation</u>

We manipulated the electrical double layer in a metallic nanopore by applying an electrical potential to the surface of the nanopore. Experimentally, we observed gating and linear amplification of the ionic conductance through the nanopore depending on the polarity and magnitude of the applied bias. By adapting our numerical model of the electrical double layer to the geometry, materials, and electrical conditions of our experiment, we were able to describe the changes to the double layer that were responsible for the observed conductance effects. Primary findings of this study were that it is possible to generate spatially varying charge distributions in the fluid within the nanopore and changes to the surface potential of the nanopore result in reorganization of the charge and structure of the diffuse layer in the electrical double layer. Crucially, this work demonstrated a controlled interaction between the charge of the diffuse layer and the nanopore surface potential. The relationships tend to be well defined in that the on-state ionic conductance through the nanopore and the number of charges in the nanopore are both linearly related to the surface potential. This relationship defines a charge/potential balance that is critical to activating the nanopore as a molecular sensor (as was discussed in Chapter 5 and Chapter 6).

Manipulation of the electrical double layer was critical in developing our model and understanding of the relationship between the electrical conditions of the nanopore and the fluid within the nanopore. As a standalone device, the gating nanopore is interesting in that the on-state conductance is linearly related to the gating potential. In order to apply the device as liquid-state logic devices, a method is needed to link the ionic current through the nanopore to the gating potential of a second nanopore transistor. Such an arrangement could be useful for liquid-state computation, which could potentially be useful to link chemical inputs to electronic sensors, bridging the gap between traditional computation and molecular signalling. A liquid-state computation device could be useful to detect certain analytes and transport individual molecules into specified channels, cascading into complex electrical responses due to molecular inputs, similar to a biological endocrine system.

7.4 Electrical Double Layer Detection

Based on our observation of the balance between the charge in the electrical double layer and the applied surface potential, it seemed likely that the process could be inverted. In order to allow the double layer to control the surface potential, it was necessary to allow the surface potential to stay in equilibrium with the energetic potential of the electrical double layer. A small electrical current was supplied to the metallic layer of the nanopore and the potential was allowed to reach equilibrium. Initial confirmation that the electrode was in equilibrium with the solution was obtained by observing that the steady-state potential measured at the electrode was logarithmically related to the concentration

of the supporting electrolyte. A logarithmic relationship with concentration is typical for the activity and electrochemical potential of a solution. In seeking to describe the solution/electrode balance, it was helpful to return to the original work on the electrochemical potential of aqueous electrolyte solution by Huckel and Debye. [5] Their analytical description of the relationship between the charge, size, and permittivity of constituent ions with the electrochemical potential of solutions was similar to our experimental observations, particularly the logarithmic relationship between concentration and potential. Further, by expanding our numerical model of the nanopore and electrical double layer to account for the charging behavior of the metallic electrode, we were able to relate the measured potential to the charge and size of the constituent ions within the nanopore. Particularly, we were able to like the charge and size of small molecular analytes (which were different from the supporting electrolytes and much more dilute) to the change in measured potential that was observed during a translocation event. In essence, the transient presence of an analyte molecule will change the electrochemical potential of the solution within the nanopore due to the contribution of the size and charge of the analyte. The change in electrochemical potential will be recorded as a corresponding change to the charging potential of the metallic nanopore electrode.

From this work, we were able to demonstrate the practicality of this method for molecular detection and identification. Through extensive modeling and analysis we were able to determine the underlying physical principles and reduce the source of the signal to fundamental concepts, chiefly the balance between the electrochemical potential of the

solution and the charged metallic nanopore. While this relationship is well characterized in terms of source and mechanics, there is still much to do to probe the limits of this method. One of the primary goals of this project is the development of a nanopore DNA sequencer, and application of this method to that end is discussed in Chapter 6. However, there are other applications for this technology that have yet to be explored. In the characterization work for this electrical double layer method, small molecular analytes were examined, however identification of mixed analyte solutions has great interest in several fields, including pharmaceutics, metabolomics, and chemical testing. Additionally, the steady-state relationship between solution and potential suggests that this sort of sensor has applications in pH detection and solution characterization. Clearly, much development is needed in order to fully explore the impact of this device.

7.5 <u>DNA Sequencing</u>

The EDL detection method was explored by considering DNA as the analyte of interest. DNA offers unique challenges in that the nucleotide bases carry similar charge and have similar size. Additionally, the nucleotides are closely spaced along the DNA strand, imposing a longitudinal resolution limit. A further motivation for pursuing this application is the emerging market for fast, cheap DNA sequencing which is estimated to reach several billions of dollars in the next few years. The problem of DNA sequencing in a nanopore is to map the sensor output to the DNA input in a reliable and error tolerant way. This is complicated by the relatively high noise of sub-molecular measurements, meaning that each nucleotide may produce a range of sensor outputs. Because the

nucleotides are similar in size and charge, we expect that the sensor outputs of different nucleotides will be fairly similar. From the acquisition side, it is uncertain that the source of the signal is individual nucleotides, and it is likely that the source is a multi-nucleotide region. In order to map the inputs to the outputs, we employ a machine learning method to define a hidden Markov model with consideration of various input nucleotide resolutions and output resolutions. Considering various input resolutions allowed us to account for the multi-nucleotide resolution of the nanopore sensor, since it was unlikely that the detection was truly of a single nucleotide. What we found was that the ionic current was likely due to 2-nucleotide stretches while the double layer potential signal appears to have 1-nucleotide resolution. By varying the output resolution, which is in effect changing the step size in our quantization of the signals, we consider smaller differences between the collected signals. Our belief was that eventually the step size would fall below the noise level of the signal and we would lose discrimination. However, even at the highest resolution considered (at the nanovolt and femtoamp range), we showed continually increasing accuracy. Since we were not limited by the resolution of the measurements, we were eventually limited by the computational resources required to train hidden Markov models with the high resolution signals. At the highest resolution considered, there were over 4 billion digitization levels (4^{7+9}), which was too many data points to handle, even on the Palmetto cluster with 550 GB of memory. From this there is a clear trade-off between computational load and accuracy. It was observed that high single molecule accuracy could be attained by sequencing with a very high resolution double layer potential signal, but at the cost of high computational

180

load. A high average accuracy could be attained by using combined measurements of the ionic current and double layer potential signals with resolutions near the middle of the range considered. This nanopore sequencing method is then highly tuneable and customizable for specific applications.

Future work with this method will include improving the computational efficiency of the algorithm and exploring specific applications. Areas where this technology could be applied include sequencing long reads, whole genomes, epigenomes, and sequences that are difficult to parse using contemporary technology.

APPENDICES

PROCESS FLOW FOR METALLIC NANOPORE FABRICATION

Introduction:

      To fabricate a <10 nm diameter pore in a suspended membrane. The critical dimension is the diameter of the nanopore. The suspended membrane should be multilayered with a supporting layer, a minimally thin conductive metal layer, and a passivation layer. The minimum diameter of the nanopore should occur within the metal layer. The device will be used for molecular sensing applications.

Project Description:

Substrate material	silicon wafer
Substrate size	4" wafer
Supporting membrane material	Silicon Nitride (low stress layer)
Supporting membrane size	50 nm (thickness), area = 50 x 50 um
Adhesion layer material	Ti or AlO_2
Adhesion layer thickness	5 nm
Metal layer material	Au or Pt
Metal layer thickness	10 nm
Device Type	MEMS
Critical dimension	<10 nm (pore diameter)
Die size	4 mm x 4 mm

Process Flow Diagram (process modified from doctoral thesis of Amir Ahmadi, Georgia Tech, May 2013)

Final product:

Silicon Nitride Window
With Nanopore

Gold Contact Pad

Silicon Base

Zhang Lab
Clemson University

PR
Ti
Au
SiN
Si
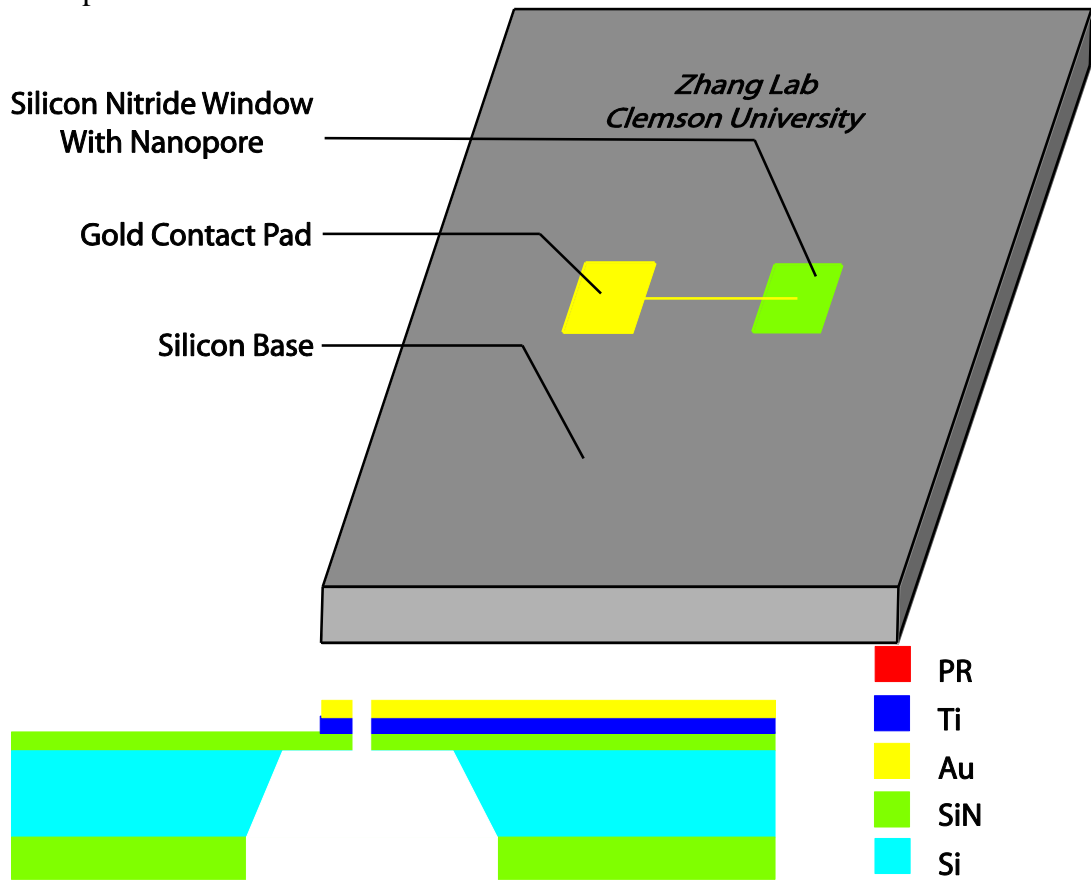
Mask designs:
1. Pt. electrode lift-off mask
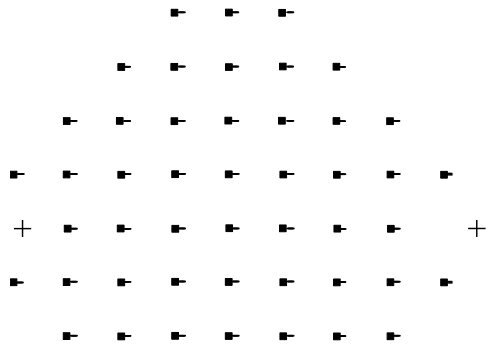
    a.
2. Pt contact pad/oxide lift-off mask
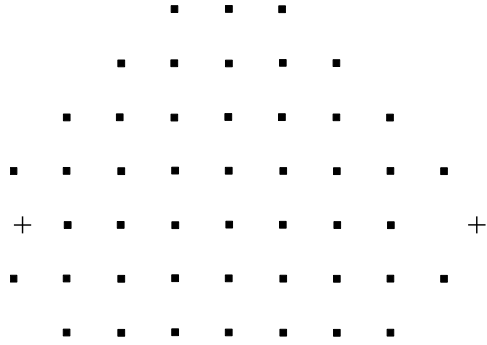
    a.
3. Backside SiN etch mask (775 um, for EBL design)
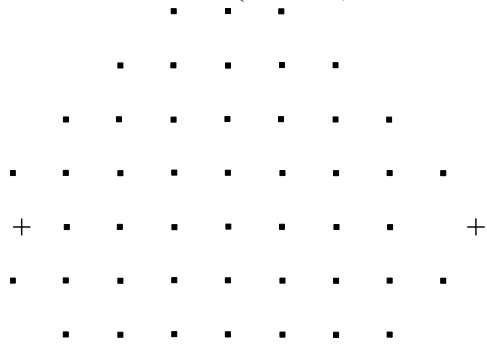
    a.
4. Backside SiN etch mask (333 um, for TEM design)

a.

5. EBL mask design (for EBL alignment)
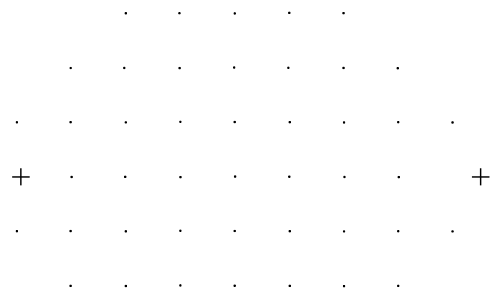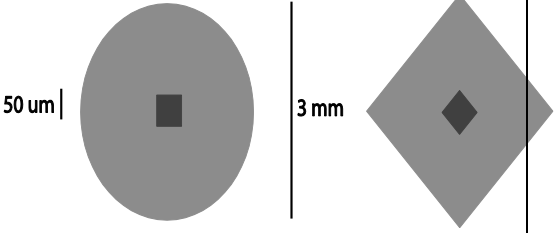
a.

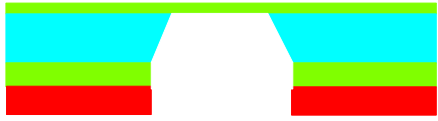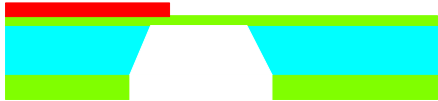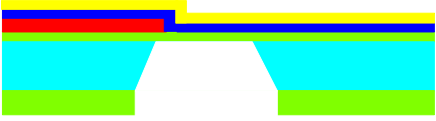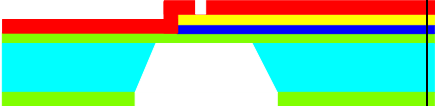| TEM process	EBL process	Legend

1. Clean double sided, 200 um thick, silicon wafer
  a. Purpose: To prepare the wafer for Silicon Nitride deposition
  b. Equipment: CMOS cleaning station
  c. Time Estimate: 30 min
Clean double sided silicon wafer
	1. Clean double sided silicon wafer
	  a. Purpose: To prepare the wafer for Silicon Nitride deposition
	  b. Equipment: CMOS cleaning station
	  c. Time Estimate: 30 min
	Clean double sided silicon wafer
		▉ PR
		▉ Ti
		▉ Au
		▉ SiN
		▉ Si

2. Deposit 50 nm LPCVD Silicon Nitride on wafer
  a. Purpose: To serve as the supporting layer of a suspended membrane
  b. Equipment: LPCVD furnace (Tystar Nitride 4)
  c. Time Estimate:
    1. Total time: 4-5 hrs
  d. Use a low stress tension recipe
Deposit LPCVD Silicon Nitride
		▉ PR
		▉ Ti
		▉ Au
		▉ SiN
		▉ Si

3. Deposit 200 nm Silicon Nitride on backside of wafer
  a. Purpose: To serve as a masking layer in step 6
  b. Equipment: PECVD (Oxford PECVD right)
  c. Time Estimate:
    1. (2000 A)/(170.91 A/min) = 11.70 min
    2. Rotate wafer 90 degrees halfway through deposition, or the backside etch (step 6) will destroy this layer
Deposit 200 nm Silicon Nitride on backside of wafer
		▉ PR
		▉ Ti
		▉ Au
		▉ SiN
		▉ Si

187
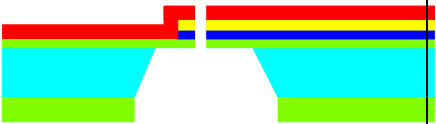
4. Deposit PR for backside etch 　　a. Purpose: To pattern SiN layer mask to release suspended membranes 　　b. Equipment: Spinner, mask aligner, wet bench 　　c. Time Estimate: 　　　　1. Spinner: 10 min 　　　　2. Mask aligner: 30 min 　　　　3. PR: negative resist (Futurrex NR9-1500PY) 　　　　4. Speed: 3000 rpm, 40 s for 1.5 um 　　　　5. 150C for 60s (softbake) 　　　　6. Exposure:　190 mJ/cm2 / um @ 365 nm 　　　　7. 100C for 60s (hardbake) 　　　　8. Resist developer RD6 　　　　9. Remove with acetone 　　d. Mask 3 or 4 (if EBL or TEM), tone ok **Deposit backside PR**	■ PR ■ Ti ■ Au ■ SiN ■ Si
5. Etch openings in backside Silicon Nitride 　　a. Purpose: To be used as a mask for etching of Silicon in step 9 　　b. Equipment: Vision RIE 2 　　c. Time Estimate: 　　　　1. 5-10 min, check with microscope **Etch backside SiN**	■ PR ■ Ti ■ Au ■ SiN ■ Si
6. Etch underlying Silicon masked by backside Silicon Nitride 　　a. Purpose: To open the window and create a suspended membrane 　　b. Equipment: wet bench, KOH etchant 　　　　1. 45% KOH 85C 　　　　2. Remove wafer from holder while submerged to prevent 　　　　　breakage 　　c. Time Estimate: 　　　　1. 8 hrs for standard 400 um wafer 　　　　2. 3-4 hrs for thin 200 um wafer	■ PR ■ Ti ■ Au ■ SiN ■ Si

Etch backside Si	

7. Deposit PR for lift off of Ti/Au for 10-1000 micron scale electrode, wire, contact pad
   a. Purpose: To pattern metal region around nanopore, contact pad, and connection between nanopore and contact pad
   b. Equipment: Spinner, mask aligner, wet bench
      1. PR: negative resist (Futurrex NR9-1500PY)
      2. Speed: 3000 rpm, 40 s for 1.5 um
      3. 150C for 60s (softbake)
      4. Exposure: 190 mJ/cm2 / um @ 365 nm
      5. 100C for 60s (hardbake)
      6. Resist developer RD6
      7. Remove with acetone
   c. Time Estimate:
      1. Spinner: 10 min
      2. Mask aligner: 30 min, use backside alignment
   d. Mask #1 with backside alignment
   e. Remove a screw from the backside alignment chuck, this will reduce the vacuum holding the wafer to the chuck and prevent membrane rupture.
   Deposit PR for lift off
	PR
	Ti
	Au
	SiN
	Si

8. Deposit Ti/Au on the masked membrane
   a. Purpose: To form metallic layer
   b. Equipment: Denton Explorer - E-beam Evaporator – Ti/Au
   c. Time Estimate: 5,10, and 20 nm at 0.5 nm/s, 2 hr pumpdown
      1. Total time: 120 min
   d. Ti and Au can be deposited in sequential steps without breaking vacuum
	PR
	Ti
	Au
	SiN
	Si

Deposit Ti/Au	

9. Lift off Ti/Au layer
    a. Purpose: To pattern electrode layer
    b. Equipment: wet bench, acetone
    c. Time Estimate: 10 min
    d. Inspect with optical microscope
Lift-off Ti/Au
 	
	■ PR
	■ Ti
	■ Au
	■ SiN
	■ Si

10. Dice the wafer to fit the TEM holder
    d. Purpose: To create pieces for nanopore formation
    e. Equipment: diamond scriber
    f. Time Estimate:
       1. User dependent
Dice wafer
 	
	10. Deposit Zeon ZEP-520 positive resist on thin Silicon Nitride/oxide/platinum layer
	    a. Purpose: To form masking layer for 10 nm pore formation in suspended membrane
	    b. Equipment: EBL spin coater
	    c. Time Estimate:
	       1. 10 min
	Deposit EBL resist
	
		■ PR
		■ Ti
		■ Au
		■ SiN
		■ Si

11. Form nanopore with IPST FEG-TEM
    a. Purpose: To form high aspect ratio (>20) nanopores with diameters <10 nm
    b. Equipment: FEG-TEM (not IEN equipment,
	11. Pattern Zeon ZEP-520 positive resist on thin Silicon Nitride/oxide/platinum layer with electron beam lithography
	    a. Purpose: To form masking layer for 10 nm pore formation in
		■ PR
		■ Ti
		■ Au
		■ SiN
		■ Si

located and billed to the GT IPST) c. Time Estimate: actual exposure is fast (<5 min), setup time depends on how long it takes the sample to reach thermal equilibrium (45-60 min). **Form nanopore with FEG-TEM**	Silicon Nitride/ Ti/Au membrane b. Equipment: Jeol EBL c. Time Estimate: actual patterning should be fast (minutes), setup time depends on number of devices and alignment d. Mask # 5 **Pattern EBL resist**	

	12. Etch thin Nitride/Ti/Au membrane
	  a. Purpose: To produce 10 nm nanopores in Silicon Nitride/Ti/Au membrane
	  b. Equipment: Oxford Cryogenic ICP
	For SiN/Ti/Au devices:
	  a. Coil power: 2600 W
	  b. Platen power: 45 W
	  c. Pressure: 5 mT
	  d. Temperature: 10 C
	  e. CHF_3: 20 sccm
	  f. O_2: 5 sccm
	  g. Ar: 30 sccm
	  h. Time: 60 s
	For SiN/AlO$_2$/Pt devices:
	  a. Coil power: 2600 W
	  b. Platen power: 45 W
	  c. Pressure: 5 mT
	  d. Temperature: 10 C
	  e. CHF_3: 20 sccm
	  f. O_2: 5 sccm
	  g. Ar: 30 sccm
	  h. Cl_2: 10 sccm
	  i. Time: 60 s
		■ PR
		■ Ti
		■ Au
		■ SiN
		■ Si

	Etch nanopore	

	13. Remove resist
	    a. Purpose: To finish device
	    b. Equipment: wet bench
	    c. Time Estimate: 10 min
	
	Remove resist
	
		PR
		Ti
		Au
		SiN
		Si

Appendix B

NANOPORE DEVICE FABRICATION

Nanopore fabrication is a technically challenging problem with due to the very small dimensions of the structures involved. Typically, a suspended membrane is prepared and the nanopore is formed in the membrane. Membrane materials may be dielectric, semiconductor, metallic, or some single-molecule sheet (such as graphene or molybdenum disulfide). The limiting property of the suspended membrane is that it must be strong enough to support itself in a fluidic environment and withstand whatever forces are applied during device operation. Additionally, the membrane must be impermeable, else there would exist alternative conduction channels competing with the nanopore. Because strength of the membrane is a primary concern, Silicon Nitride (SiN) is often used, where low pressure chemical vapor deposition (LPCVD) produces the highest quality SiN membranes. In this research project, membranes consisted of LPCVD SiN with a metallic (Ti/Au) electrode deposited over the membrane. The nanopore was formed through the electrode and membrane using a variety of methods.

Nanopores have been fabricated with a number of approaches, including embedding nanotubes in a dielectric medium, heavy ion track etching, wet etch, dry etch, focused ion beam (FIB), and electron beam (e-beam) sculpting. The fabrication method depends on the material of the nanopore as well as the desired shape and size. For example, embedding nanotubes in a dielectric medium can produce nanochannels with very high aspect ratios. Etching along a heavy ion track can produce conical nanopores with very large taper angles, but the method is limited primarily to polymer substrates. In this

193

research project, nanopores were formed in the SiN/Ti/Au membrane with three different methods: FIB, inductively coupled plasma (ICP) etching, and e-beam sculpting.

Focused ion beam was used to produce the first generation of nanopore devices (Figure B.1). Membranes and electrodes were prepared and nanopores were formed with focussed ion beam. The membranes in this case were produced at Cornell's nanofabrication facility and were approximately 5 microns thick with a 100 nm gold layer and a lateral area of 700x700 μm. Because of the large surface area of these membranes, they were prone to breakage. The FIB method consists of bombarding the membrane with Gallium ions in order to sputter away material in the region of the nanopore. Nanopores prepared in this way were found to range between $100 - 200$ nm in diameter. Since the diameter of these nanopores was so large, they failed to display any fluidic effects associated with the electrical double layer. In order to produce double layer effects, the gold layer of these nanopores was electroplated, essentially filling in the volume of the nanopore with gold. Electroplating was an iterative process that often took several hours to produce a nanopore with <20 nS conductance in 100 mM KCl (where this conductance is a typical maximum value to observe double layer effects). Because of the crude nature of these first generation nanopore devices, the membrane often ruptured and it was rare to obtain a device with good characteristics. However, good devices were eventually produced and used in the nanopore gating study (Chapter 4).
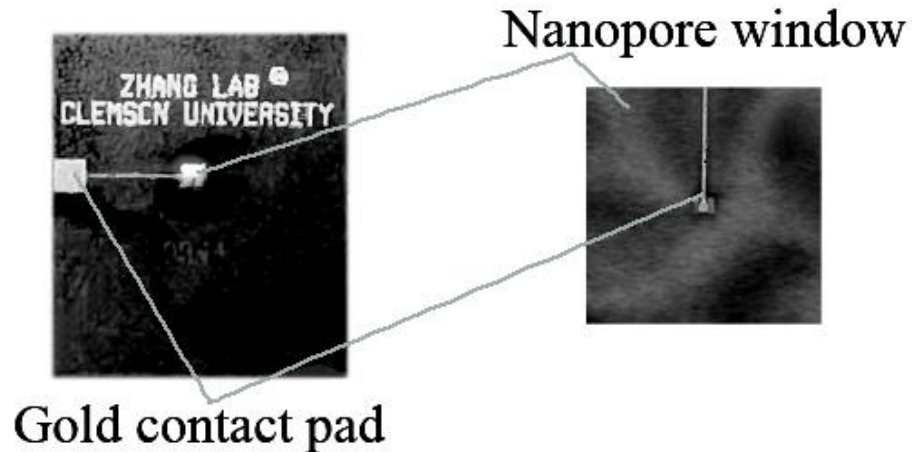
Figure B.1. 1st generation nanopore device. The nanopore was formed in the nanopore window with a combination of FIB and electroplating.

The second generation of nanopore devices was produced at the Georgia Institute of Technologies nanofabrication facility. The membrane consisted of a 50 nm thick LPCVD SiN membrane with a 5 nm Ti and 10 nm Au electrode (Figure B. 2). The lateral area of the suspended membrane was 50x50 μm. Because the surface area was much smaller and the ratio of thickness to area was much greater in this second generation compared to the first, breakage of the membrane was rarely observed. Nanopores were formed by first patterning resist with an electron beam lithography system (JEOL JBX-9300FS EBL System), then etching the membrane with either an ICP etch system (Oxford Cryogenic ICP) or reactive ion etch (RIE) system (Vision 320 RIE). The e-beam resist used was a

195

350 nm thick layer of ZEP 520a, which was spun onto the membrane substrate at 4000 rpm for 60 s. The nanopore itself was patterned as a 10 nm disk at doses of 1100 $\mu C / cm^2$ to 33000 $\mu C / cm^2$, where the best results typically were produced between 1100 and 10000 $\mu C / cm^2$. The patterned devices were transferred to a dry etch chamber and etched with the appropriate recipe (see appendix for recipes). The conductance in 100 mM NaF solution of nanopores produced by this method typically fell in the range of 2-20 nS, where the devices chosen for further evaluation were from the 2 nS devices. Imaging and fluidic analysis of 3rd generation devices indicates that a 2 nS conductance correlates to a nanopore with a 10 nm diameter. This 2nd generation of devices was used in molecular sensing applications (Chapter 5 and Chapter 6).
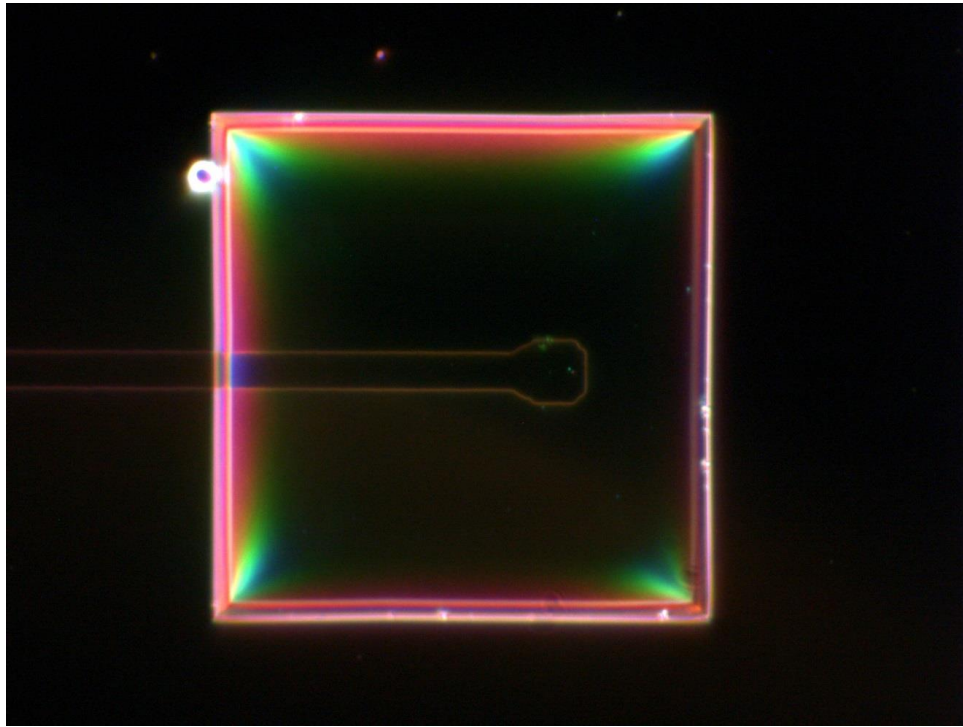
Figure B. 2. Darkfield image of the 2nd generation nanopore. The location of the

nanopore on the electrode is visible as a faint blue spot near the center-right of the

electrode.

The third generation of devices were developed on the membranes with the same

dimensions and materials as the second generation devices. However the nanopore itself

was formed in a single step by exposing the device to a tightly focused, high powered

electron beam in a transmission electron microscope equipped with a field emission gun.

The benefit of using this method is that the nanopore may be imaged immediately after

formation (Figure B. 3). The method to produce this nanopore on this particular machine

was to load the sample and allow 45-60 minutes for thermal equilibration, as any thermal

contraction results in sample movement and deformation of the nanopore. Once the

sample has stabilized, the TEM is placed in 'nanoprobe' mode to produce the smallest beam width and manually focused on the center of the membrane. The screen current will gradually increase to saturation, at which point the nanopore is through-etched. These nanopores have thus far only been evaluated in preliminary tests. Typical conductance in 100 mM NaF is 2-4 nS, which is similar to the 2nd generation nanopores.

a.
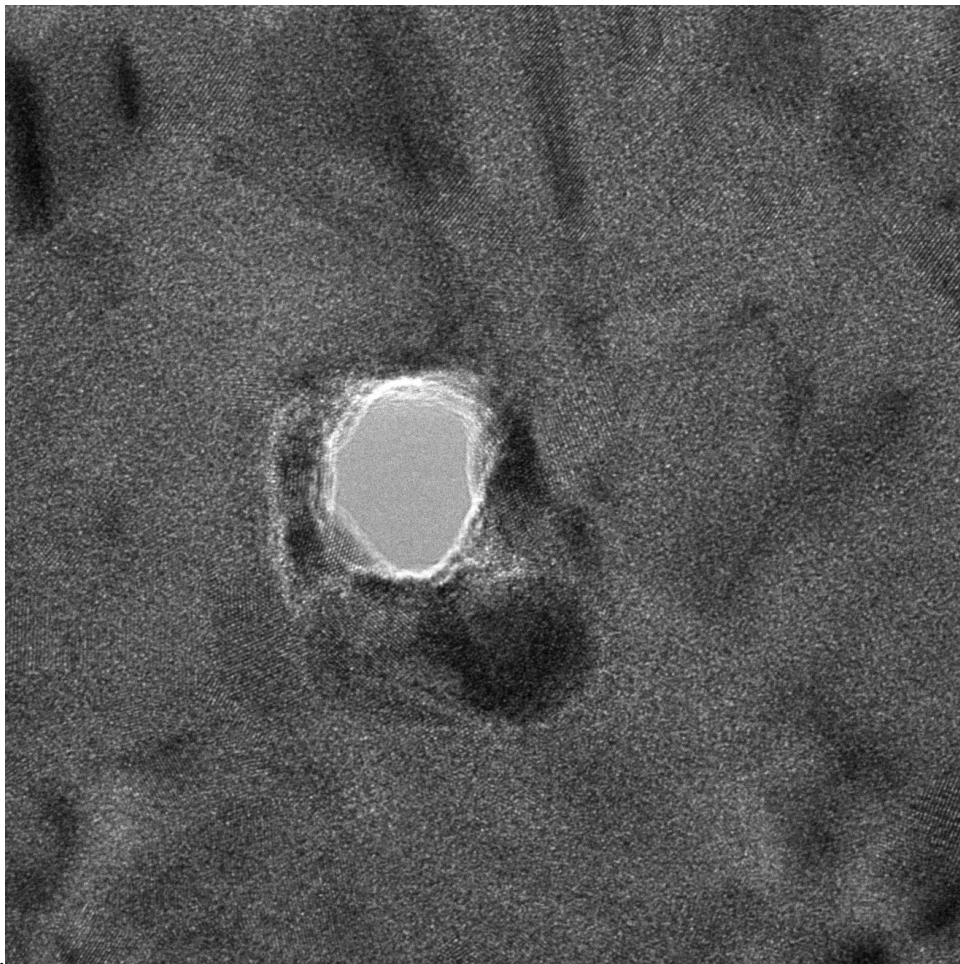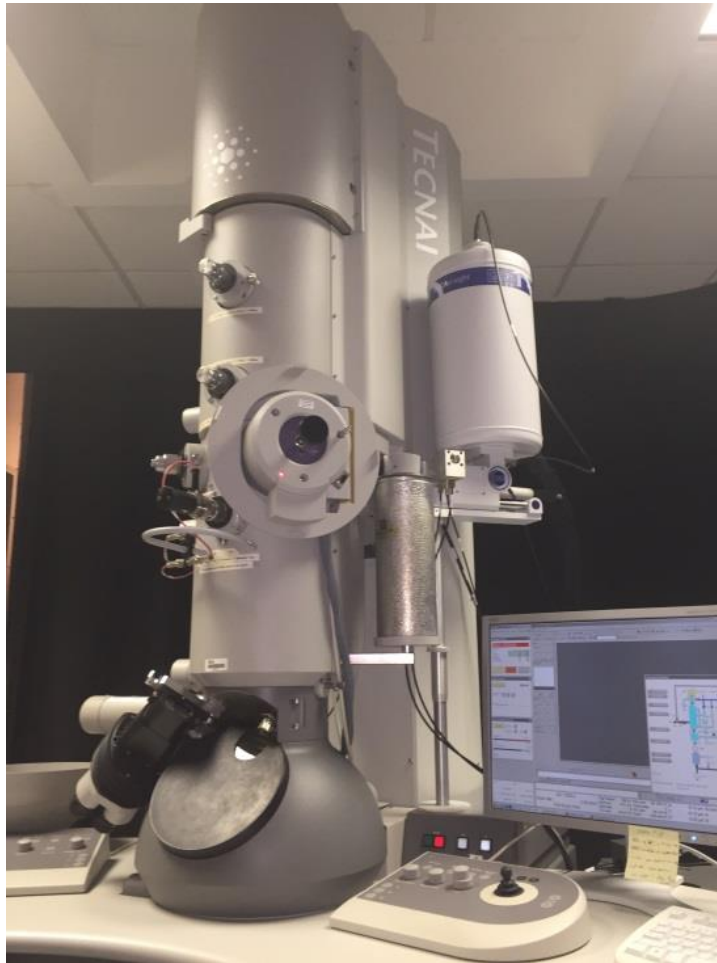
b.

Figure B. 3. a. High resolution TEM image a 3rd generation nanopore. The diameter is 10 nm with a circular shape. At this scale, the gold atoms are visible surrounding the nanopore. b. The FEG-TEM used to form and image the 3rd generation nanopores.

Membrane fabrication:

The second and third generation nanopore devices share a common fabrication process up until formation of the nanopore. An overview of the step by step fabrication method is available in Appendix A. Additional details are provided in this section.

1. Cleaning

Select the appropriate wafer for the desired nanopore formation technique. If e-beam lithography is to be used, a standard thickness (100) oriented wafers may be used. If the nanopores are to be formed in a high energy transmission electron microscope (TEM), then the wafers used must be <250 μm thick in order to fit in the TEM sample holder. Cleaning the wafers consists of piranha cleaning followed by HF dip. Use the CMOS cleaning station, turn on power and set the temperature to 120 C for the Piranha bath. While the bath is heating (~15 min), add 100 ml of H_2O_2 to the bath.

Once temperature has been reached, load the wafers in a boat and insert into the bath for 10 minutes. Use the timer built in to the CMOS cleaning station. After time is up, transfer the wafers in the boat to the dump rinse and press start, allow the dump rinse to cycle 5 times. Transfer the wafers and boat to the HF bath for 1 minute. Use the timer built in to the CMOS cleaning station. Transfer the boat and wafers to the dump rinse for 5 cycles. Transfer the wafers and boat to the CMOS spin rinse dryer, boat H-bar goes to the back. Press the green button to start. When the spin rinse cycle is done, the wafers are clean and dried.

2. Deposit LPCVD SiN

LPCVD SiN is deposited in the LPCVD furnace (Tystar Nitride furnace 4) located in the Petit cleanroom. Log in to the equipment and run the 'open' program in the interface. Identical controls are located in hardware buttons on the furnace and on the touchscreen LCD screen. Some buttons work on one interface but not the other, so if pushing a button has no effect, try pushing the corresponding button on the other interface. Once the furnace caddy is open, load the wafers on the metal boat on the furnace rails (all

components that go into the furnace are very hot). Use the plastic vacuum wafer paddle to transfer wafers, it is important that no metal tweezers are used in the context of the furnace to avoid contamination. After the wafers are loaded into the boat, activate the 'load' command to close the furnace. While the furnace is closing, set up the deposition program. For this application use the recipe 'LSNITRID50', and set the deposition time. The deposition rate is 3.46 nm/min, so use a deposition time of 15 minutes for a 50 nm layer. The LPCVD deposition deposits SiN on both sides of the wafer and should look blue-green. If the layer is red, then the deposition is of very poor quality and is unsuitable for this application.

3. Backside SiN deposition

In order to fully mask the backside of the wafer for backside deposition, it is necessary to add more SiN to one side of the wafer. Use the Oxford PECVD right tool to deposit 200 nm of PECVD SiN on the side of the wafer chosen to be the back of the device. From this point on it is necessary to maintain the front/back orientation of the wafer. PECVD SiN tends to be poor quality and will tend to be etched by KOH wet etch baths. However, this is due to the presence of pinhole defects throughout the layer. These pinhole defects may be avoided in thick layers by rotating the wafer halfway through deposition. So for this step, load the wafer on the tool with the backside oriented up, close the tool and run the SiN deposition recipe. Run the deposition for 5:51 min:ss (100 nm, 170.91 A/min deposition rate), open the chamber, rotate the wafer 90 degrees, close

the chamber and deposit for an additional 5:51 min:ss. This 200 nm thick layer will be impermeable to the KOH etch.

4. Photoresist deposit and pattern

There are several photoresist steps in this fabrication process. With the exception of the EBL resist deposition (which is done on the EBL spin coater in Petit cleanroom and uses ZEP 520a resist), all photoresist deposition and patterning follows the same procedure. Briefly, photoresist is spun onto the wafer and softbaked, the photoresist is patterned on a Karl-Suss mask aligner, hardbaked, and developed. In every deposition step, use photoresist Futurrex NR9-1500PY, spun at 3000 rpm for 40 s to produce a 1.5 μm layer. Softbake at 150C for 60 s. Align the wafer on a Karl-Suss mask aligner with the appropriate mask for the step (see Appendix A for the mask design and use). It is important to determine the power of the Karl-Suss mask aligner lamp, so check that the lamp is set to 365 nm wavelength (channel A on the lamp power supply). Measure power output by placing the detector (located in a suitcase under the aligner) on the platen and pressing 'lamp test'. Calculate the exposure time by dividing the required dose (190 mJ/cm^2/ μm at 1.5 μm thickness) by the measured power (mW/cm^2)/(mW/cm^2) = time in s. Reduce the calculated time by 2 seconds, as the mask aligner tends to overexpose the photoresist, which can destroy surface features <10 μm in size. After exposure, hardbake the resist at 100C for 60s. Develop the resist in RD6 developer for 30 s and examine the features under a microscope. If the features are unsatisfactorily developed, photoresist can be stripped with acetone and the process can be repeated.

5. Etch backside SiN for KOH mask

Place the wafer in the Vision RIE 2 with the patterned photoresist side up. Etch the SiN by running the SiO_2 etch recipe (same recipe works for SiO_2 and SiN) for 5 minutes. Check that the SiN was fully removed with a microscope. Additional etch time may be needed depending on wafer-to-wafer variation, but be sure to fully remove the SiN. It is acceptable and even desirable to overetch this step, so long as the etch does not extend through the wafer.
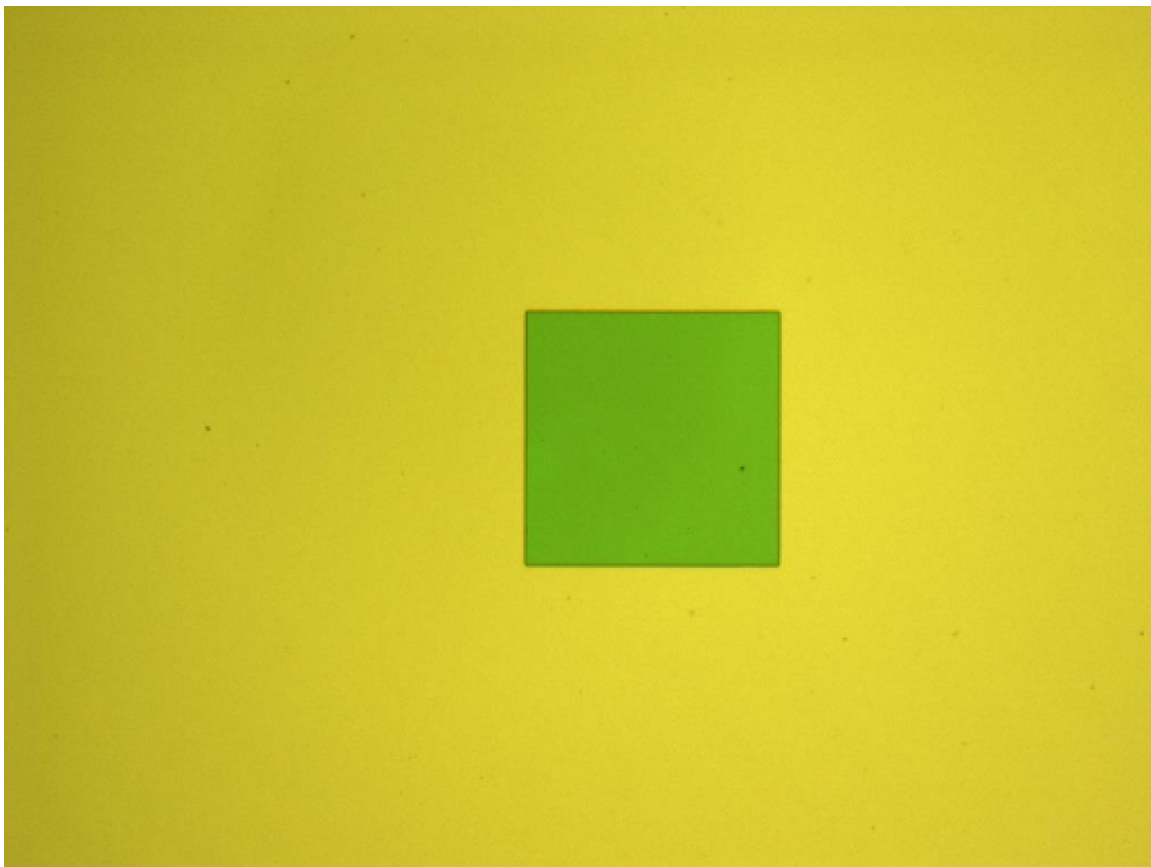
Figure B.4. Wafer backside after RIE etch. The yellow region is masked by PECVD and LPCVD SiN while the green square is the underlying silicon substrate. Colors will vary

depending on microscope settings, but to the naked eye the SiN layer should be blue-

green.

6.   Backside wet etch

The backside wet etch removes the underlying silicon to free the SiN membrane. The etch step may be completed on a hotplate in a wet bench or in the MEMS wet bench (in Petit cleanroom). The MEMS wet bench is more convenient for this sort of etch, but in development, the wafers were kept in Marcus cleanroom to avoid contamination if the wafers are transported between cleanrooms. In this etch step, the wafers are loaded in a wafer holder (typically kept in the Petit mask shop but can be moved to Marcus, check with Harley Hayden). The loaded wafer holder is kept in a bath of 45% KOH solution at 85C for 8 hrs (for a standard thickness wafer) or 4 hrs (for a thin wafer). It is important that the bath is well mixed for the duration of the etch in order to achieve a uniform etch rate across the wafer. KOH solution is provided by the cleanroom in gallon sized containers.
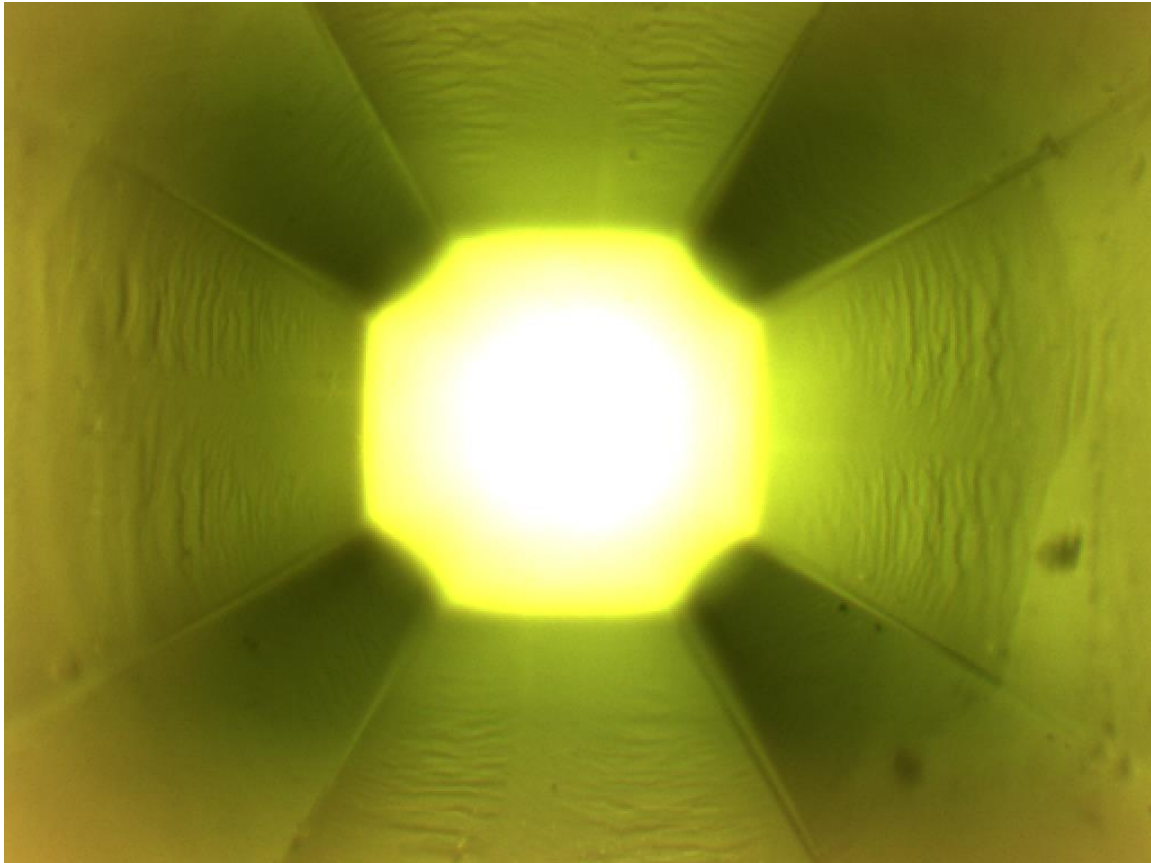
Figure B. 5. The backside of a suspended membrane after KOH through-etch. The angle of the walls (54.7°) is due to the crystal structure of the silicon substrate. After baskside etching, the low stress SiN membrane should be smooth and flat.

7. Deposit photoresist for metal lift off step

Repeat the instructions in step 4 for photoresist deposition and patterning of the topside electrodes. Care must be taken at this step to prevent breaking the membranes. For the spin step, attach the wafer to a carrier wafer (use tape), so that the spinner vacuum chuck does not break the membranes. For the alignment/exposure step, it is usually easier to align the electrodes to the membranes using backside alignment, rather than the standard

frontside alignment. On the backside alignment chuck, there is a small screw above the vacuum port (on the bottom of the chuck). Removal of this screw will reduce the vacuum pressure holding the wafer to the backside alignment chuck and prevent breakage (be careful to not lose the screw and be sure to replace it once alignment is complete).
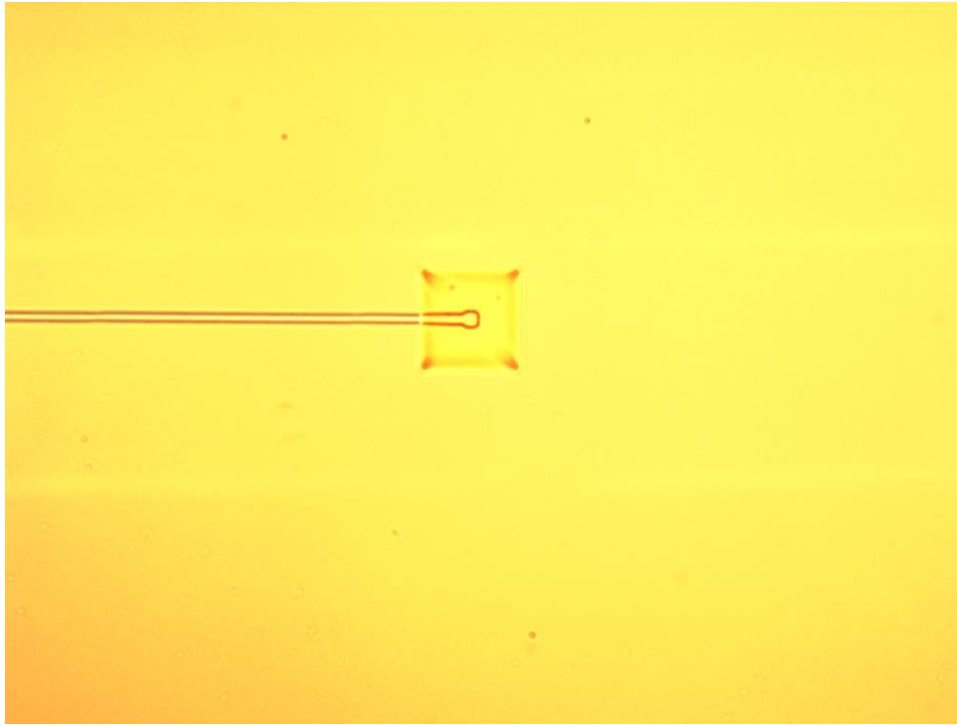
Figure B. 6. Photoresist patterned over the membranes before metallization. It is important to confirm that the electrodes will be centered over the membranes and that the features are present in good quality before metal is deposited.

8. Metallization

Metallization is done in the Denton Explorer e-beam evaporator. This tool is very heavily used, so it is important to schedule it as early as possible for at least a 2 hr time period. Once logged onto the tool, run 'Avent' to autovent the chamber. The door will

automatically open once atmospheric pressure is reached. For this project, deposition metals are titanium and gold. Titanium occupies a fixed crucible in the carousel, but check that there is enough material in the crucible before proceeding. The gold crucible must be exchanged with copper in the carousel holder (gold is not a standard carousel metal). When the process is complete, be sure to switch gold and copper back to the default positions. Load the wafers into the wafer carousel at the top of the chamber. Wafers will sit on top with the deposition surface facing down through the wafer carousel openings. Close the chamber door and run 'Apump' to begin pumping down the chamber. Allow the chamber to reach <2.5e-6 T before beginning deposition (about an hour). Set up the deposition programs while waiting.

Edit the deposition program for the desired metals (Ti/Au). In both cases the deposition rate should be between 0.1 and 0.5 nm/s. Titanium thickness should be 5 nm and gold thickness should be 10 nm. The deposition will tend to be less than the chosen thickness and the above settings should produce a 5 nm thick metal layer with good adhesion. Once pressure has been reached, deposit titanium, rotate the carousel, and deposit gold. Allow the metal crucibles to cool for 10 minutes before opening the chamber (opening too soon will cause oxidation of the metals and contaminate the next users samples). Run the 'Avent' program to vent the chamber and retrieve the metallized wafers. Exchange the crucibles and pumpdown the chamber before logging out of the tool.

9. Metal liftoff

Place the metallized wafers in an acetone bath to lift off the metal layer (leaving the electrode features). Most metal will liftoff immediately, but allow the wafer to soak for 15-20 minutes to fully remove any photoresist residue. Check the electrodes under a microscope, do not proceed if the electrodes and alignment marks are not fully developed. If no metal remains, the photoresist deposited in step 7 was overdeveloped and the wafer process can be restarted from that step (reduce exposure time by a 4 s from the calculated time). If the small features of the metal were removed, but some features remain, the metal may be removed by dipping the wafer in dilute aqua regia. However, this is dangerous and there is the risk that the wafer surface will be destroyed. Most problems at this stage may be prevented by being extremely careful in step 7.

a.

b.
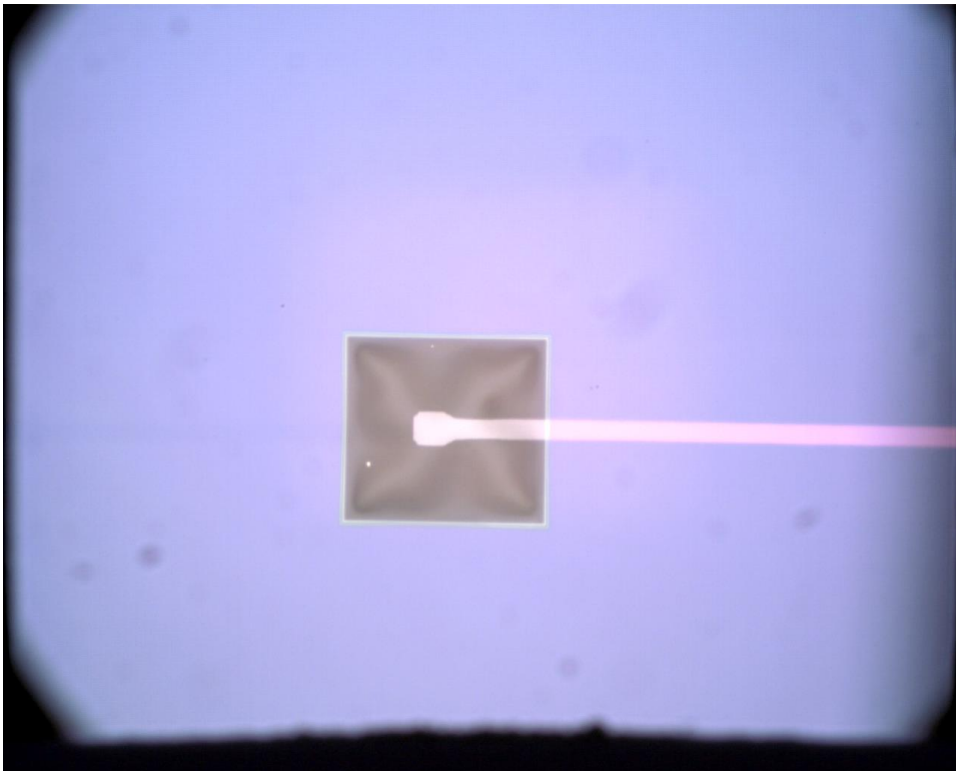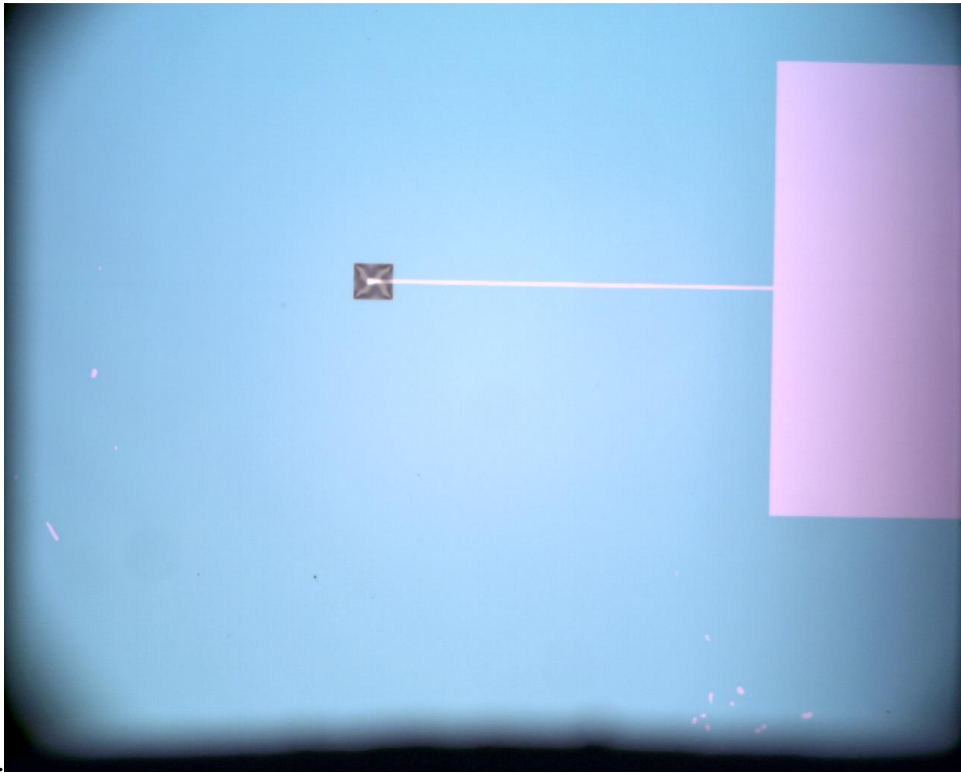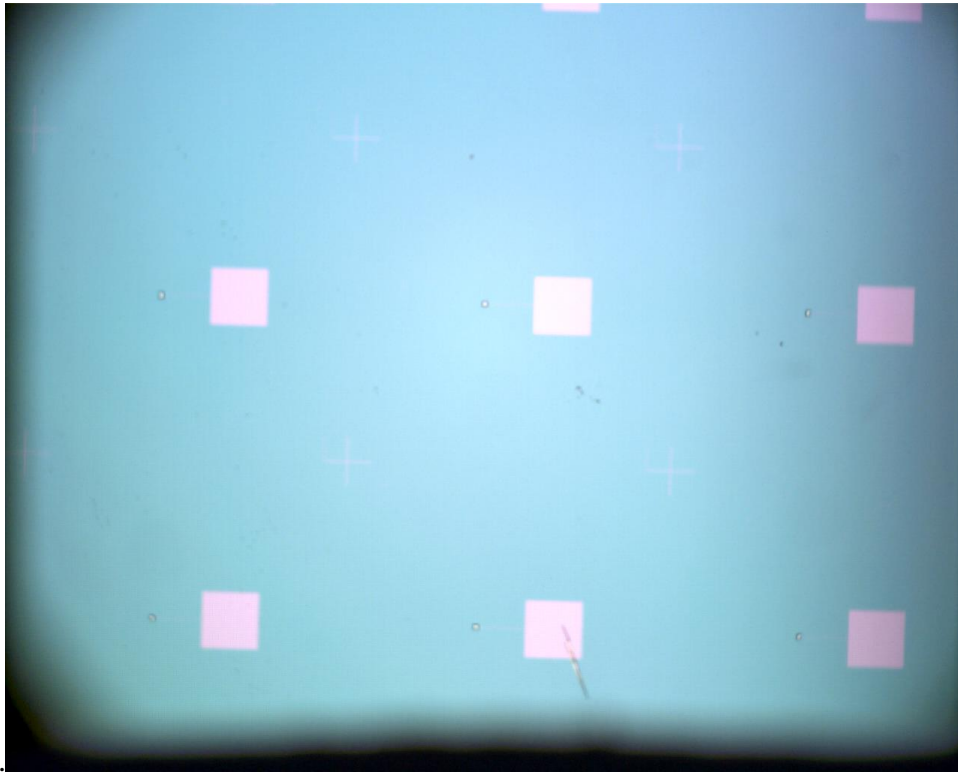
c.

Figure B.7. a. A 50x image of the Ti/Au electrode on the membrane after metallization and liftoff. b. A 10x image showing the membrane, electrode, and contact pad. c. A 2.5x image showing the spacing of devices on the wafer.

Electron beam lithography nanopore formation:

1. Program setup

E-beam lithography consists of three steps: preparation, exposure, and etching. Of these, preparation is the most difficult and will vary between samples. Preparation includes designing an exposure pattern in CAD software, writing execution files for the exposure, and preparing the physical sample to be loaded into the EBL system. In preparing the CAD files, software such as AutoCad are useful. The CAD file will contain

a 'unit cell', which is the pattern that will be tiled across the sample with location oriented relative to surface markers on the sample surface.

The execution files for the EBL system include the prepared CAD files, and a job deck file (.jdf) file and a schedule (.sdf) file. All three files are compiled into a magazine file (.mgn) which is readable by the JEOL JBX-9300FS EBL System. The job deck file references the CAD files and defines the tiling pattern in which the CAD files will be arranged. The job deck file also includes the electron beam dose (relative to a base dose defined in the scheduling file) to be applied to each pattern. The schedule file contains information regarding which wafer cassette is in use, parameters for the electron beam, global coordinates for the alignment marks, and the base electron beam dose. There are many commands and options which may be used in the job deck and schedule files which are not covered here. The full description of the JEOL EBL programming language may be found online, at the Georgia Tech nanolithography website (http://nanolithography.gatech.edu/index.html), or from JEOL. Included here are example job deck and scheduler files from this project, but certain details (such as the coordinates of alignment marks and the cassette to be used) will change run to run:

BNPALIGN.sdf:

```
MAGAZIN 'BNPALIGN'
#1
%3B
JDF 'BNPALIGN',1
ACC 100
CALPRM '100kv_2na'
DEFMODE 1 ;1_stage deflection
HSWITCH OFF,ON
RESIST 200 ; ZEP
SHOT A,100
GLMDET A
CHMDET A
CHIPAL 1
END 1
```

BNPALIGN.jdf:

```
JOB/W 'BNPALIGN',2

; 3B window center  = ( 200,000 , 60,000 )
; P actual position = ( 183,651 , 59,075 )
; P design position = ( 186,000 , 60,000 )
; P offset act-des  = (  -2,349 ,   -925 )
; P offset jdf/sdf  = (  -2,349 ,    925 )

GLMPOS P=(-14000,0), Q=(14000,0)
GLMP 3.0,2500.0
GLMQRS 3.0,2500.0

PATH DEVIN

; first mark at     (-14,000 ,      0 )
; pattern offset    ( +2,000 , +2,000 )
; first pattern     (-12,000 ,  2,000 )
; L chip design off ( +1,062 ,  1,059.15 )
; L chip jdf/sdf    (-10,938 ,  3,059.15 )
; L chip stage      ( 186,713, 56,016 )
; L chip actual     ( 186,723, 56,028 )
; L chip error      (    +10,    +12 )
; L chip error jdf  (    +10,    -12 )

  ARRAY ( -14500, 2, 200) / ( 2000, 10, 200)
      ASSIGN P(7)->((1,1),SHOT1)
      ASSIGN P(7)->((1,2),SHOT2)
      ASSIGN P(7)->((1,3),SHOT3)
      ASSIGN P(7)->((1,4),SHOT4)
      ASSIGN P(7)->((1,5),SHOT5)
      ASSIGN P(7)->((1,6),SHOT6)
      ASSIGN P(7)->((1,7),SHOT7)
      ASSIGN P(7)->((1,8),SHOT8)
      ASSIGN P(7)->((1,9),SHOT9)
      ASSIGN P(7)->((1,10),SHOT10)
      ASSIGN P(7)->((2,1),SHOT11)
      ASSIGN P(7)->((2,2),SHOT12)
      ASSIGN P(7)->((2,3),SHOT13)
      ASSIGN P(7)->((2,4),SHOT14)
      ASSIGN P(7)->((2,5),SHOT15)
      ASSIGN P(7)->((2,6),SHOT16)
      ASSIGN P(7)->((2,7),SHOT17)
```

```
        ASSIGN P(7)->((2,8),SHOT18)
        ASSIGN P(7)->((2,9),SHOT19)
        ASSIGN P(7)->((2,10),SHOT20)
     AEND


PEND

LAYER 1

P(7) 'bearde2medsq.v30'
SPPRM 4.0,,,,1.0,1

STDCUR 1.5

        SHOT1:  MODULAT ((0,-75))
        SHOT2:  MODULAT ((0,-70))
        SHOT3:  MODULAT ((0,-65))
        SHOT4:  MODULAT ((0,-60))
        SHOT5:  MODULAT ((0,-55))
        SHOT6:  MODULAT ((0,-50))
        SHOT7:  MODULAT ((0,-45))
        SHOT8:  MODULAT ((0,-40))
        SHOT9:  MODULAT ((0,-35))
        SHOT10: MODULAT ((0,-30))
        SHOT11: MODULAT ((0,-25))
        SHOT12: MODULAT ((0,-20))
        SHOT13: MODULAT ((0,-15))
        SHOT14: MODULAT ((0,-10))
        SHOT15: MODULAT ((0, -5))
        SHOT16: MODULAT ((0,  0))
        SHOT17: MODULAT ((0,  5))
        SHOT18: MODULAT ((0, 10))
        SHOT19: MODULAT ((0, 15))
        SHOT20: MODULAT ((0, 25))

END
```

After the programming files are prepared, the sample may be prepared and loaded into the lithography system. The sample may be cut from the wafer (if a piece is to be patterned) or the whole wafer may be prepared. In this research, only pieces were used consisting of 4 x 9 devices to a piece. Electron beam resist is applied to the piece, here the piece is fixed to a carrier wafer. ZEP 520a e-beam resist was used, spun on at 5000 rpm for 60 s to produce a 350 nm thick layer. If the membranes are poorly formed or 'sag' under the resist (which is typically indicative of a mistake in the backside etch step), the thickness of the resist on the membranes will be thicker than 350 nm and the resulting nanopores will be larger than desired. No softbake step is required. The piece is then loaded onto the chosen cassette, taking care to avoid contamination. The cassette is then loaded into the EBL system.

2.   Exposure

Once the sample is loaded into the EBL system and the program files are set up, the alignment must be checked. With the thin metal layers used in this device, the alignment marks may offer poor contrast, in which case alignment must be done manually with the built in SEM capability. Once alignment is complete, the sample may be exposed with the electron beam, which typically only takes a few minutes. After the exposure, the cassette is unloaded from the EBL system and the sample removed. The patterned e-beam resist undergoes a post-bake (150C for 60s) before being developed in amyl acetate. The developed sample may be rinsed in isopropanol to remove excess developer.

3.   Etching

The nanopore is then etched in the membrane with an inductively coupled etch method. The sample may be diced into individual pieces in order to individually etch the pieces or the entire sample may be etched at once. Etching the entire sample at once runs the risk of destroying or underetching some of the samples. In either case, if the sample is not an entire wafer, the devices to be etched will be fixed to a carrier wafer and loaded into the Oxford Cryogenic ICP system. The recipe to use is dependent on the metal to be etched as Ti/Au electrodes may be etched with $CHF_3/O_2/Ar$ process gas, while platinum requires the addition of chlorine in a $CHF_3/O_2/Ar/Cl_2$ recipe (see appendix A for recipes and etch settings). Micron scale features may be examined under a microscope to ensure that the etch is complete. Once etching is complete, the devices may be diced to the required size and packaged for use in the flow cell.

<u>Transmission electron microscopy nanopore formation:</u>

The process of forming a nanopore with TEM is much more straightforward than the EBL method, but imposes certain requirements which make fabrication less efficient. In order to form nanopores with TEM, the membrane devices must be fabricated on thin silicon wafers (<200 μm thick), the membranes devices must be diced with a maximum dimension of 3 mm before loading into the TEM, and the TEM must be equipped with a field emission gun (FEG) electron source in order to achieve sufficient power. However, once these requirements are met, the individual samples may be loaded into the TEM and allowed to reach thermal equilibrium. Thermal equilibrium may take up to an hour to

achieve and may be assessed by imaging the sample. The sample will appear to move on its own in the sample holder as the materials contract in the cryogenic temperatures within the TEM column. Once sample motion ceases, the electron beam may be placed in 'nanoprobe' mode (to allow sub-nanometer beam focussing) and focussed on the center of the nanopore membrane. The screen current (the amount of current reaching the TEM detector) will initially decrease, then begin to increase until it reaches a constant value. Once the screen current reaches a constant value, the nanopore has been formed and may be imaged and removed from the sample holder.

Compared to EBL nanopore formation, the TEM method is much more straightforward. However the compromise is that the TEM method is slow due to the necessity of waiting for thermal equilibrium. For comparison purposes, 9 complete nanopore devices can be formed in 2.5 hours using the EBL method while only 5 devices were formed in 8 hrs using the TEM method. The advantage of the TEM method is that devices may be imaged directly after fabrication. In terms of device quality, no experimental difference has been observed between the fluidic or molecular detection capabilities of the EBL devices versus the TEM devices. In 100 mM NaF solution, both versions of the device have conductances of about 2nS, indicating that the size is similar regardless of the fabrication method. When choosing a nanopore formation technology, the goals of the experiment must be established. For mass fabrication, EBL is the economical choice. If the goal is to assess the structure of the nanopore with specific membrane and electrode materials, TEM offers immediate feedback.

Appendix C

HIDDEN MARKOV MODEL BASECALLER CODE

```matlab
function output = HMM_basecaller(filename, SeqName, training,
bp_resolution, v_sig_resolution, i_sig_resolution)

clear output


%% import data
% opens a saved .mat format data file
data = open(filename);

% extract the sampling rate from data
sampling_rate = data.sampling_rate;

% extract the time vector from data
time = data.time;

% extract the unfiltered ionic current trace from data
unfiltered_i = data.unfiltered_i;

% extract the unfiltered double layer potential trace from data
unfiltered_v = data.unfiltered_v;


% lookup the sequence of DNA sample (if known) in
DNA_characteristics_map returns the sequence encoded using
[EncodedSeq,EncodedSeq_comp] = DNA_characteristics_map(SeqName);

% Transforms the expected sequences into 4^n space
if bp_resolution > 1
    EncodedSeq = multibases(EncodedSeq, bp_resolution);
    EncodedSeq_comp = multibases(EncodedSeq_comp, bp_resolution);
end


%% filter V and I data
% filter cutoff frequencies were empirically determined
% Low_Pass_Filter and High_Pass_Filter are custom Butterworth filter
functions
filtered_v = Low_Pass_Filter(unfiltered_v,1500);
filtered_v = High_Pass_Filter(filtered_v,70);
```

```matlab
filtered_i = Low_Pass_Filter(unfiltered_i,1500);
filtered_i = High_Pass_Filter(filtered_i,100);

%% find edges in the V and I data
% Translocation events appear to be demarcated by 'jumps' in the
signal,
% we locate these demarcations with a Roberts cross algorithm

v_edge = edge(filtered_v,'roberts');
i_edge = edge(filtered_i,'roberts');



%% find time segments in the current trace

% initialize variables
i_index = [];
v_index = [];


% set the expected translocation time
time_min = (0.0112) + (0.0002)*length(EncodedSeq)*0.75;
time_max = (0.0112) + (0.0002)*length(EncodedSeq)*1.25;

% Iterate through the edges in the double layer potential trace
(v_edge)
% and ionic current trace (i_edge) to find pairs that occur within the
expected time range

[v_edge_spacing, v_index] = edge_pair_finder(v_edge, time, time_min,
time_max)

[i_edge_spacing, i_index] = edge_pair_finder(i_edge, time, time_min,
time_max)

% check for errors
if size(i_index) == [0,0]
    output = 'err';
    fprintf('size(i_index) == [0,0]')
    return
end

% check for errors
if size(v_index) == [0,0]
    output = 'err';
    fprintf('size(v_index) == [0,0]')
    return
end
```

```matlab
%% Check for similarities in the first column of i_index and v_index

[match_index_i, match_index_v] = index_compare(i_index, v_index,
sampling_rate)


% Only include indices of corresponding time segments
i_edge_spacing = i_edge_spacing(match_index_i);
v_edge_spacing = v_edge_spacing(match_index_v);
i_index = i_index(match_index_i,:);
v_index = v_index(match_index_v,:);


% check for errors
if length(v_index(:,1)) <= 0,0
    output = 'err';
    fprintf('length(v_index(:,1)) <= 0,0')
    return
end

% check for errors
if length(i_index(:,1)) <= 0,0
    output = 'err';
    fprintf('length(i_index(:,1)) <= 0,0')
    return
end


%% Separate out the corresponding time segments from the data traces

% initialize variables
len = max(v_index(:,2)-v_index(:,1));
matched_filtered_v = zeros(length(v_index(:,1)),len);
matched_filtered_i = zeros(length(i_index(:,1)),len);


% separate out data segments
for ii = 1:length(v_index(:,1))
    if (v_index(ii,1)-1+len) < length(filtered_v)

        matched_filtered_v(ii,:) =
filtered_v(v_index(ii,1):v_index(ii,1)-1+len);

    end
end

for ii = 1:length(i_index(:,1))
    if (i_index(ii,1)-1+len) < length(filtered_i)
```

220

```matlab
        matched_filtered_i(ii,:) =
filtered_i(i_index(ii,1):i_index(ii,1)-1+len);

    end
end


%% Find local extrema in the selected time segments

[pks_v, loc_v, pks_i, loc_i] = local_extrema(matched_filtered_v,
matched_filtered_i, EncodedSeq);

% check for errors
if length(pks_i(:,1)) <= 1 || length(pks_v(:,1)) <= 1
    output = 'err';
    fprintf('length(pks_i(:,1)) <= 1 || length(pks_v(:,1)) <= 1')
    return
end


%% Convert raw signal values into 4^m space ranks

v_rank = ones(length(pks_v(:,1)),length(EncodedSeq));
i_rank = ones(length(pks_i(:,1)),length(EncodedSeq));

for ii = 1:length(pks_i(:,1))
    if pks_i(ii,1) ~= 0 && pks_v(ii,1) ~= 0

        % class_multi is a function that transforms raw signal values
        % (electrical measurements) into 4^m space ranks
        [v_rank(ii,:)] = class_multi(pks_v(ii,:),v_sig_resolution,1);
        [i_rank(ii,:)] = class_multi(pks_i(ii,:),i_sig_resolution,2);

    end
end



%% encode ranks into a 4^(mi+mv) space dual output
seq = (4^i_sig_resolution)*(v_rank)-1)+i_rank);


%% decode with combined IC and GP signals

% initialize variables
PSTATES = zeros(length(TRANS_EST),length(seq(1,:)),length(seq(:,1)));

PSTATES_i =
zeros(length(TRANS_EST_i),length(seq(1,:)),length(seq(:,1)));
```

```matlab
PSTATES_v =
zeros(length(TRANS_EST_v),length(seq(1,:)),length(seq(:,1)));


% import trained HMMs
mult_trans = open(training);
TRANS_EST = mult_trans.TRANS_EST;
EMIS_EST = mult_trans.EMIS_EST;
TRANS_EST_v = mult_trans.TRANS_EST_v;
EMIS_EST_v = mult_trans.EMIS_EST_v;
TRANS_EST_i = mult_trans.TRANS_EST_i;
EMIS_EST_i = mult_trans.EMIS_EST_i;




% decode the sequence and calculate the posterior state probabilities
for ii = 1:length(seq(:,1))
    likelystates(ii,:) = hmmviterbi(seq(ii,:),TRANS_EST, EMIS_EST);

    PSTATES(1:length(TRANS_EST),1:length(seq(1,:)),ii)=
hmmdecode(seq(ii,:),TRANS_EST,EMIS_EST);

    % concatentate the decoded sequence into a data structure
    data_dual(ii).Sequence =
DNA_decode(likelystates(ii,:),bp_resolution);

    data_dual(ii).Header =
strcat('dual_',SeqName,'_training_iv_multi_bp',
num2str(bp_resolution),'_vsig', num2str(v_sig_resolution),'_isig',
num2str(i_sig_resolution),'_',num2str(ii));

end

% write the sequenced time segment data structure into a .fasta file
fastawrite(strcat('dual_',SeqName,'_training_iv_multi_bp1_vsig9_isig7.t
xt'), data_dual);

% determine the accuracy of the decoded segments in the dual channel
[states, hamming_dist, min_accuracy, max_accuracy, mean_accuracy,
std_accuracy, median_accuracy] = seq_state_comparator(likelystates,
seq, EncodedSeq )

% check for errors
if sum(sum(states==0)) > 0
    output = 'err';
    fprintf('sum(sum(states==0)) > 0')
    return
end

% calculate the Viterbi posterior state probability
```

```matlab
for ii = 1:length(seq(:,1))
    for jj = 1:length(seq(1,:))
        call_prob(ii,jj) = PSTATES(likelystates(ii,jj),jj,ii);
    end
end


% print statistics for the dual channel decoded segments
fprintf('\n dual min accuracy: %4.0f %%\n', min_accuracy);
fprintf('dual max accuracy: %4.0f %%\n', max_accuracy);
fprintf('dual mean accuracy: %4.0f %%\n', mean_accuracy);
fprintf('dual std accuracy: %4.0f %%\n', std_accuracy);
fprintf('dual median accuracy: %4.0f %%\n\n', median_accuracy);


% print the highest accuracy sequence obtained
[minA,ind] = min(hamming_dist);
basecall_con(likelystates(ind,:),call_prob(ind,:), bp_resolution);


%% decode with combined GP signals

% decode the sequence and calculate the posterior state probabilities
for ii = 1:length(v_rank(:,1))
    likelystates_v(ii,:) = hmmviterbi(v_rank(ii,:),TRANS_EST_v,
EMIS_EST_v);

    PSTATES_v(1:length(TRANS_EST_v),1:length(v_rank(1,:)),ii)=
hmmdecode(v_rank(ii,:),TRANS_EST_v,EMIS_EST_v);

    % concatentate the decoded sequence into a data structure
    data_v(ii).Sequence =
DNA_decode(likelystates_v(ii,:),bp_resolution);

    data_v(ii).Header =
strcat('DL_',SeqName,'_training_iv_multi_bp1_vsig9_isig7_',num2str(ii))
;

end

% write the sequenced time segment into a .fasta file
fastawrite(strcat('DL_',SeqName,'_training_iv_multi_bp1_vsig9_isig7.txt
'), data_v);


% determine the accuracy of the decoded segments in the double layer
potential channel
[states, hamming_dist, DL_min_accuracy, DL_max_accuracy,
DL_mean_accuracy, DL_std_accuracy, DL_median_accuracy] =
seq_state_comparator(likelystates_v, v_rank, EncodedSeq )
```

```matlab
% calculate the Viterbi posterior state probability
for ii = 1:length(v_rank(:,1))
    for jj = 1:length(v_rank(1,1:length(EncodedSeq)))
        call_prob_v(ii,jj) = PSTATES_v(likelystates_v(ii,jj),jj,ii);
    end
end


% print statistics for the double layer channel decoded segments
fprintf('\n DL min accuracy: %4.0f %%\n', DL_min_accuracy);
fprintf('DL max accuracy: %4.0f %%\n', DL_max_accuracy);
fprintf('DL mean accuracy: %4.0f %%\n', DL_mean_accuracy);
fprintf('DL std accuracy: %4.0f %%\n', DL_std_accuracy);
fprintf('DL median accuracy: %4.0f %%\n\n', DL_median_accuracy);

% print the highest accuracy sequence obtained
[minA,ind] = min(hamming_dist_v);
basecall_con(likelystates_v(ind,:),call_prob_v(ind,:), bp_resolution);


%% decode with combined IC signals

for ii = 1:length(i_rank(:,1))
    likelystates_i(ii,:) = hmmviterbi(i_rank(ii,:),TRANS_EST_i,
EMIS_EST_i);

    PSTATES_i(1:length(TRANS_EST_v),1:length(v_rank(1,:)),ii)=
hmmdecode(i_rank(ii,:),TRANS_EST_i,EMIS_EST_i);

    % concatentate the decoded sequence into a data structure
    data_i(ii).Sequence =
DNA_decode(likelystates_i(ii,:),bp_resolution);

    data_i(ii).Header =
strcat('IC_',SeqName,'_training_iv_multi_bp1_vsig9_isig7_',num2str(ii))
;
end

fastawrite(strcat('IC_',SeqName,'_training_iv_multi_bp1_vsig9_isig7.txt
'), data_i);

% determine the accuracy of the decoded segments in the ionic current
channel
[states_i, hamming_dist_i, IC_min_accuracy, IC_max_accuracy,
IC_mean_accuracy, IC_std_accuracy, IC_median_accuracy] =
seq_state_comparator(likelystates_i, i_rank, EncodedSeq )

% calculate the Viterbi posterior state probability
for ii = 1:length(i_rank(:,1))
    for jj = 1:length(i_rank(1,1:length(EncodedSeq)))
```

```matlab
        call_prob_i(ii,jj) = PSTATES_i(likelystates_i(ii,jj),jj,ii);
    end
end


% print statistics for the ionic current channel decoded segments
fprintf('\n IC min accuracy: %4.0f %%\n', IC_min_accuracy);
fprintf('IC max accuracy: %4.0f %%\n', IC_max_accuracy);
fprintf('IC mean accuracy: %4.0f %%\n', IC_mean_accuracy);
fprintf('IC std accuracy: %4.0f %%\n', IC_std_accuracy);
fprintf('IC median accuracy: %4.0f %%\n\n', IC_median_accuracy);

% print the highest accuracy sequence obtained
[minA,ind] = min(hamming_dist_i);
basecall_con(likelystates_i(ind,:),call_prob_i(ind,:), bp_resolution);




output = struct('dual_max_accuracy', max_accuracy, 'DL_max_accuracy',
DL_max_accuracy, 'IC_max_accuracy', IC_max_accuracy, 'i_rank', i_rank,
'v_rank', v_rank, 'states_for', states_for, 'SeqName', SeqName,
'likelystates', likelystates, 'likelystates_v', likelystates_v,
'likelystates_i', likelystates_i, 'pks_v', pks_v, 'pks_i', pks_i,
'call_prob', call_prob, 'call_prob_v', call_prob_v, 'call_prob_i',
call_prob_i);
```

REFERENCES

(1)   Zhang, G. Zhang Nanopore Patent US20100289505A1.pdf, 2010, 10.

(2)   Bearden, S.; Zhang, G. A Solid-State Nanopore as Biosensor. In *Computational Bioengineering*; Zhang, G., Ed.; CRC Press, 2015; pp. 355–376.

(3)   Bearden, S.; Zhang, G. The Effects of the Electrical Double Layer on Giant Ionic Currents through Single-Walled Carbon Nanotubes. **2013**, *24*.

(4)   Bearden, S.; Simpanen, E.; Zhang, G. Active Current Gating in Electrically Biased Conical Nanopores. *Nanotechnology* **2015**, *26*, 185502.

(5)   Hückel, E.; Debye, P. The Theory of Electrolytes. I. Lowering of Freezing Point and Related Phenomena. *Phys. Zeitschrift* **1923**, *24*, 185–206.

(6)   Zhang, G. Chapter 6: Nanotechnology-Based Biosensors in Drug Delivery. In *Nanotechnology in Drug Delivery*; de Villiers, M. M.; Aramwit, P.; Kwon, G. S., Eds.; Springer: New York, 2009; pp. 163–189.

(7)   Gangadharan, R.; Anandan, V.; Zhang, A.; Drwiega, J. C.; Zhang, G. Enhancing the Performance of a Fluidic Glucose Biosensor with 3D Electrodes. *Sensors Actuators B Chem.* **2011**, *160*, 991–998.

(8)   Gangadharan, R.; Anandan, V.; Zhang, G. Optimizing the Functionalization Process for Nanopillar Enhanced Electrodes with GOx/PPY for Glucose Detection. *Nanotechnology* **2008**, *19*, 395501.

(9)   Anandan, V.; Gangadharan, R.; Zhang, G. Role of SAM Chain Length in Enhancing the Sensitivity of Nanopillar Modified Electrodes for Glucose Detection. *Sensors (Basel).* **2009**, *9*, 1295–1305.

(10)   Pang, P.; He, J.; Park, J. H.; Krstić, P. S.; Lindsay, S. Origin of Giant Ionic Currents in Carbon Nanotube Channels. *ACS Nano* **2011**, *5*, 7277–7283.

(11)   Kalman, E. B.; Sudre, O.; Vlassiouk, I.; Siwy, Z. S. Control of Ionic Transport through Gated Single Conical Nanopores. *Anal. Bioanal. Chem.* **2009**, *394*, 413–419.

(12)   Vlassiouk, I.; Smirnov, S.; Siwy, Z. Ionic Selectivity of Single Nanochannels. *Nano Lett.* **2008**, *8*, 1978–1985.

(13)   Siwy, Z.; Fuliński, a. Fabrication of a Synthetic Nanopore Ion Pump. *Phys. Rev. Lett.* **2002**, *89*, 4–7.

(14)   Siwy, Z.; Heins, E.; Harrell, C. C.; Kohli, P.; Martin, C. R. Conical-Nanotube Ion-Current Rectifiers: The Role of Surface Charge. *J. Am. Chem. Soc.* **2004**, *126*, 10850–10851.

(15)   Ali, M.; Mafe, S.; Ramirez, P.; Neumann, R.; Ensinger, W. Logic Gates Using Nanofluidic Diodes Based on Conical Nanopores Functionalized with Polyprotic Acid Chains. *Langmuir* **2009**, *25*, 11993–11997.

(16)   De Zoysa, R. S. S.; Krishantha, D. M. M.; Zhao, Q.; Gupta, J.; Guan, X. Translocation of Single-Stranded DNA through the A-Hemolysin Protein Nanopore in Acidic Solutions. *Electrophoresis* **2011**, *32*, 3034–3041.

(17)   Chang, H.; Kosari, F.; Andreadakis, G.; Alam, M. a.; Vasmatzis, G.; Bashir, R. DNA-Mediated Fluctuations in Ionic Current through Silicon Oxide Nanopore Channels. *Nano Letters*, 2004, *4*, 1551–1556.

(18)   Gracheva, M. E.; Xiong, A.; Aksimentiev, A.; Schulten, K.; Timp, G.; Leburton, J.-P. Simulation of the Electric Response of DNA Translocation through a Semiconductor Nanopore–capacitor. *Nanotechnology* **2006**, *17*, 622–633.

(19)   Ivanov, A. P.; Instuli, E.; McGilvery, C. M.; Baldwin, G.; McComb, D. W.; Albrecht, T.; Edel, J. B. DNA Tunneling Detector Embedded in a Nanopore. *Nano Lett.* **2011**, *11*, 279–285.

(20)   Timp, W.; Mirsaidov, U. M.; Wang, D.; Comer, J.; Aksimentiev, A.; Timp, G. Nanopore Sequencing: Electrical Measurements of the Code of Life. *IEEE Trans. Nanotechnol.* **2010**, *9*, 281–294.

(21)   Min, S. K.; Kim, W. Y.; Cho, Y.; Kim, K. S. Fast DNA Sequencing with a Graphene-Based Nanochannel Device. *Nat. Nanotechnol.* **2011**, *6*, 162–165.

(22)   Deamer, D. W.; Branton, D. Characterization of Nucleic Acids by Nanopore Analysis. *Acc. Chem. Res.* **2002**, *35*, 817–825.

(23)   Schneider, G. F.; Kowalczyk, S. W.; Calado, V. E.; Pandraud, G.; Zandbergen, H. W.; Vandersypen, L. M. K.; Dekker, C. DNA Translocation through Graphene Nanopores. *Nano Lett.* **2010**, *10*, 3163–3167.

(24)   Branton, D.; Deamer, D. W.; Marziali, A.; Bayley, H.; Benner, S. a; Butler, T.; Ventra, M. Di; Garaj, S.; Hibbs, A.; Jovanovich, S. B.; et al. The Potential and Challenges of Nanopore Sequencing. *Genome Res.* **2008**, *26*, 1146–1153.

(25)   Nelson, T.; Zhang, B.; Prezhdo, O. V. Detection of Nucleic Acids with Graphene Nanopores: Ab Initio Characterization of a Novel Sequencing Device. *Nano Lett.* **2010**, *10*, 3237–3242.

(26)   Ohshiro, T.; Umezawa, Y. Complementary Base-Pair-Facilitated Electron Tunneling for Electrically Pinpointing Complementary Nucleobases. *Proc. Natl. Acad. Sci. U. S. A.* **2006**, *103*, 10–14.

(27)   Saha, K. K.; Drndić, M.; Nikolić, B. K. DNA Base-Specific Modulation of Microampere Transverse Edge Currents through a Metallic Graphene Nanoribbon with a Nanopore. *Nano Lett.* **2011**, *12*, 50–55.

(28)   Lee, C. Y.; Choi, W.; Han, J.-H.; Strano, M. S. Coherence Resonance in a Single-Walled Carbon Nanotube Ion Channel. *Science* **2010**, *329*, 1320–1324.

(29)   Smeets, R. M. M.; Keyser, U. F.; Krapf, D.; Wu, M.-Y.; Dekker, N. H.; Dekker, C. Salt Dependence of Ion Transport and DNA Translocation through Solid-State Nanopores. *Nano Lett.* **2006**, *6*, 89–95.

(30)   Yan, Y.; Wang, L.; Xue, J.; Chang, H.-C. Ion Current Rectification Inversion in Conic Nanopores: Nonequilibrium Ion Transport Biased by Ion Selectivity and Spatial Asymmetry. *J. Chem. Phys.* **2013**, *138*, 044706.

(31)   Majumder, M.; Chopra, N.; Andrews, R.; Hinds, B. J. Enhanced Flow in Carbon Nanotubes. *Nature* **2005**, *438*, 43–44.

(32)   Bearden, S.; Zhang, G. The Effects of the Electrical Double Layer on Giant Ionic Currents through Single-Walled Carbon Nanotubes. *Nanotechnology* **2013**, *24*, 125204.

(33)   Skou, J. C. Enzymatic Basis for Active Transport of Na+ and K+ Across Cell Membrane. *Physiol. Rev.* **1965**, *45*, 596–617.

(34)   Scha, A. R. Review Aquaporin Function , Structure , and Expression : Are There More Surprises to Surface in Water Relations ? *Planta* **1998**, *204*, 131–139.

(35)   Pang, P.; He, J.; Park, J. H.; Krstić, P. S.; Lindsay, S.; Page, S. Supporting Information for " Origin of Giant Ionic Currents in Carbon Nanotube Channels ." *ACS Nano* **2011**, *5*, 1–40.

(36)   Wu, J.; Gerstandt, K.; Majumder, M.; Zhan, X.; Hinds, B. J. Highly Efficient Electroosmotic Flow through Functionalized Carbon Nanotube Membranes. *Nanoscale* **2011**, *3*, 3321–3328.

(37) Holt, J. K.; Park, H. G.; Wang, Y.; Stadermann, M.; Artyukhin, A. B.; Grigoropoulos, C. P.; Noy, A.; Bakajin, O. Fast Mass Transport through Sub-2-Nanometer Carbon Nanotubes. *Science* **2006**, *312*, 1034–1037.

(38) Apel, P. Y.; Korchev, Y. .; Siwy, Z.; Spohr, R.; Yoshida, M. Diode-like Single-Ion Track Membrane Prepared by Electro-Stopping. *Nucl. Instruments Methods Phys. Res. Sect. B Beam Interact. with Mater. Atoms* **2001**, *184*, 337–346.

(39) Kowalczyk, S. W.; Grosberg, A. Y.; Rabin, Y.; Dekker, C. Modeling the Conductance and DNA Blockade of Solid-State Nanopores. *Nanotechnology* **2011**, *22*, 315101.

(40) Firnkes, M.; Pedone, D.; Knezevic, J.; Döblinger, M.; Rant, U. Electrically Facilitated Translocations of Proteins through Silicon Nitride Nanopores: Conjoint and Competitive Action of Diffusion, Electrophoresis, and Electroosmosis. *Nano Lett.* **2010**, *10*, 2162–2167.

(41) Lu, N.; Wang, J.; Floresca, H. C.; Kim, M. J. In Situ Studies on the Shrinkage and Expansion of Graphene Nanopores under Electron Beam Irradiation at Temperatures in the Range of 400–1200°C. *Carbon N. Y.* **2012**, *50*, 2961–2965.

(42) Merchant, C. a; Healy, K.; Wanunu, M.; Ray, V.; Peterman, N.; Bartel, J.; Fischbein, M. D.; Venta, K.; Luo, Z.; Johnson, a T. C.; et al. DNA Translocation through Graphene Nanopores. *Nano Lett.* **2010**, *10*, 2915–2921.

(43) Liu, H.; He, J.; Tang, J.; Liu, H.; Pang, P.; Cao, D.; Krstic, P.; Joseph, S.; Lindsay, S.; Nuckolls, C. Translocation of Single-Stranded DNA through Single-Walled Carbon Nanotubes. *Science* **2010**, *327*, 64–67.

(44) Venkatesan, B. M.; Estrada, D.; Banerjee, S.; Jin, X.; Dorgan, V. E.; Bae, M.-H.; Aluru, N. R.; Pop, E.; Bashir, R. Stacked Graphene-Al2O3 Nanopore Sensors for Sensitive Detection of DNA and DNA-Protein Complexes. *ACS Nano* **2012**, *6*, 441–450.

(45) Novoselov, K. S.; Geim, a K.; Morozov, S. V; Jiang, D.; Katsnelson, M. I.; Grigorieva, I. V; Dubonos, S. V; Firsov, a a. Two-Dimensional Gas of Massless Dirac Fermions in Graphene. *Nature* **2005**, *438*, 197–200.

(46) Novoselov, K. S.; Abbott, E. A.; Romance, F. A. GRAPHENE : MATERIALS IN THE FLATLAND. *Rev. Mod. Phys.* **2010**, *83*, 106–131.

(47) Novoselov, K. S.; Jiang, D.; Schedin, F.; Booth, T. J.; Khotkevich, V. V; Morozov, S. V; Geim, a K. Two-Dimensional Atomic Crystals. *Proc. Natl. Acad. Sci. U. S. A.* **2005**, *102*, 10451–10453.

(48)   Novoselov, K. S.; Geim, a K.; Morozov, S. V; Jiang, D.; Zhang, Y.; Dubonos, S.
         V; Grigorieva, I. V; Firsov, a a. Electric Field Effect in Atomically Thin Carbon
         Films. *Science* **2004**, *306*, 666–669.

(49)   Nam, S.-W.; Rooks, M. J.; Kim, K.-B.; Rossnagel, S. M. Ionic Field Effect
         Transistors with Sub-10 Nm Multiple Nanopores. *Nano Lett.* **2009**, *9*, 2044–2048.

(50)   Allen, M. J.; Tung, V. C.; Kaner, R. B. Honeycomb Carbon: A Review of
         Graphene. *Chem. Rev.* **2010**, *110*, 132–145.

(51)   Krapf, D.; Wu, M.-Y.; Smeets, R. M. M.; Zandbergen, H. W.; Dekker, C.; Lemay,
         S. G. Fabrication and Characterization of Nanopore-Based Electrodes with Radii
         down to 2 Nm. *Nano Lett.* **2006**, *6*, 105–109.

(52)   Wanunu, M.; Morrison, W.; Rabin, Y.; Grosberg, A. Y.; Meller, A. Electrostatic
         Focusing of Unlabelled DNA into Nanoscale Pores Using a Salt Gradient. *Nat.
         Nanotechnol.* **2010**, *5*, 160–165.

(53)   Heng, J. B.; Aksimentiev, A.; Ho, C.; Marks, P.; Grinkova, Y. V; Sligar, S.;
         Schulten, K.; Timp, G. Stretching DNA Using the Electric Field in a Synthetic
         Nanopore. *Nano Lett.* **2005**, *5*, 1883–1888.

(54)   Melngailis, J. Focused Ion Beam Technology and Applications. *J. Vac. Sci.
         Technol. B Microelectron. Nanom. Struct.* **1987**, *5*, 469.

(55)   Matsunami, N.; Yamamura, Y.; Ltikawa, Y.; Itoh, N.; Kazumata, Y.; Miyagawa,
         S.; Morita, K.; Shimizu, R.; Tawara, H. Energy Dependence of Sputtering Yields
         of Monatomic Solids. *At. Data Nucl. Data Tables* **1984**, *31*, 1–80.

(56)   Bacri, L.; Oukhaled, a G.; Schiedt, B.; Patriarche, G.; Bourhis, E.; Gierak, J.; Pelta,
         J.; Auvray, L. Dynamics of Colloids in Single Solid-State Nanopores. *J. Phys.
         Chem. B* **2011**, *115*, 2890–2898.

(57)   Powell, M. R.; Cleary, L.; Davenport, M.; Shea, K. J.; Siwy, Z. S. Electric-Field-
         Induced Wetting and Dewetting in Single Hydrophobic Nanopores. *Nature
         nanotechnology*, 2011, *6*, 798–802.

(58)   Siwy, Z.; Ausloos, M.; Ivanova, K. Correlation Studies of Open and Closed State
         Fluctuations in an Ion Channel: Analysis of Ion Current through a Large-
         Conductance Locust Potassium Channel. *Phys. Rev. E* **2002**, *65*, 1–6.

(59)   Siwy, Z. S. Ion-Current Rectification in Nanopores and Nanotubes with Broken
         Symmetry. *Adv. Funct. Mater.* **2006**, *16*, 735–746.

(60)   Cervera, J.; Schiedt, B.; Ramírez, P. A Poisson/Nernst-Planck Model for Ionic Transport through Synthetic Conical Nanopores. *Europhys. Lett.* **2005**, *71*, 35–41.

(61)   Nishizawa, M.; Menon, V. P.; Martin, C. R. Metal Nanotubule Membranes with Electrochemically Switchable Ion-Transport Selectivity. *Science* **1995**, *268*, 700–702.

(62)   Yang, X.; Zhang, G. The Effect of an Electrical Double Layer on the Voltammetric Performance of Nanoscale Interdigitated Electrodes: A Simulation Study. *Nanotechnology* **2008**, *19*, 465504.

(63)   Kovarik, M. L.; Zhou, K.; Jacobson, S. C. Effect of Conical Nanopore Diameter on Ion Current Rectification. *J. Phys. Chem. B* **2009**, *113*, 15960–15966.

(64)   Pham, P.; Howorth, M.; Planat-chrétien, A.; Tardu, S. Numerical Simulation of the Electrical Double Layer Based on the Poisson-Boltzmann Models for AC Electroosmosis Flows. In *Excerpt from the Proceedings of the COMSOL Users Conference 2007 Grenoble*; 2007.

(65)   Keh, H. J.; Wu, Y. Y. Electroosmotic Velocity and Electric Conductivity in a Fibrous Porous Medium in the Transverse Direction. *J. Phys. Chem. B* **2011**, *115*, 9168–9178.

(66)   Smith, C. P. Theory of the Voltammetric Response of Electrodes of Submicron Dimensions . Violation of Electroneutrality in the Presence of Excess Supporting Electrolyte. *Anal. Chem.* **1991**, *65*, 3343–3353.

(67)   Berg, P.; Findlay, J. Analytical Solution of the Poisson-Nernst-Planck-Stokes Equations in a Cylindrical Channel. *Proc. R. Soc. A Math. Phys. Eng. Sci.* **2011**, *467*, 3157–3169.

(68)   Movahed, S.; Li, D. Electrokinetic Transport through Nanochannels. *Electrophoresis* **2011**, *32*, 1259–1267.

(69)   Karnik, R.; Duan, C.; Castelino, K.; Daiguji, H.; Majumdar, A. Rectification of Ionic Current in a Nanofluidic Diode. *Nano Lett.* **2007**, *7*, 547–551.

(70)   Grahame, D. C. The Electrical Double Layer and the Theory of Electrocapillarity. *Chem. Rev.* **1947**, *41*, 441–501.

(71)   Macdonald, J. R. Theory of the Differential Capacitance of the Double Layer in Unadsorbed Electrolytes. *J. Chem. Phys.* **1954**, *22*, 1857–1866.

(72) Yang, X.; Zhang, G. Simulating the Structure and Effect of the Electrical Double Layer at Nanometre Electrodes. *Nanotechnology* **2007**, *18*, 335201.

(73) Ulam, S. M. Statistical Methods in Neutron Diffusion: With J. von Neumann and R. D. Richtmyer (LAMS-551, April 9, 1947). In *Analogies Between Analogies: The Mathematical Reports of S.M.Ulam and His Los Alamos Collaborators*; Bednarek, A. R.; Ulam, F., Eds.; University of California Press: Oxford, England, 1990; pp. 18–37.

(74) Comer, J.; Dimitrov, V.; Zhao, Q.; Timp, G.; Aksimentiev, A. Microscopic Mechanics of Hairpin DNA Translocation through Synthetic Nanopores. *Biophys. J.* **2009**, *96*, 593–608.

(75) Gad-El-Hak, M. Differences between Liquid and Gas Transport at the Microscale. *Bull. Polish Acad. Sci.* **2005**, *53*, 301–316.

(76) Hammack, A.; Chen, Y.-L.; Pearce, J. Role of Dissolved Salts in Thermophoresis of DNA: Lattice-Boltzmann-Based Simulations. *Phys. Rev. E* **2011**, *83*, 1–7.

(77) Chen, J. Large On-Off Ratios and Negative Differential Resistance in a Molecular Electronic Device. *Science (80-.).* **1999**, *286*, 1550–1552.

(78) Electron Work Function of the Elements. In *CRC Handbook of Chemistry and Physics, 93rd Edition (Internet Version 2013)*; Haynes, W. M. et al, Ed.; CRC Press/Taylor and Francis: Boca Raton, FL., 2012; p. 124.

(79) *Fundamentals of Adhesion*; Lee, L. H., Ed.; 1st ed.; Springer-Verlag New York, LLC: New York, NY, 1991.

(80) Ibach, H.; Rowe, J. E. Electron Orbital Energies of Oxygen Adsorbed on Silicon Surfaces and of Silicon Dioxide. *Phys. Rev. B* **1974**, *10*, 710–718.

(81) Meller, A.; Branton, D. Single Molecule Measurements of DNA Transport through a Nanopore. *Electrophoresis* **2002**, *23*, 2583–2591.

(82) Chen, P.; Gu, J.; Brandin, E.; Kim, Y.-R.; Wang, Q.; Branton, D. Probing Single DNA Molecule Transport Using Fabricated Nanopores. *Nano Lett.* **2004**, *4*, 2293–2298.

(83) Scruggs, N. R.; Robertson, J. W. F.; Kasianowicz, J. J.; Migler, K. B. Rectification of the Ionic Current through Carbon Nanotubes by Electrostatic Assembly of Polyelectrolytes. *Nano Lett.* **2009**, *9*, 3853–3859.

(84) Chen, P.; Mitsui, T.; Farmer, D. B.; Golovchenko, J.; Gordon, R. G.; Branton, D. Atomic Layer Deposition to Fine-Tune the Surface Properties and Diameters of Fabricated Nanopores. *Nano Lett.* **2004**, *4*, 1333–1337.

(85) Chu, L. L.; Takahata, K.; Selvaganapathy, P.; Shohet, J. L.; Gianchandani, Y. B. A MICROMACHINED KELVIN PROBE FOR SURFACE POTENTIAL MEASUREMENTS IN MICROFLUIDIC CHANNELS AND SOLID-STATE APPLICATIONS. *12th Int. Conf. Solid-State Sensors, Actuators Microsystems* **2003**.

(86) Duan, C.; Majumdar, A. Anomalous Ion Transport in 2-Nm Hydrophilic Nanochannels. *Nat. Nanotechnol.* **2010**, *5*, 848–852.

(87) Zhang, G.; Gilbert, J. L. A New Method for Real-Time and In-Situ Characterization of the Mechanical and Material Properties of Biological Tissue Constructs. In *Tissue Engineered Medical Products*; Schutte, E.; Kaplan, D.; Picciolo, G., Eds.; ASTM International: West Conshohocken, PA, 2003; pp. 120–133.

(88) Postma, H. W. C. Rapid Sequencing of Individual DNA Molecules in Graphene Nanogaps. *Nano Lett.* **2010**, *10*, 420–425.

(89) Maitra, R. D.; Kim, J.; Dunbar, W. B. Recent Advances in Nanopore Sequencing. *Electrophoresis* **2012**, n/a – n/a.

(90) Eisenstein, M. Oxford Nanopore Announcement Sets Sequencing Sector Abuzz. *Nat. Biotechnol.* **2012**, *30*, 295–296.

(91) Liu, Y.; Dong, X.; Chen, P. Biological and Chemical Sensors Based on Graphene Materials. *Chem. Soc. Rev.* **2012**, *41*, 2283–2307.

(92) Bard, A. J.; Faulkner, L. R. *Electrochemical Methods: Fundamentals and Applications*; 2nd ed.; Wiley, 2001.

(93) Zwolak, M.; Di Ventra, M. Electronic Signature of DNA Nucleotides via Transverse Transport. *Nano Lett.* **2005**, *5*, 421–424.

(94) Church, G.; Deamer, D. W.; Branton, D.; Baldarelli, R.; Kasianowicz, J. J. CHARACTERIZATION OF INDIVIDUAL POLYMER MOLECULES BASED ON MONOMER-INTERFACE INTERACTIONS. 5,795,782, 1998.

(95) Kasianowicz, J. J.; Brandin, E.; Branton, D.; Deamer, D. W. Characterization of Individual Polynucleotide Molecules Using a Membrane Channel. *Proc. Natl. Acad. Sci. U. S. A.* **1996**, *93*, 13770–13773.

(96)   Shannon, C. E. A Mathematical Theory of Communication. *Bell Syst. Tech. J.* **1948**, *27*, 379–423.

(97)   Timp, W.; Comer, J.; Aksimentiev, A. DNA Base-Calling from a Nanopore Using a Viterbi Algorithm. *Biophys. J.* **2012**, *102*, L37–L39.

(98)   Fan, R.; Karnik, R.; Yue, M.; Li, D.; Majumdar, A.; Yang, P. DNA Translocation in Inorganic Nanotubes. *Nano Lett.* **2005**, *5*, 1633–1637.

(99)   Clausen-Schaumann, H.; Rief, M.; Tolksdorf, C.; Gaub, H. E. Mechanical Stability of Single DNA Molecules. *Biophys. J.* **2000**, *78*, 1997–2007.

(100) Smith, S. B.; Cui, Y.; Bustamante, C. Overstretching B-DNA: The Elastic Response of Individual Double-Stranded and Single-Stranded DNA Molecules. *Science* **1996**, *271*, 795–799.